

Electrical and Electrochemical Properties of Nitrogen-Containing Tetrahedral Amorphous
Carbon (ta-C) Thin Films

By

Xingyi Yang

A DISSERTATION

Submitted to
Michigan State University
in partial fulfillment of the requirements
for the degree of

DOCTOR OF PHILOSOPHY

Chemistry

2013

ABSTRACT

Electrical and Electrochemical Properties of Nitrogen-Containing Tetrahedral Amorphous Carbon(ta-C) Thin-Films

By

Xingyi Yang

Tetrahedral amorphous carbon (ta-C) is a diamond-like carbon (DLC) material comprised of a mixture of sp^2 (~40%) and sp^3 -bonded (~60%) carbon domains. The physicochemical structure and electrochemical properties depend strongly on the sp^2/sp^3 bonding ratio as well as the incorporation of impurities, such as hydrogen or nitrogen. The ability to grow ta-C films at lower temperatures (25-100°C) on a wider variety of substrates is a potential advantage of these materials as compared with diamond films.

In this project, the basic structural and electrochemical properties of nitrogen-incorporated ta-C thin films will be discussed. The major goal of this work was to determine if the ta-C:N films exhibit electrochemical properties more closely aligned with those of boron-doped diamond (sp^3 carbon) or glassy carbon (amorphous sp^2 carbon). Much like diamond, ta-C:N thin-film electrodes are characterized by a low background voltammetric current, a wide working potential window, relatively rapid electron-transfer kinetics for aqueous redox systems, such as $Fe(CN)_6^{-3/-4}$ and $Ru(NH_3)_6^{+3/+2}$, and weak adsorption of polar molecules from solution. For example, negligible adsorption of methylene blue was found on the ta-C:N films in contrast to glassy carbon; a surface on which this molecule strongly adsorbs. The film microstructure was studied with x-ray photoelectron microscopy (XPS), visible Raman spectroscopy and electron-

energy loss spectroscopy (EELS); all of which revealed the sp^2 -bonded carbon content increased with increasing nitrogen.

The electrical properties of ta-C:N films were studied by four-point probe resistance measurement and conductive-probe AFM (CP-AFM). The incorporation of nitrogen into ta-C films increased the electrical conductivity primarily by increasing the sp^2 -bonded carbon content. CP-AFM showed the distribution of the conductive sp^2 -carbon on the film surface was not uniform. These films have potential to be used in field emission area. The heterogeneous electrochemical properties were studied with scanning electron microscopy (SECM). It was found that more electrically conducting sites were isolated by less conducting or even insulating sites. Consistent with the heterogeneous electrical properties, heterogeneous electrochemical activity was observed for different aqueous redox analytes.

Flow injection analysis with electrochemical detection (EC-FIA) of dopamine and norepinephrine were carried out using the N-ta:C films. Detection figures of merit for these biomolecules were determined. These biomolecules can be detected stably and reproducibly in PBS buffer at constant potential by N-ta:C film. The N-ta:C films provide good limits of detection for these biomolecules.

N-ta:C films show great promise in the electroanalytical field. Compared with the diamond, the growth condition is much milder. These N-ta:C films are commercially available and could be produced in large scale. All of these virtues make N-ta:C films excellent choices for electroanalytical measurements.

ACKNOWLEDGEMENTS

It is very emotional to come to write the acknowledgements to those who helped me in the tough process of my PhD.

First I express my sincere appreciation to my advisor, Professor Greg M. Swain, for his academic guidance in this research and his encouragements as a mentor. Thank you for his challenge to be an excellent student. I would also thank you to Dr Merlin Bruening, my second reader, for his discussions with me during this research, Dr Dana Spence and Dr Lawrence Drzal for all of their comments and kindness of being my committee members.

I would like to thank the members of the Swain group. Matt Swope and Liang Guo helped me a lot in the first two years. Matt Phaner, Yingrui Dai, Doo Young Kim, Hong Zhao, Ayten Ay, Liangliang Li, Yan Zhu, Catherine Munson, LeighAnn Jordan and Marion France are all great people and I enjoyed working with you guys.

I especially felt lucky to have Gabriel DeVivo as my technician in this research. He was a hard-working and very intelligent guy. He made a significant contribution to this project. I would also especially thank to Dr Xudong Fan for his help about using the TEM and utilization of the EELS in this research.

I am very proud of having wonderful friends in my life. Kelly Young, Cassie Phaner, Jennie Miller, Nicholas White, Chen Qiu, Yuling Xie, Chen Zhang, Bai Nie, Bite Zhou and Zhe Chen supported me a lot to survive in this tough process.

Last and most importantly, I have a very good family, my Mom and Dad, brother Xingfu, sister Xingyu and Xingrong to support me forever. They gave me a lot of support, not only economic but also mental. They encouraged me to come to USA for my graduate study. Whenever I felt depressed with my research and wanted to give up, they taught me the importance of persistence in my life. Without their support, I cannot finish this big achievement in my life. My brother Xingfu is my mentor in my life. He always reminded me the motivation of your life should be your dreams no matter what happened. I love my family.

Keep on fighting for your dream and it will become true!

TABLE OF CONTENTS

LIST OF TABLES	x
LIST OF FIGURES	xi
Chapter 1. Introduction	1
1.1 Overview of ta:C films	1
1.1.1 Growth of ta:C Films	7
1.1.2 Characterization of ta:C films	9
1.2 Review of the Electrical and Electrochemical Properties	12
1.3 The microscopic structure of ta:C film	16
1.4 The influence of nitrogen to these properties	17
1.5 Hypothesis and Research	18
Chapter 2. Experimental Approach	20
2.1 Growth of ta:C films by Physical Vapor Deposition (PVD)	20
2.2 Physical and Chemical Characterization	20
2.2.1 Four-Point Probe Resistance Measurements	20
2.2.2 XPS	22
2.2.3 Raman Spectra	22
2.2.4 TEM	22
2.3 Electrochemical Characterization	23
2.3.1 Cyclic Voltammetry	23
2.3.2 Flow Injection Analysis (FIA)	24
2.4 Characterization by Scanning Probe Methods	26
2.4.1 Conductive-Probe Atomic Force Microscopy (CP-AFM)	26
2.4.2 Scanning Electrochemical Microscopy (SECM)	30
2.5 Reagents for electrochemical measurements	31
Chapter 3. Electroanalytical Performance of Nitrogen-Containing Tetrahedral amorphous Carbon Thin-Film Electrodes	32
3.1 Introduction	32
3.2 Microstructure Characterization	33
3.2.1 X-ray Photoelectron Spectroscopy (XPS)	33
3.2.2 Atomic Force Microscopy (AFM)	35
3.2.3 Electron Energy Loss Spectra (EELS)	36
3.2.4 Visible Raman Spectroscopy	39
3.3 Electrochemical Performance	42
3.3.1 Background Current and Capacitance-Potential Profiles	42
3.3.2 Electrochemical Activities in Outer-sphere and Inner-sphere Redox Couples	44
3.3.3 Electrochemical Behavior of Methylene Blue	48
3.4 Microstructural Stability	51
3.4.1 Effect of Anodic Polarization	51
3.4.2 Effect of Chemical Oxidation	54

3.5 Discussion and Conclusions	55
Chapter 4. Factors Affecting the Microscopic Electrical and Electrochemical Properties of Nitrogen-Containing Tetrahedral Amorphous Carbon Thin-Film Electrodes.....	61
4.1 Heterogeneous Electrical Conductivity of N-ta:C films	61
4.1.1 Introduction.....	61
4.1.2 CP-AFM Images and Topography of the ta:C and N-ta:C Films.....	62
4.1.3 Effect of Bias Voltage Polarity and Magnitude	64
4.1.5 Conclusions	69
4.2 Heterogeneous Electrochemical Properties of N-ta:C Films	71
4.2.1 Introduction	71
4.2.2 Tip Conditioning	72
4.2.3 Tip Approach Curves	74
4.2.4 SECM Images for N-ta:C Films in $\text{Ru}(\text{NH}_3)_6^{3+/2+}/1\text{M KCl}$	79
4.2.5 SECM Images for N-ta:C Films in $\text{Fe}(\text{CN})_6^{3-/4-}/1\text{M KCl}$	80
4.2.4 Conclusions	82
Chapter 5. Application of Nitrogen-Containing Tetrahedral Amorphous Carbon (ta-C) Thin-film Electrodes in Flow Injection Analysis	83
5.1 Introduction	83
5.2 Cyclic Voltammetry of Dopamine and Norepinephrine	85
5.3 FIA-EC studies of Norepinephrine	90
5.3.1 Hydrodynamic Voltammetric <i>i-E</i> Curves	90
5.3.2 Detection figures of merit for DA and NE	92
5.3.3 Conclusions	98
Chapter 6. Conclusions and Future Work.....	100
REFERENCES	103

LIST OF TABLES

Table 3.2 Raman spectral parameters for ta:C and N-ta:C films obtained from fitting the spectra with two peaks using Gaussian-Lorentzian functions: D-band at 1358 cm^{-1} and G-band at 1580 cm^{-1} . The N-ta:C films were deposited with 10, 30 and 50 sccm N_2 . (n=4).....	40
Table 3.3 Summary of iR-corrected cyclic voltammetric data for $\text{Ru}(\text{NH}_3)_6^{+3/+2}$ and..... $\text{Fe}(\text{CN})_6^{-3/-4}$ at ta:C and N-ta:C thin films deposited with 10, 30 and 50 sccm N_2 . Scan rate = 0.1 V/s. Geometric area = 0.2 cm^2 . (n=5).....	47
Table 4.1 Contact resistance from I-V curves for ta:C and N-ta:C films.....	67
Table 5.1 FIA-EC data of 30 sccm N-ta:C film for dopamine.....	98
Table 5.2 FIA-EC data of 30 sccm N-ta:C film for norepinephrine.	98

LIST OF FIGURES

Figure 1.1 Ternary phase diagram of C, H, system showing a-C:H and ta-C. ²¹ (Reprinted with permission from <i>Materials Science and Engineering R</i> .37,129(2002).Copyright(2012)Elsevier. For interpretation of the references to color in this and all other figures, the reader is referred to the electronic version of this dissertation)	4
Figure 1.2 Schematic diagram of σ and π states in amorphous carbon. ³⁰ (Reprinted with permission from <i>Diamond and Related Materials</i> . 6,212(1997).Copyright (2012) Elsevier.).....	6
Figure 1.3 Proposed microstructure for tetrahedral amorphous carbon (ta:C) from reference 73. (a) The complete 64 atom structure. (b) The three- and four- membered ring present in the structure. (c) The 22 sp^2 hybridized carbon atoms showing how the group into clusters.....	16
Figure 2.2 Design of single compartment, three-electrode glass cell. ¹¹	24
Figure 2.4 Design of the thin-layer electrochemical cell. ⁸¹ A: rubber gasket; B: working electrode; C: rubber backing; D: screw clamp; E: Kel-f body, bottom piece; F: current collector; G: working electrode; H: Kel-f body, top piece.	26
Figure 2.5 Schematic of electronics system combined with a NanoScope IIIa scanning probe microscope for performing CP-AFM measurements.....	26
Figure 2.6 Schematic of CP-AFM tip current measurement circuit.	29
Figure 2.7 Schematic of electrical connection between ta:C films and Au-coated tip in CP-AFM.	30
Figure 3.1 (A) XPS survey spectra for a ta:C film and a N-ta:C film deposited with 30 sccm N ₂ . (B) Expanded XPS survey spectra for C1s and N1s peak from (A). (C) Plot of the O/C and N/C atomic ratio for different ta:C films as a function of the N ₂ flow used during the deposition.....	34
Figure 3.2 Height-mode of AFM images of ta:C and N-ta:C films deposited with 10, 30 and 50 sccm of N ₂	36
Figure 3.3 (A) Electron energy loss spectra (EELS) at the C K edge for (A) ta:C and N-ta:C films deposited with 10, 30 and 50 sccm N ₂ . (B) Reference spectra for single crystal diamond (pure sp^3) and multiwall carbon nanotubes (pure sp^2).	38
Figure 3.4 Visible Raman Spectra (514.5 nm) for ta:C and N-ta:C films deposited with 10, 30 and 50 sccm N ₂	41

Figure 3.5 Cyclic voltammetric *i-E* curves for ta:C, N-ta:C films grown with 10, 30 and 50 sccmN₂, glassy carbon and a boron-doped diamond thin film, all in 1M KCl. Scan rate = 0.1 V/s. Geometric area = 0.2 cm². 43

Figure 3.6 Capacitance-potential profiles for ta:C (○), 10 sccmN-ta:C(△), 30 sccmN-ta:C (▽), and 50 sccmN-ta:C (◇) films in 0.1 M HClO₄. Comparison data for glassy carbon and boron-doped diamond are presented. Capacitance values were determined using a 10 mV sine wave at 40 Hz. $Z_{im} = 1/2\pi fC_{dl}$. Data are normalized to the geometric area, 0.2 cm². 44

Figure 3.7 Cyclic voltammetric *i-E* curves with iR correction for ta:C (A), 10 sccm N-ta:C (B), 30 sccm N-ta:C (D), 50 sccm N-ta:C (E) in 1 mM Ru(NH₃)₆^{2+/3+} in 1 M KCl. Scan rate = 0.1 V/s. Geometric area = 0.2 cm². 46

Figure 3.8 Cyclic voltammetric *i-E* curves with iR correction for ta:C (A), 10 sccm N-ta:C (B), 30 sccm N-ta:C (D), 50 sccm N-ta:C (E) in 1 mM Fe(CN)₆^{3-/4-} in 1 M KCl. Scan rate = 0.1 V/s. Geometric area = 0.2 cm². 47

Figure 3.9 Cyclic voltammetric *i-E* curves for (A) GC and (B) a 30-sccm N-ta:C film (B), in 0.1 M H₂SO₄ (—), in 10 μM methylene blue solution (---) and after soaking(...). Scan rate = 0.025 V/s, Geometric area = 0.2 cm². The inserted were cyclic voltammetric *i-E* curves in 10 μM methylene blue after background subtraction. 50

Figure 3.10 Cyclic voltammetric *i-E* curves for (A) a ta:C film and (B) GC in 0.5 M H₂SO₄ before polarization and after polarization. Scan rate = 50 mV/s. Electrode area = 0.2 cm². 53

Figure 4.1 AFM images (1×1μm²) for 10 sccm N-ta:C film: (A) height mode; (B) deflection mode and (C) conductivity mode..... 63

Figure 4.2 CP-AFM images with line profiles (1×1μm²) for 10 sccm N-ta:C film at bias voltages of (A) +0.2 V or (B) -0.2 V. 65

Figure 4.3 CP-AFM images (1×1μm²) for 10 sccm N-ta:C film with bias voltage of (A) +0.2 V, (B) + 0.4 V, (C) + 0.6 V and (D) + 0.8 V. 66

Figure 4.4. Current vs bias voltage curve for 10 sccm N-ta:C film. 66

Figure 4.5 CP-AFM images (1 ×1μm²) for (A) ta:C, (B) 10 sccm, (C) 30 sccm and (D) 50 sccm N-ta:C films at a bias voltage of + 0.2 V. The current ranged from 0 to 0.07 μA..... 68

Figure 4.6 General principle of the positivefeedback mode for an SECM measurements. 71

Figure 4.7 Cyclic voltammetric *i-E* curve for the Pt microelectrode in 0.1 mol/L HClO₄ at 0.05 V/s. 73

Figure 4.8 Cyclic voltammetric *i-E* curve for Pt microelectrode in 1 mmol/L Fe(CN)₆⁴⁻/1M KCl. Scan rate = 0.05 V/s. 73

Figure 4.9 Fundamental principles of an SECM measurement. (A) Tip is far away from substrate (hemispherical diffusion). (B) Tip is close to the substrate (regeneration reaction or positive feedback). (C) Tip is close to the substrate (hindered diffusion or negative feedback). 74

Figure 4.10 Approach curves for ta:C and N-ta:C films in 1 mM Ru(NH₃)₆^{3+/2+}/1M KCl. The microelectrode was held at -0.3 V and the substrate was held at 0 V vs Ag/AgCl. $L=d/a$, where d is the distance between the tip and the substrate, a is the tip radius. i_T is the tip current and $i_{T,\infty}$ is the limiting current. 76

Figure 4.11 Approach curves for ta:C and N-ta:C films in 1 mM Fe(CN)₆^{3-/4-}/1M KCl. The microelectrode was held at 0 V and the substrate was held at +0.4 V vs Ag/AgCl. $L=d/a$, where d is the distance between the tip and the substrate, a is the tip radius. i_T is the tip current and $i_{T,\infty}$ is the limiting current. 77

Figure 4.12 Feedback mode SECM images ($500 \times 500 \mu\text{m}^2$) in 1 mM Ru(NH₃)₆^{2+/3+} + 1M KCl at (A) ta:C, (B) 10 sccm N-ta:C, (C) 30 sccm N-ta:C, and (D) 50 sccm N-ta:C films. In all cases, the Pt probe tip diameter was 5 μm . The tip potential was - 0.3 V and the substrate potential was 0 V vs Ag/AgCl. 80

Figure 4.13 Feedback mode SECM images ($500 \times 500 \mu\text{m}^2$) in 1 mM Fe(CN)₆^{3-/4-} +1M KCl at (A) ta:C, (B) 10 sccm N-ta:C, (C) 30 sccm N-ta:C and (D) 50 sccm N-ta:C films. In all cases, the Pt probe tip diameter was 5 μm . The tip potential was 0 V and the substrate potential was 0.4 V vs Ag/AgCl. 81

Figure 5.1 (A) Cyclic voltammetric *i-E* curves at scan rate of 0.025 V/s for 30 sccm N-ta:C film in: 0.1M PBS (—), in 10 μM dopamine(---) and in 0.1M PBS buffer after soaking(...); (B) Cyclic voltammetric *i-E* curves of first scan after background subtraction in 10 μM dopamine at scan rate(ν) of 0.025, 0.050, 0.100, 0.200 and 0.300 V/s, the insert graph was the i_p^{ox} vs $\nu^{1/2}$. Geometric area = 0.2 cm^2 88

Figure 5.2 (A) Cyclic voltammetric *i-E* curves at scan rate of 0.025 V/s for 30 sccm N-ta:C film in: 0.1M PBS buffer(—), in 10 μM norepinephrine (NE)(---) and in 0.1M PBS buffer after soaking(...); (B) Cyclic voltammetric *i-E* curves of first scan after background subtraction in 10 μM norepinephrine(NE) at scan rate(ν) of 0.025, 0.050, 0.100, 0.200 and 0.300 V/s, the insert graph was the i_p^{ox} vs $\nu^{1/2}$. Geometric area = 0.2 cm^2 89

Figure 5.3 Background Hydrodynamic voltammetric *i-E* curves in 0.1M PBS (pH=7.2)for (■) glassy carbon(GC), (●) boron-doped diamond(BDD) and (□) a 30 sccm N-ta:C films. Flow rate = 1.0 mL/min. Electrode geometric area = 0.12 cm² 90

Figure 5.4 Hydrodynamic *i-E* curves for 50 μM norepinephrine (NE) in 0.1 PBS (pH=7.2) at a 30 sccm N-ta:C film., Flow rate = 1.0 mL/min. Electrode geometric area = 0.12 cm² 91

Figure 5.5 The amperometric response of a 30 sccm N-ta:C film to 30 consecutive injections of dopamine over a 15 minute period (1 and 100 μM) in 0.1M PBS buffer (pH=7.2) with detection potential of 0.65 V, flow rate of 1.0 mL/min..... 95

Figure 5.6 FIA-EC response of a 30 sccm N-ta:C film for 1μM DA (■) and 1 μM NE(●) in 0.1M PBS (pH=7.2) buffer recorded over a 6-h period. Mobile phase was PBS buffer (pH=7.2), flow rate = 1.0 mL/min, electrode area = 0.12 cm² . Each data point was calculated from 5 injections with interval of 30 second. The error bars were within the size of the marker. 96

Figure 5.7 Calibration curves obtained for (A) dopamine and (B) norepinephrine for 30 sccm N-ta:C film . Mobile phase was 0.1 M PBS buffer (pH=7.2), flow rate = 1.0 mL/min, applied potential was 0.65 V for dopamine and 0.55 V for norepinephrine. 97

Chapter 1. Introduction

1.1 Overview of ta:C films

In electroanalytical measurements, an electrode material ideally possesses several important properties: low background current, relatively rapid rates of electron transfer, good mechanical properties, high sensitivity, and good reproducibility and stability. As a traditional electrode, sp^2 -bonded carbon (glassy carbon or graphite) has been widely applied and extensively studied in electrochemistry.¹⁻² Glassy carbon, pretreated by traditional polishing or laser activation, has a double layer capacitance of 24-36 $\mu\text{F}/\text{cm}^2$, and a heterogeneous electron-transfer rate constant (k^0) for $\text{Ru}(\text{NH}_3)_6^{+2/+3} > 0.4 \text{ cm}^2/\text{s}$ and $0.46 \text{ cm}^2/\text{s}$ for $\text{Fe}(\text{CN})_6^{3-/4-}$.³

Although sp^2 -bonded carbon has excellent electrochemical properties, there are some limitations with its use. Graphite has a layered, planar structure. In each layer, the carbon atoms are arranged in a [hexagonal lattice](#) with separation of 0.142 nm, and the distance between planes is 0.335 nm. The two known forms of graphite, *alpha* (hexagonal) and *beta* ([rhombohedral](#)), have very similar physical properties (except that the [graphene](#) layers stack slightly differently). The top of the layer graphene sheets is referred to as the “basal plane” while the edges of the sheets are referred to as the “edge plane”. The carbon atoms in the basal plane are generally unreactive with air except at elevated temperatures. The edge plane sites are prone to reaction with oxygen and water to form a variety of carbon-oxygen functional groups, such as carbonyls, ethers and carboxylic acids. The fraction of edge plane exposed in a graphitic material and the chemical functionalities terminating these sites strongly control many of the properties of the material, including the electrochemical behavior.² In electrochemical measurements, strong molecular

adsorption of polar molecules generally occurs and this adsorption can lead to electrode fouling. Another challenge to working with graphitic carbons is control of the surface chemistry. A wide variety of functional groups terminate the edge plane sites. Many redox systems have heterogeneous electron-transfer rate constants that are quite sensitive to the presence of certain functional groups (e.g., $\text{Fe}^{+3/+2}$)⁴⁻⁷. Therefore, reproducibly controlling the types of functional groups and their coverage is of paramount importance for high quality electrochemical measurements. Controlling this surface chemistry can be a challenge.

Boron-doped diamond (BDD) is another useful electrode material consisting of tetrahedral-coordinated sp^3 bonded carbon. This bonding produces a material with very high hardness. Diamond is one of mother nature's best electrical insulators and is normally not useful as an electrode because of low electrical conductivity. However, the conductivity can be significantly increased to levels similar to glassy carbon by substitutionally inserting boron during the diamond deposition process. Boron doping levels above the metal-semiconductor transition of $\sim 5 \times 10^{20} \text{ cm}^{-3}$ are common for chemical vapor deposited diamond⁸⁻⁹. Such high doping produced thin film electrodes with resistivities below $0.05 \Omega \cdot \text{cm}$. In electroanalytical measurements, boron-doped diamond offers advantages of: (1) low detection limits with superb precision and stability; (2) the ability to withstand high potentials and high current densities ($1-10 \text{ A/cm}^2$) in aggressive solution environments with little morphological or microstructural degradation; (3) optically transparency in the ultraviolet-visible (UV-Vis) and infrared (IR) regions for spectroelectrochemical measurements.¹⁰ The double-layer capacitance (C_{dl}) of boron-doped diamond is in the range of $5-10 \mu\text{F/cm}^2$. For $\text{Ru}(\text{NH}_3)_6^{3+/2+}$, k^0 is 0.012 cm/s and for

$\text{Fe}(\text{CN})_6^{3-/4-}$ the value is 0.017 cm/s.¹¹ An important feature of diamond is its microstructural and chemical stability as compared with graphitic electrodes. The stable surface structure and chemistry leads to improved response reproducibility and stability in electroanalytical measurements such as amperometric detection¹²⁻¹⁴. Diamond electrodes generally need little if any pretreatment prior to and they are resistant to fouling due to weak molecular adsorption particularly for polar molecules¹⁵⁻¹⁷.

Even though BDD has been successfully used electroanalytical measurements, there are some drawbacks with its use.¹⁸ First, in order to enhance the initial nucleation density for diamond growth chemical vapor deposition method (CVD), the substrate must to be properly pretreated. A common method is to use mechanical polishing or sonication with small diameter diamond powder (0.01-1 μm diameter) to scratch and to seed the surface with diamond particles. This process takes time and the quality of pretreatment impacts the quality of the diamond film grown. Second, the growth temperature for CVD diamond is $> 700^\circ\text{C}$. This limits the substrate choices to those that can withstand these temperatures with no phase change and those that form carbide interfacial layers¹⁹. Third, the growth time for achieving continuous films can be long (3-10 hours).

The ability of carbon to adopt different types of bonding makes it possible to synthesize pure carbon materials with different properties²⁰. Amorphous carbons contain a mixture of sp^2 and sp^3 -bonded carbon. Amorphous carbon means that there is a random arrangement of the

sp^3 and sp^2 carbon domains with no long-range order. A wide range of amorphous carbon materials, with or without hydrogen, can be prepared synthetically by controlling the ratio of sp^3 - sp^2 carbon.

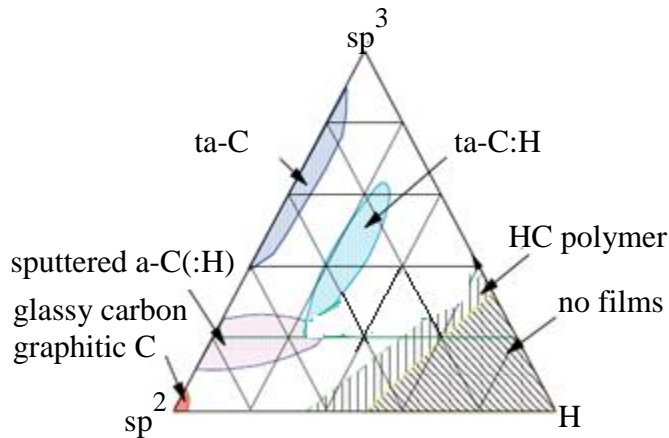


Figure 1.1 Ternary phase diagram of C, H, system showing a-C:H and ta-C.²¹ (Reprinted with permission from *Materials Science and Engineering R.37,129(2002)*. Copyright(2012)Elsevier .For interpretation of the references to color in this and all other figures, the reader is referred to the electronic version of this dissertation)

Figure 1 shows a ternary phase diagram displaying different compositions of amorphous carbon, of which diamond-like carbon and tetrahedral amorphous carbon (ta:C) are subtypes, These microstructural-different materials are shown with respect to their sp^2 - sp^3 -bonding and hydrogen content.²¹ ta:C materials can be prepared with no hydrogen and up to 85% sp^3 carbon²².

These materials can be deposited by several methods involving the deposition of energetic carbon ions²³⁻²⁹. Many properties of ta:C depend directly on the fraction of sp^3 carbon including the density and band gap. Given the limitations of diamond discussed above and the fact that ta:C materials can be made to have properties similar to those of diamond, there are several reasons for using ta:C films as electrochemical electrodes. These include the low growth temperature (25-100 °C), which opens the door to using a wider range of substrate materials. Another is the short deposition times for formation of a continuous film (minutes

rather than hours). Finally, another benefit is the availability of commercial reactors capable of coating many substrates during a deposition run.

Of course, for these ta:C films to have utility as electrochemical electrodes, they must possess high electrical conductivity. There are general two types of carbon bonds in ta:C film, sp^3 -bonded and sp^2 -bonded. In sp^3 -bond configuration, four valence electrons in a carbon atom are located in a tetrahedral- sp^3 -orbital and each one can form strong σ bond with an adjacent atom. In sp^2 -bonded configuration, three of the four valence electrons are located in trigonal- sp^2 -orbitals, which form three σ bonds in a plane. The fourth electron enters in a $p\pi$ orbital and forms π bond with a neighboring $p\pi$ orbital. sp^1 -bonded carbon is unusually existed in ta:C films, which has two $p\pi$ bonds and two σ bonds. In Figure 3, the σ bond from sp^3 and sp^2 -bonded carbon forms occupied σ states in the valence band and empty σ^* states in the conduction band. The π bonds form filled π states and empty π^* states. The σ - σ^* gap is much wider than the π - π^* gap. Robertson et al, developed a very simple mode to describe the atomic structure (Figure 1.3).³⁰ The maximized π bonding energy leads the sp^2 sites to form cluster of π bonds in a sp^3 -bond matrix and the band gap is determined by the cluster size.

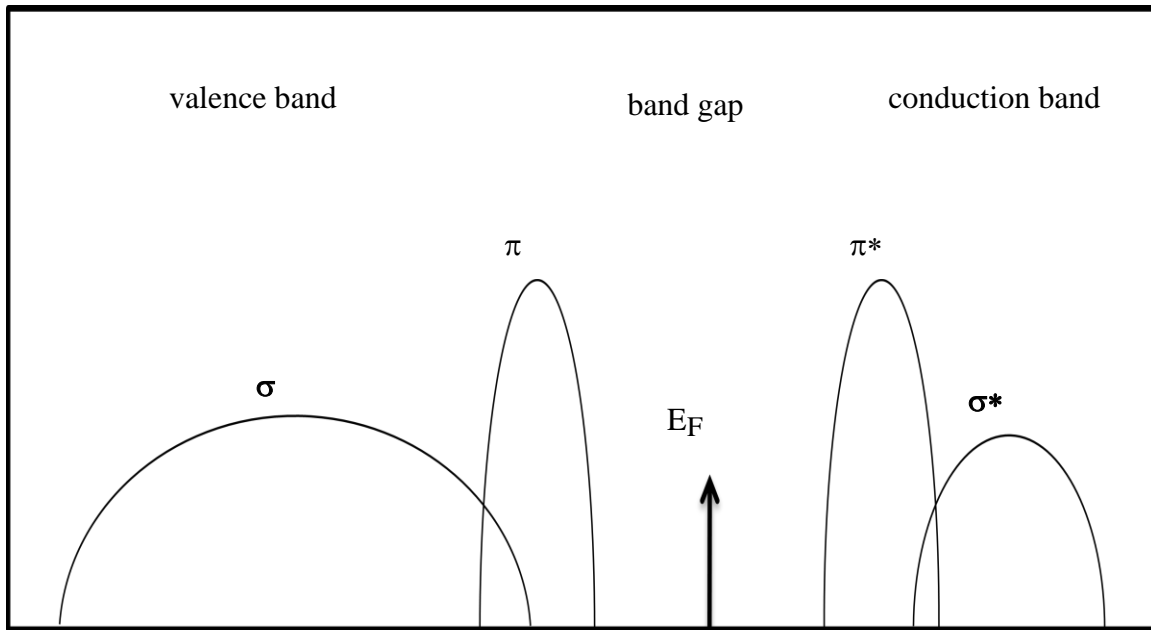


Figure 1.2 Schematic diagram of σ and π states in amorphous carbon.³⁰ (Reprinted with permission from *Diamond and Related Materials*. 6,212(1997). Copyright (2012) Elsevier.)

High quality, as-grown ta:C is a p-type semiconductor with an optical gap of about 2 eV due to $\pi \rightarrow \pi^*$ transitions³⁰⁻³¹. The electronic density of states (DOS) consists of two types of states. The σ bonds of sp^3 and sp^2 sites form σ states in the valence band and σ^* states in the conducting band separated by a band gap of about 5 eV. The sp^2 bonded carbon possesses π states that give rise to filled and empty π and π^* states that lie closer to the Fermi level within the σ - σ^* gap³². The π states therefore control the optical gap and the electronic properties of the films. Therefore, the electrical conductivity of ta:C films increases proportionally with the sp^2 -bonded carbon content in the films. In order to understand the electrochemical properties of these new electrode materials, it is important to consider (i) the sp^3 – sp^2 carbon ratio; (ii) the clustering of the sp^2 domains in the film; (iii) the impurity content (doping with B, N, and metals).

Robertson and coworkers have been studying the electronic and atomic structure of diamond-like carbon materials, in particular ta:C, films for many years and their publications have covered the growth mechanism, microstructural analysis and electronic properties.^{20-21, 33-}

⁴² DLC films can be deposited by several methods, including ion beam, mass selected ion beam (MSIB) and filtered cathodic vacuum arc (FCVA). The beam contains energetic carbon ions, typically ions with 20-100 eV of energy. A fraction of beam with neutral or low energy atoms forms an sp^2 layer on the original surface. Another fraction of the beam penetrates the surface and forms sp^3 bonded carbon. The sp^3 content depends on ion energy and growth temperature.³⁹

1.1.1 Growth of ta:C Films

Since the first reported diamond-like carbon film growth reported by Aisengerg and Chabot in 1971 using ion beam deposition,⁴³ DLCs have been widely used as coating materials in industry. Various deposition methods are available for growing DLC. There are four main categories: ion beam, pulsed laser deposition, sputtering and plasma enhanced chemical vapor deposition (PEVCD). The quality of DLC materials in terms of the sp^3/sp^2 carbon ratio, intrinsic stress, smoothness, density, optical gap and electronic properties depend strongly on the deposition method and conditions. One important parameter is the energy of the carbon ions formed and used for film growth. If a carbon ions possess ca. 100 eV, with a narrow energy distribution, DLC films will generally be of high quality.²⁴

In ion beam deposition, carbon ions are formed by the plasma sputtering of a graphite cathode or generated by a hydrocarbon gas ionization in plasma. The carbon ions or hydrocarbon

ions are accelerated in high vacuum chamber. Since the ion is accelerating at a finite pressure, the ion beams contains a large amount of unionized neutral species.

There are several methods to minimize the content of neutral species. One is mass selected ion beam deposition (MSIB).²⁵⁻²⁶ These accelerated ions passed through a magnetic filter. The selected ions with a certain e/m ratio could pass through the filter and will be decelerated before reaching the substrate. This method is used in laboratory to produce ta:C film. It is a controllable process and the energy of the ions could be adjusted. In this method, the deposition rate is very low (0.001 Angstrom/s), the cost is high because of the magnetic filter.

The sputtering deposition method is commonly used in industry, for example the coating of cutting tools.⁴⁴⁻⁴⁵ An Ar plasma interacts with a graphite electrode to form a dc or rf sputtering of carbon ion. Magnets are applied to increase the ionization process. A dc bias could be applied to control the ion energy. By changing the gas source, other element could be incorporated, such as nitrogen. The reason for sputtering to be widely used in industry is versatile scalability. The scale of deposition could be changed according to the application. Since the ions also contain neutral species, the hardness of these DLCs is not high.

For pulsed laser deposition, a pulsed excimer laser vaporizes carbon from a graphite source to form intense plasma containing carbon ions.^{27, 46-47} The intense plasma ion is accelerated before reach the substrate in the high vacuum chamber. The PLD could produce ta:C films as FCVA and MSIB. It could be used to deposit different types of materials, such as

hard coating materials and high temperature superconductors. In this process, the formation of ta:C film is strongly depend on the energy of the accelerated plasma ion. The high current charge between anode and cathode increases ionization energy of these carbon ions. The high kinetic energy of the carbon ions is critical to form ta:C films with high sp^3 -carbon content. Another important parameter during the deposition process is the deposition temperature. The typical temperature for PLD process is 25-100 °C. The relative low temperature expands the choices for substrate. In higher temperature (> 150 °C), the film properties will transit from diamond-like carbon to graphite-like.⁴⁸

Radio-frequency plasma enhance chemical vapor deposition is the most popular deposition in laboratory.²⁸⁻²⁹ In this deposition system, there are two electrodes. One is the substrate, where the rf power is capacitively couples. Another one is usually the reactor wall and is grounded to the earth. The rf power forms a plasma between the two electrodes.

1.1.2 Characterization of ta:C films

To characterize ta:C films, there are several key parameters: (1) the content of sp^3 -bonded carbon; (2) the ordering of the sp^2 -bonded carbon, which determines the electronic properties;(3) impurity(nitrogen) role in the deposition process. There are various methods to characterize these parameters. Each method has its own advantages and weakness.

Electron energy loss spectroscopy (EELS) is the most commonly used method to derive sp^2 -bonded carbon ratio for ta:C films now.^{20, 49-50} In EELS, an electron beam interacts with

the ta:C films and is inelastically scattered. There are two energy loss regions, the low energy loss region (0-40 eV) and the high loss energy region for the carbon K edge (ca. 285 eV). For the carbon K edge spectrum, there are mainly two peaks. One peak at 285 eV originates from the excitation to $p\pi^*$ states of sp^2 -bonded carbon. Another peak at 290 eV originates from excitation to $p\sigma^*$ states of sp^3 and sp^2 -bonded carbon.⁵¹ Disordered graphite is generally used as a reference of 100% content of sp^2 -bonded carbon. By comparing the area ratio between the 280~285 eV and 285~290 eV with the reference, the content of sp^2 -bonded carbon in the film could be calculated. Another method to compare the area ratio is fitting the σ^* area from 290 eV with a Gaussian.

There are several limiting factors in EELS. First, this method is destructive since the substrate has to be removed. Second, this technique requires the film thickness less than 20 nm to avoid multiple scattering. Third, it is time-consuming. It usually takes several hours to obtain spectra. Fourth, the reference for the pure 100% sp^2 -bonded carbon needs to be randomly oriented. Otherwise the π^*/σ^* area ratio will depend on the local orientation of the graphite plane and it would not be a constant.

Raman spectroscopy is widely used in the characterization of ta:C films since it is rapid, nondestructive. Visible Raman is only sensitive to sp^2 -bonded carbon because the scattering cross-section coefficient of sp^2 -bonded carbon is 50~230 larger than that of sp^3 -bonded carbon.⁵²⁻⁵³ But the UV Raman, which could excite the σ states of both sp^2 and sp^3 -bonded

carbon, can directly tell the content of sp^3 -bonded carbon. By comparing the UV Raman spectra of ta:C to visible Raman spectrum, there is a new peak (T peak) at ca. 1100 cm^{-1} .⁵⁴⁻⁵⁶ The broad peak at ca 1650 cm^{-1} is the feature of sp^2 -bonded carbon and is composed of so-called D and G peaks.²¹ Raman spectrum reflects peaks in the vibrational density-of-states (VDOS) of ta:C films. The expected maximum of VDOS of a fully sp^3 -bonded random network is ca. 1100 cm^{-1} , where the T peak is. UV Raman excites at 244 nm, which corresponds excitation energy of 5.1 eV. This energy is high enough to excite the σ states in sp^2 and sp^3 -bonded carbon. The simulations of ta:C film prove that T peak is due to sp^3 -bonded carbon.⁵⁷ By fitting the two peaks with Lorentzians function, the peak intensity ratio ($I(1100)/I(1100)+I(1650)$) increases with increasing the content of sp^3 -bonded carbon. Recently, Cui et al, published a paper about the quantitative measurements of sp^3 content in both hydrogen-free and hydrogenated DLC films.⁵⁸ For Hydrogenated DLC films, the following equation has been established:

$$sp^3\text{ content} = -0.07 + 2.50 \times \text{Disp}(G) [\text{cm}^{-1}/\text{nm}] \pm 0.06,$$

Disp(G) is the dispersion rate of the G peak in UV and Visible Raman. For hydrogen-free DLC films,

$$sp^3\text{ content} = -2.05 + 1.90 \times 10^{-2} W - 3.01 \times 10^{-5} W^2 \pm 0.08,$$

where W is the FWHM(G). By comparing the calculated results with the published or independently measured sp^3 content values, these two equations give acceptable results.

There are other methods which could be applied to measure the sp^2 or sp^3 fraction, such as NMR. NMR could directly measure the content of sp^3 -bonded carbon since each hybridization of carbon has a unique chemically-shift peak in C^{13} -NMR. But this method is also destructive and needs large amount of sample.

1.2 Review of the Electrical and Electrochemical Properties

In ta:C film, there are two carbon hybridizations, sp^3 and sp^2 . In sp^2 configuration, three of the four valence electrons in a carbon atom are in trigonal sp^2 orbital, σ bonds and the fourth electron is in the π orbital. While in sp^3 configuration, four valence electrons are all in tetrahedral sp^3 orbital. The π orbital forms π bond with adjacent atoms and this controls the electronic properties. The mechanical properties and hardness are controlled by the σ bonds in the film. Pure ta:C film is weakly p-type semiconductor with a band gap around 2 eV.⁵⁹ The introducing of nitrogen in the ta:C film can have two functions. One is moving the Fermi level to the conduction band. Another one is narrowing the band gap, which is controlled by the π bonds in the film. The electrical conductivity of the film is changed by either one.^{42, 60-61} The incorporation of nitrogen can change the ta:C film to be n-type semiconductor and the electrical conductivity is increased. Robertson et al. reported the conductivity of ta:C film increased from $10^{-8} /(\Omega \cdot \text{cm})$ to $10^{-2} /(\Omega \cdot \text{cm})$ by increasing nitrogen to 10%.⁴¹ In 2011, Honda et al. applied hall measurement to measure the electrical properties of N-doped DLC.⁶² The undoped DLC films exhibited no conductivity. The hall coefficient of N-doped DLC film was $-3.63 \text{ cm}^3 \text{C}^{-1}$. The

negative value implied the n-type conduction. The carrier concentration was $1.625 \times 10^{18} \text{ cm}^{-3}$.

The resistivity was $0.695 \text{ } \Omega\cdot\text{cm}$. The carrier concentration was $5.38 \text{ cm}^2 \text{ V}^{-1} \text{ s}^{-1}$.

The DLC film has been widely used as a protective coating material in magnetic storage disks, biomedical coating for many years due to its high mechanical hardness, chemical inertness. In 1999, Dr Miller's lab at Case Western Reserve University, first reported on the use of N-ta:C films as electrochemical electrodes.⁶³ The taC:N film were deposited by a filter cathodic arc deposition and had 70-80% of sp^3 carbon. Nitrogen content was ca 10% by Auger spectra with film thickness about 40 nm. By comparison with boron-doped diamond, their taC:N film had a wider potential window in 1M HClO_4 , reversible behavior with outer sphere redox couples (1 mM $\text{Ru}(\text{NH}_3)_6\text{Cl}_3$ + 1 mM Co(III)-sepulchrate in 1M KCl), faster electron-transfer rate for the quinone/hydroquinone couple and higher catalytic activity for Cl_2/Cl^- with high stability. The taC:N film was grown at ambient temperature, which expanded the substrate choices and applications. They predicated the great future of the taC:N film to the electroanalytical and electrosynthetic applications.

In 2002, they used the taC:N film for the detection of dopamine with rotating disk electrodes and the detection limit could reach 200 nM at physiological pH.⁶⁴ Liu et al, reported a conductive nitrogen-doped diamond-like carbon film (N-DLC) with excellent electrochemical behavior.⁶⁵ This N-DLC was deposited with DC magnetron sputtering system and annealed at

250°C in the deposition chamber in nitrogen gas pressure of 10^{-4} Torr for 5h. The sheet resistance for this N-DLC by four-point probe was $2.5 \times 10^2 - 5.7 \times 10^3 \Omega$ per square. The N-DLC had wide potential window in several aqueous systems (3.55 V vs SCE in 0.5 M H_2SO_4 and 2.97 V vs SCE in 1M HClO_4). It also showed catalytic activity to the Cl_2/Cl^- reaction. In $\text{Fe}(\text{CN})_6^{4-}/\text{Fe}(\text{CN})_6^{3-}$, quasi-reversible behavior was observed with this N-DLC. In the detection of 1Mm Pb^{2+} in 0.1M KCl solution, high signal for Pb^{2+} and Pb^0 were shown in the cyclic voltammogram. They predicted the great promise of N-DLC in the environmental-friendly disposable electrodes.

There are other papers describing the electrochemical properties of nitrogen containing DLC.^{64, 66-70} However, there are very few papers explaining the relationship between the microstructure and electrochemical properties of n-ta:C films. Zeng et al. reported semiconductor properties of nitrogen-doped amorphous carbon (a-C:N) and correlated the film structure and molecular oxygen reduction.⁷¹⁻⁷² The capacitances of the three samples (a:C-N10, a:C-N20 and a:-C-N40)(10,20 and 40 were nitrogen flow rate(sccm) in the FCVA system) in 0.1M NaOH solution were dependent on the electrode potential. The sp^2/sp^3 ratio increased by increasing nitrogen flow rate. When these electrodes were immersed in solution containing O_2 or anion other than OH^- , the capacitance was due to the space-charge layer that formed in the electrode and Helmholtz layer that formed in the solution, which were in series. By comparing with the glassy carbon, the kinetics constant (k^0) for $\text{Fe}(\text{CN})_6^{4-/3-}$ was smaller due to absence of

electrons at the Fermi level. All of these proved the a-C:N were semiconductor. Thus, the sp^2/sp^3 ratio could be controlled to optimize the electrode sensitivity. Another research was reported at the same time about the correlation between film structures and potential limits for hydrogen and oxygen evolutions for these a-C:N films. A series of a-C:N films were grown in FCVA with different nitrogen flow rate. The sp^3 fraction of carbon was greatly decreased from 74.2% to 39.3% when the nitrogen flow rate varied from 10 sccm to 15 sccm. In the 0.1M H_2SO_4 , two potential limits (with current density of $100 \mu A/cm^2$ and $1000 \mu A/cm^2$) for dihydrogen evolution were evaluated and compared with glassy carbon. At current density of $100 \mu A/cm^2$, dihydrogen evolution potential limit for a-C:N varied from -1.35 V to -0.95V. For glassy carbon, it was -0.64V. At current density of $1000 \mu A/cm^2$, a-C:N films's potential limit varied from -1.54 V to -1.10 V. For glassy carbon, it was -0.86 V. In 0.1M NaOH, at current density of $100 \mu A/cm^2$, the dioxygen potential limits for a-C:N films changed from 1.45 V to 1.00 V and it was 0.72 V for glassy carbon. At current density of $1000 \mu A/cm^2$, it was 1.35 V for glassy carbon. The a-C:N films varied from 2.04 V to 1.42 V. For both the dihydrogen and dioxygen evolution, these a-C:N electrodes were more chemically inert than glassy carbon. By correlation the sp^3 fraction and potential limits of these two reactions, they found out that sp^3 -bonded carbon was the reason of higher kinetic barriers for the reduction of protons to dihydrogen and the oxidation of water to dioxygen. Also the sp^3 -bonded carbon had less adsorption sites for protons or hydronium ions than in the case of sp^2 -bonded carbon. According to different requirements in the electroanalysis, the fraction of sp^3 could be controlled to make the electrode with high or low resistance.

With the currently published papers, there is still incomplete understanding the structure-function relationships. In order to expand the application of these electrodes in electroanalytical area, more detailed information about the correlation between structure and properties (electrochemical, electronic) is going to be explored.

1.3 The microscopic structure of ta:C film

In terms of the microscopic structure of ta:C, Pailthorpe et al. proposed a structure consisting of 65% sp^3 -bonded and 35% sp^2 -bonded carbon, which has been widely used as the standard model for ta:C.⁷³

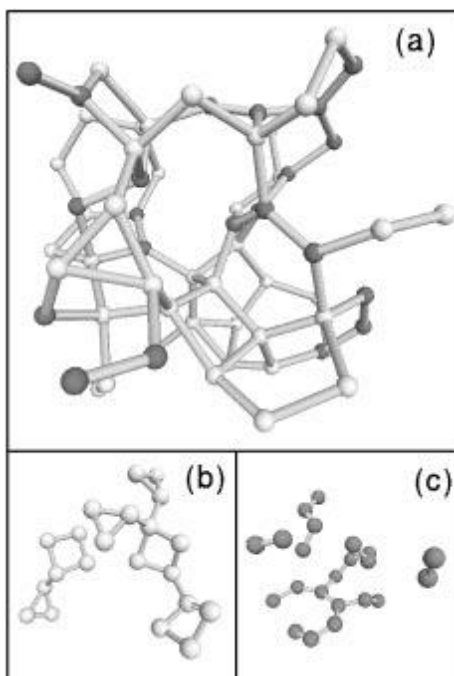


Figure 1.3 Proposed microstructure for tetrahedral amorphous carbon (ta:C) from reference 73. (a) The complete 64 atom structure. (b) The three- and four- membered ring present in the structure. (c) The 22 sp^2 hybridized carbon atoms showing how the group into clusters. Reprinted with permission from Marks, N.A.; McKenzie, D.R.; Pailthorpe, B.A.; Bernsasconi, M.; Parrinello, M. Physical Review Letters, 76, 768-771, 1996. http://prl.aps.org/abstract/PRL/v76/i5/p768_1.

The structure in Figure 1.3 is composed of 64 carbon atom (42 sp^3 -bonded and 22 sp^2 -bonded carbon). The three- and four-membered rings in Figure 1.3 (b) are mainly responsible for the mechanical properties (hardness). While in Figure 1.3 (c), the sp^2 -bonded carbon could be in either ethylenelike double bonds or in graphite-like forms. For the ta:C and N-ta:C films, the microstructure should be similar to this structure. The sp^2 -bonded carbon in ta:C and N-ta:C films should be not only in graphite-like form, but also in aliphatic form.

1.4 The influence of nitrogen to these properties

Pure ta:C films are a weak p-type semiconductor that could be translated to n-type with nitrogen incorporation.^{22, 74-76} According to Robertson's theory,⁴¹ at lower nitrogen level (< 1%), nitrogen does act as n-type dopant. The conductivity increases due to the Fermi level shift to the conduction band. At moderate nitrogen level (1%~10%), nitrogen helps the existing sp^2 -bonded carbon to cluster. The reason for the conductivity increasing is the reducing of the band gap because of clustering. When the nitrogen level is smaller than 10%, the sp^3 -bonded carbon and optical gap remain constant. At higher nitrogen level (> 10%), the content of sp^3 -bonded carbon decreases and new sp^2 -bonded carbon is formed as C=N. Therefore, the nitrogen in the deposition of ta:C film changes the electronic properties.

The doping efficiency for nitrogen in the ta:C film is very low due to two main reasons. One is the bonding configuration between N and C is very complicated. Besides the sp^3 and sp^2

substitutional sites, there are many non-doping sites such as pyridine, pyrrole and nitrile.^{41, 77}

Another reason for the low doping efficiency from Robertson et al is the large density of gap states of the ta:C film.²¹ The gas state density of ta:C is about 10^{20} cm^{-3} , which is four orders larger than amorphous Si:H. In order to have significant doping, the doping efficiency needs to be 10% for 1% N addition. Since the nitrogen could change the electrical and electrochemical properties of the ta:C film, it is possible to grow electrodes which match different requirements by controlling the nitrogen content in the film.

1.5 Hypothesis and Research

Even though there is published literature describing some of the basic electrochemical properties of ta:C and N-ta:C films, a complete understanding of how the physical, chemical and electronic properties affect the electrochemical activity remains to be determined. Therefore, the motivation for this work was to address this knowledge gap and to determine if the ta:C and N-ta:C films can be grown to possess properties more similar to those of boron-doped diamond.

The overall goal of this work was to determine the microstructure of the ta:C and N-ta:C films, as deposited by pulsed laser-arc deposition, and to correlate the film microstructure and electrical properties with the basic electrochemical properties. These include the background current, working potential window, capacitance, electron-transfer kinetics for redox systems and molecular adsorption. We tested the hypothesis that increased nitrogen incorporation would result in a greater fraction of sp^2 -bonded carbon in the films and that this would cause the electrochemical properties of the films to transition from ones more resembling diamond (sp^3 carbon) to ones more resembling glassy carbon (sp^2 carbon).

Aim 1: To determine the basic electrochemical properties of ta:C and N-ta:C films through studies of the electrochemical reaction rates of various inner and outer-sphere redox mediators, the adsorption of redox-active organic molecules, the double layer capacitance, and interfacial structure in various electrolyte solutions.

Aim 2: To determine the microstructure and chemical composition of the films using Raman spectroscopy, X-ray photoelectron spectroscopy (XPS) and electron energy-loss spectroscopy (EELS). These data will be important for understanding the microscopic and macroscopic structure, and the distribution and bonding of the incorporated nitrogen.

Aim 3: To determine the electrical properties and electrochemical activity spatially across the film surface using conducting-probe atomic force microscopy (CP-AFM) and scanning electrochemical microscopy (SECM).

Aim 4: To determine the electroanalytical utility of these new electrodes for the detection of various bioanalytes using flow injection analysis. The goal was to develop an electrode with as good or superior detection figures of merit to boron-doped diamond.

Chapter 2. Experimental Approach

2.1 Growth of ta:C films by Physical Vapor Deposition (PVD)

ta:C and N-ta:C films were grown on boron-doped Si(111 and 100) substrates ($\sim 10^{-3} \Omega\text{-cm}$) using pulsed laser-arc deposition (Laser-Arco system). This system works by laser-controlled, high pulsed-current cathodic vacuum arc deposition. In this process, a pulsed laser beam is rastered across a rotating graphite target (cathode) that is positioned near the substrate. Each laser pulse generates a small carbon-containing plasma discharge that rapidly expands away from the target toward the substrate (anode). Once the plasma reaches the substrate, a vacuum arc discharge is ignited between the target (graphite) and the substrate peak currents approach 1500 A. This deposition produces a thin but hard (30-60 GPa) and dense ta:C film. The nitrogen-incorporated films were deposited in the presence of nitrogen gas at flow rates of 10, 30 or 50 sccm (N-ta:C). This process incorporates nitrogen into the deposited ta:C films. The substrate temperature during deposition was *ca.* 100°C. The ta:C growth rate was approximately 2-3 $\mu\text{m/h}$. All films had a nominal thickness of *ca.* 200-nm, as determined by a Dektak Profilometer.

2.2 Physical and Chemical Characterization

2.2.1 Four-Point Probe Resistance Measurements

Four-point probe resistivity measurements were performed to determine the sheet resistance using a Model 302 Resistivity Stand (Lucas Signatone Corp.). In Figure 2.1, a constant current (I) was applied to the outer two probes (spacing = 0.1 cm) with the voltage drop (V)

between the inner two probes being measured with an HP 3748A multimeter (Hewlett-Packard, Palo Alto, CA). The current was applied using an HP E3612A DC power supply(Hewlett-Packard, Palo Alto, CA), which was modified to output currents in the range of 1nA - 0.5A.

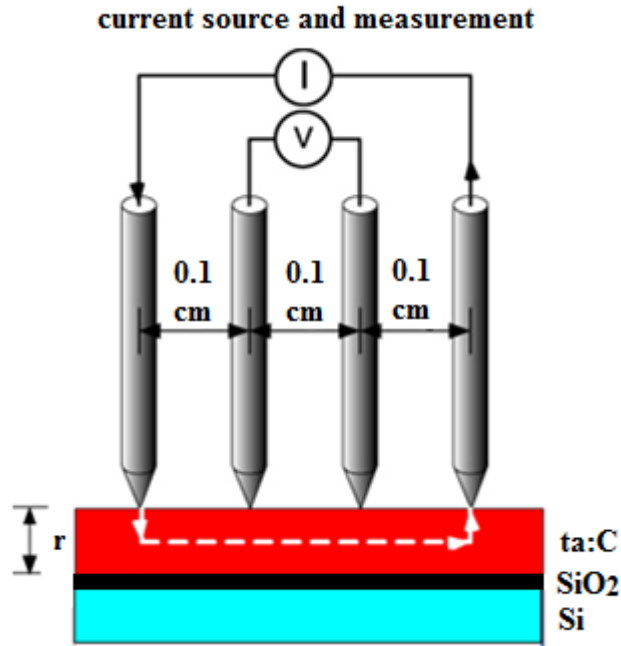


Figure 2.1 Schematic of the four-point probe measurement apparatus.

The resistance was determined from I-V data according to the following equation:

$$R=4.5324 \times V/I \quad [1]$$

where R is the resistance (Ω per square), V is the potential drop (volts) and I is the applied current (amperes).⁷⁸ All ta:C and N-ta:C films used in the resistivity measurements were grown

on SiO₂/Si with a thickness (SiO₂) of 500 nm. For each film, five different currents were applied (10-50 μ A) at each location on a film. Four random spots were measured for each film

The resistivity (ρ , ohm \times cm) was calculated from

$$\rho= R \times r \text{ (} r \text{ is the film thickness (cm))} \quad [2]$$

2.2.2 XPS

X-ray photoelectron spectra (XPS) were recorded using a Perkin-Elmer Phi 5400 ESCA system (Perkin-Elmer) with a magnesium $K\alpha$ X-ray source (1254 eV). Samples were analyzed at a base pressure near 10^{-9} torr with pass energy of 29.35 eV and a take-off angle of 45° . The spot size was roughly $250 \mu\text{m}^2$. The spectrometer was calibrated using the C1s line of graphite at 284.6 eV.

2.2.3 Raman Spectra

Raman microprobe spectra were collected at room temperature using aSpex 1250 spectrograph with a 600 groove/mm holographic grating (JobinYvon-Horiba) and 514.5 nm light from an argon ion laser for excitation. The detector was a Symphony 2000 \times 800 CCD (Horiba Jobin-Yvon) with a pixel size of 15 μm . Spectra were collected with an incident power density of ca. 1.4 kW/cm^2 (10 mW at the sample and 30 μm diameter spot size) and the integration time was 40 s. The spectrum was calibrated with single crystal diamond, which had the first-order phonon peak at 1332.6 cm^{-1} .

2.2.4 TEM

HRTEM images were collected using a field-emission microscope (JEOL-2200FS, Tokyo, Japan) operating at 200 keV. Electron energy loss spectra (EELS) were recorded with a Gatan 1024 \times 1024 detector for high quality STEM imaging and simultaneous EELS data collection. For the TEM images, a small thin section of a ta:C or a diamond film was placed on a Formvar/carbon-coated copper grid (Ted Pella #01883-F). EELS line scans were collected in the

STEM mode with an e-beam spot size of 0.7 nm. To limit any EELS background signal from the carbon-coated grid, signal was only collected only from film sections in the voids of the grid.

2.3 Electrochemical Characterization

2.3.1 Cyclic Voltammetry

The cyclic voltammetry measurements were carried out in a single compartment glass cell (Figure 2.2)¹¹ using a CHI650B potentiostat (CH Instruments, Inc., Austin, TX). A commercial Ag/AgCl “no-leak” minielectrode (3 M KCl, Dionex Corp.) was used as the reference and a platinum gauze served as the counter electrode. All of the films were pressed against a Viton o-ring placed at the bottom of the cell by a copper plate. The exposed geometric area was 0.2 cm².

All solutions were deoxygenated by purging with N₂ for 15 min prior to and blanketed with the gas during a measurement. All measurements were made at room temperature (23 ± 2°C).

In preparation for the electrochemical measurements, the film surface was exposed to ultrapure (distilled and stored over activated carbon) isopropanol for 20 min prior to use. This served to clean the surface and was the only electrode pretreatment used⁷⁹.

Comparison measurements were made with glassy carbon (GC-20, Tokai Ltd.), that was polished to a mirror-like finish with decreasing alumina grit sizes (1.0, 0.3 and 0.05 μm diam.). The grit was slurried in ultrapure water and the polishing was done on individual felt polishing pads (Buehler Ltd.). After each polishing step, the electrode received an ultrasonic cleaning in ultrapure water for 20 min to remove polishing debris. As a final cleaning step, the electrode was ultrasonicated second time for 20 min in ultrapure isopropanol. Like the ta:C films, the glassy

carbon surface was cleaned by exposure to ultrapure isopropanol for 20 min prior to making an electrochemical measurement.

Comparison measurements were also made with polycrystalline diamond. The hydrogen-terminated, boron-doped microcrystalline diamond thin-film electrodes were deposited on highly boron-doped Si substrates using a procedure described previously.⁸⁰ Prior to the electrochemical measurements, the films were cleaned by exposure to ultrapure isopropanol for 20 min.

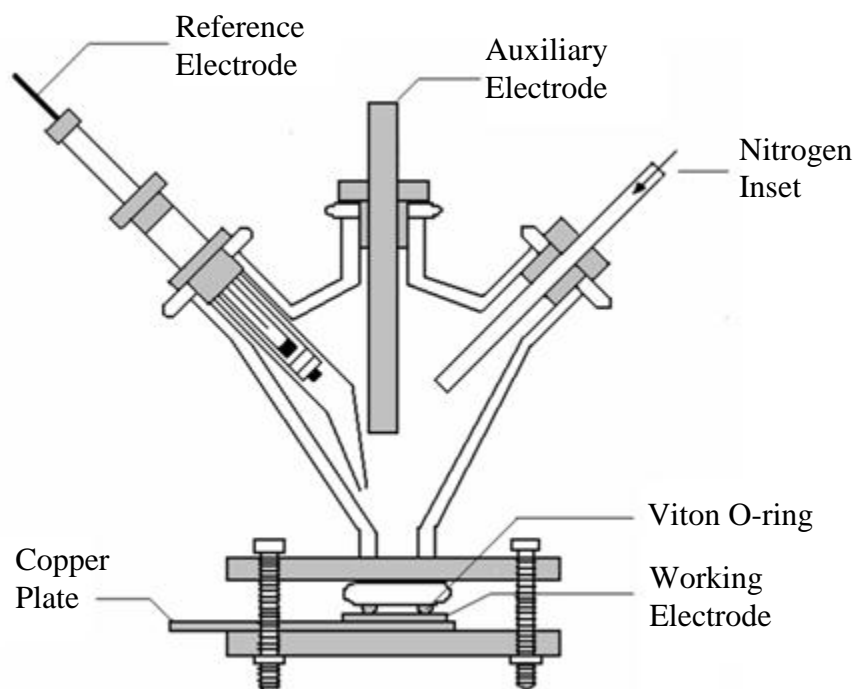


Figure 2.2 Design of single compartment, three-electrode glass cell.¹¹

2.3.2 Flow Injection Analysis(FIA)

The FIA system design is shown in Figure 2.3. It consisted of a model LP-21 (Scientific System, Inc.) pulse dampener, a model 7125 (Rheodyne) syringe-loaded injection valve with a 20 μ L injection loop, and a home-made thin layer cell constructed from Kel-F (Figure 2.4)⁸¹. A constant Metric II (Milton Roy) metering pump was used to propel the carrier solution throughout the rest

of the FIA system. A 0.1 cm-thick neoprene gasket separated the working electrode from the top section of the flow cell, with a rectangular groove (0.80 cm x 0.15 cm) defining the flow channel. The resulting surface area of the working electrode was 0.12 cm^2 , and the cell volume (assuming a 25% compression of the gasket) was estimated to be $9 \text{ }\mu\text{L}$. Electrical contact was made by pressing a piece of Cu foil against the back of the working electrode's conducting Si substrate. A commercial Ag/AgCl mini-electrode (3 M KCl, Dionex Corp.) was used as the reference, and the stainless steel tube leading from the flow cell to the waste line was used as the counter electrode. A calibrated flow rate of 1.0 mL/min was used for all analyses.

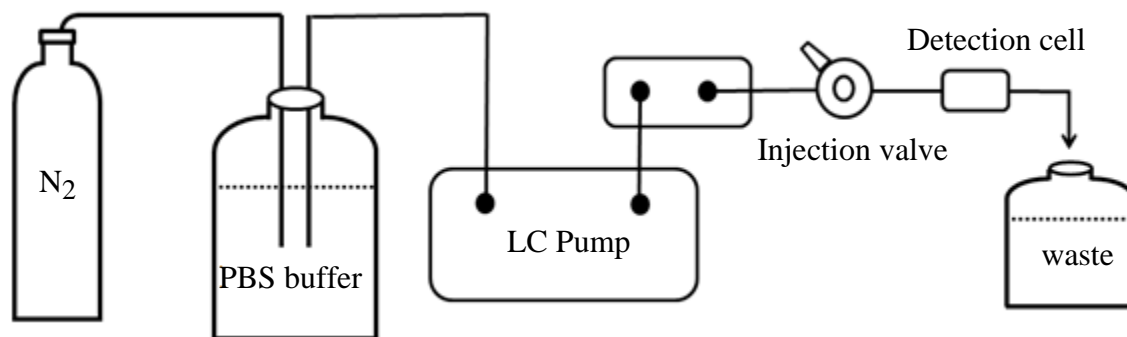


Figure 2.3 Diagram of the FIA system.

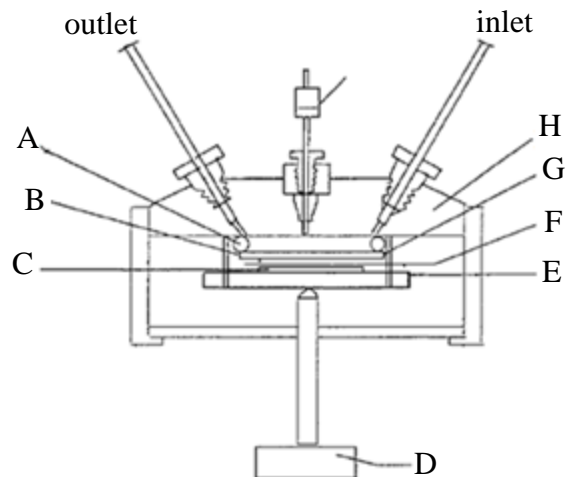


Figure 2.4 Design of the thin-layer electrochemical cell.⁸¹ A: rubber gasket; B: working electrode; C: rubber backing; D: screw clamp; E: Kel-f body, bottom piece; F: current collector; G: working electrode; H: Kel-f body, top piece.

2.4 Characterization by Scanning Probe Methods

2.4.1 Conductive-Probe Atomic Force Microscopy (CP-AFM)

CP-AFM was performed in air using a modified NanoScope IIIa instrument (Digital Instruments, CA), which is shown in Figure 2.5.

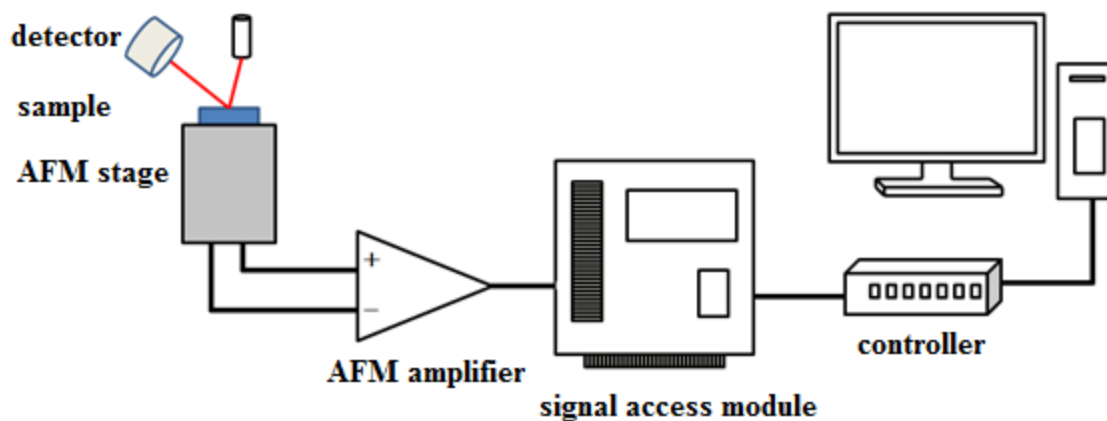


Figure 2.5 Schematic of electronics system combined with a NanoScope IIIa scanning probe microscope for performing CP-AFM measurements.

The conductivity measurement was carried out with a homemade AFM amplifier (Figure 2.6). DC1 was a +12 volt and -12 volt DC/DC convert. It supplied the balanced DC power for the amplifiers. IC1A is a current-to-voltage converter. IC1A is a very high gain amplifier with a 1 Megohm feed-back resistor. IC1A tried to keep pins 2 and 3 at the same potential. Pin 3 was at signal ground level (0 volt). Any current coming in on the connector X1 caused the opamp to generate a feedback current of the opposite polarity. The feedback current went through the 1 Megohm resistor. The circuit configuration was also inverting amplifier. The output was positive for negative input current and vice versa.

IC1B was configured as another inverting voltage amplifier. The gain was set by the ratio of R5, R6 and R1. The equation for the gain was:

$$\text{Gain}=(R1+R6)/R5$$

R1 was adjustable resistor which could go from 0 to 1000 ohms. So the range of the gain was 2.9 to 7.1. IC1B also had a second adjustable resistor which added positive or negative bias to allow the output to be zeroed. This compensated for internal DC offsets of the opamp and any external DC offsets. Since the signal goes through 2 stages of inversion the resulting output was the same polarity as the input.

All films were attached to a metal pod stage using either conducting carbon tape or Ag paint applied between the pod and the backside of the conducting Si substrate. A gold-coated, tetrahedral-shaped silicon nitride tip (Veeco NPG-20), with an radius of curvature less than 50 nm, a tip height of 15-20 μm and a full-tip cone angle less than 35° , was mounted on a rectangular cantilever. All tips were checked by SEM for shape and Au coating integrity before

use. The conductivity measurement was carried out with a home-made current-to-voltage converter circuit, which converted the current flowing through the probe tip to a proportional output voltage. A bias voltage of ± 0.2 V was applied between the sample and the tip. A signal Access Module (Digital Instruments, CA) collected the output voltage and sent it to the computer for processing. Conductivity maps were recorded simultaneously with the topographic images.

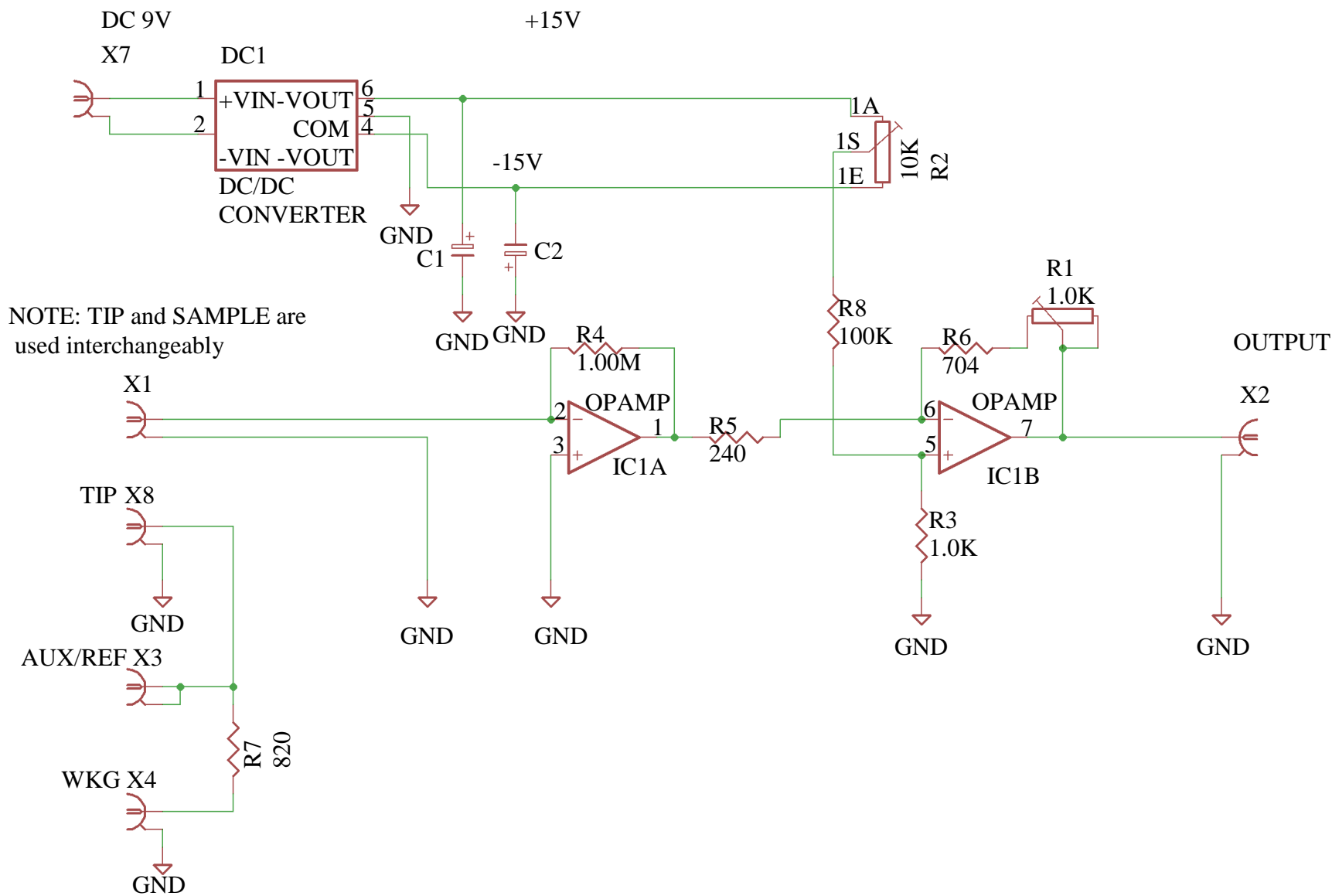


Figure 2.6 Schematic of CP-AFM tip current measurement circuit.

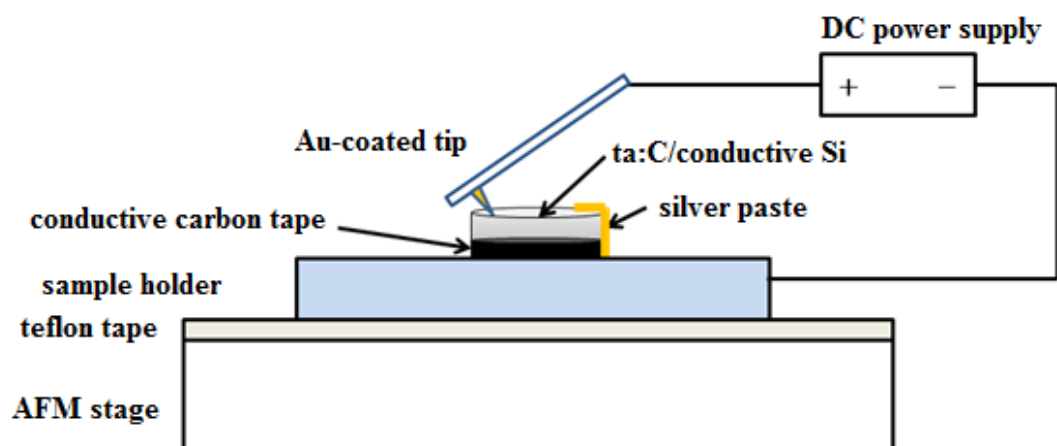


Figure 2.7 Schematic of electrical connection between ta:C films and Au-coated tip in CP-AFM.

2.4.2 Scanning Electrochemical Microscopy (SECM)

SECM measurements⁸²⁻⁸⁴ were made using a commercial microscope (CHI 900, CH Instruments Inc., Austin, TX) in a four-electrode configuration. The electrochemical cell consisted of a Pt wire auxiliary electrode, a 10 μm diameter Pt microelectrode probe tip (CH Instruments Inc. Austin, TX), a homemade Ag/AgCl reference electrode and ta:C films as substrate electrode.

Each time before the measurement, the Pt microelectrode was cleaned by running cyclic voltammograms in 0.1 mol/L HClO_4 from 0 to 1.25 to -0.3 V for 20 cycles. Cycling between the oxygen and hydrogen evolution regimes is a way to clean the Pt surface. To test the surface cleanliness, the cyclic voltammetric response for 1 mM $\text{Fe}(\text{CN})_6^{4-}$ in 1M KCl was measured at scan rate of 25 mV/s. Reversible or near reversible behavior was used as a diagnostic microelectrode preparedness. As a follow up, the microelectrode was sometimes polished to clean and activate the surface. Polishing was done with slurries of alumina of decreasing grit size

(1.0, 0.30 and 0.05 microns) on separate polishing cloth. After each polishing step, the microelectrode was fully rinsed with distilled water. Evidence for cleanliness was also obtained by measurements of the Pt voltammetric features in 0.1 M HClO₄.

2.5 Reagents for electrochemical measurements

All solutions were prepared with ultrapure water from a Barnstead E-Pure system (> 17 MΩ-cm). The potassium ferrocyanide (Sigma-Aldrich), hexamineruthenium (III) chloride (Aldrich), potassium hydroxide (Sigma-Aldrich), methylene blue (Sigma-Aldrich), potassium chloride (Sigma-Aldrich), potassium phosphate monobasic (Spectrum Chemical MFG), potassium phosphate dibasic (Columbus Chemical Industries), sulfuric acid (Columbus Chemical Industries) and hydrochloric acid (Columbus Chemical Industries), Dopamine hydrochloride (Sigma Aldrich), norepinephrine bitartrate (Sigma Aldrich), normetanephrine hydrochloride (Sigma Aldrich), and serotonin hydrochloride (Sigma Aldrich) were used without any purification. Potassium phosphate monobasic (Sigma Aldrich), potassium phosphate dibasic (Sigma Aldrich), and sodium chloride (Columbus Chemical Industries) were used to prepare the carrier solution (0.1M PBS buffer, pH=7.2).

All glassware was cleaned using a three-step procedure: ethanol/KOH bath, alconox/ultrapure water solution, and ultrapure water.

Chapter 3. Electroanalytical Performance of Nitrogen-Containing Tetrahedral amorphous Carbon Thin-Film Electrodes

3.1 Introduction

Glassy carbon is a common used electrode material for electroanalytical measurements. Therefore, it is a useful benchmark for comparison studies of new electrode materials. In this work, we compared the performance of nitrogen-containing tetrahedral amorphous carbon thin-film electrodes. These new electrode materials exhibited low background current, a wide working potential window, low capacitance, relatively rapid electron-transfer kinetics for some common aqueous redox systems and weak molecular adsorption of polar molecules.

In this chapter, the microstructure of the ta:C and N-ta:C films, as deposited by pulsed laser-arc deposition, and the correlation of the film microstructure with these basic electrochemical properties is reported on. We tested the hypothesis that increased nitrogen incorporation would result in a greater fraction of sp^2 -bonded carbon in the films and that this would cause the electrochemical properties of the films to transition from ones more resembling diamond (sp^3 carbon) to ones more resembling glassy carbon (sp^2 carbon). The film chemistry was probed by XPS while the film microstructure was characterized by EELS and Raman spectroscopy. The heterogeneous electron-transfer kinetics for $Ru(NH_3)_6^{+3/+2}$ and $Fe(CN)_6^{-3/-4}$ were studied as was the potential-dependence of the electrode capacitance. The tendency for a redox-active molecule, methylene blue, to adsorb was also investigated as a function of the film microstructure.

3.2 Microstructure Characterization

3.2.1 X-ray Photoelectron Spectroscopy (XPS)

Figure 3.1A shows survey scans for a ta:C film deposited without N₂ and one deposited with 30 sccm N₂ added to the process gas. Clearly, nitrogen is present (N1s ~402eV) in the near surface of only the film deposited in the presence of N₂. Both film surfaces contain carbon (C1s ~284 eV) and oxygen (O1s ~532 eV). Figure 3.1B shows both scans on an expanded scale, specifically enlargement of the C1s and N1s regions. The C1s line position is about 284.8 eV for both films; a slightly higher binding energy than that for carbon in graphite at 284.6 eV. This is consistent with there being some sp³ bonded carbon in the film.⁸⁵ Figure 3.1C shows plots of the O/C and N/C atomic ratios for the different ta:C films deposited with varying amounts of N₂. There is a near linear relationship between the amount of incorporated film nitrogen and the N₂ flow rate. The N/C atomic ratio increased from *ca.* 6% for the film grown with 10 sccm N₂ to *ca.* 13% for the film deposited with 50 sccm N₂. Due to the shallow photoelectron escape depth, the nitrogen signal arises from the atomic content in the near-surface region (~10 nm or so) and not the bulk. We presume, however, that these near-surface levels are reflective of the atomic composition throughout the film bulk as the films are relatively thin (~200 nm thick). All the films, regardless of the nitrogen content, contain a relatively constant O/C atomic ratio of 13-15% in the near-surface region.

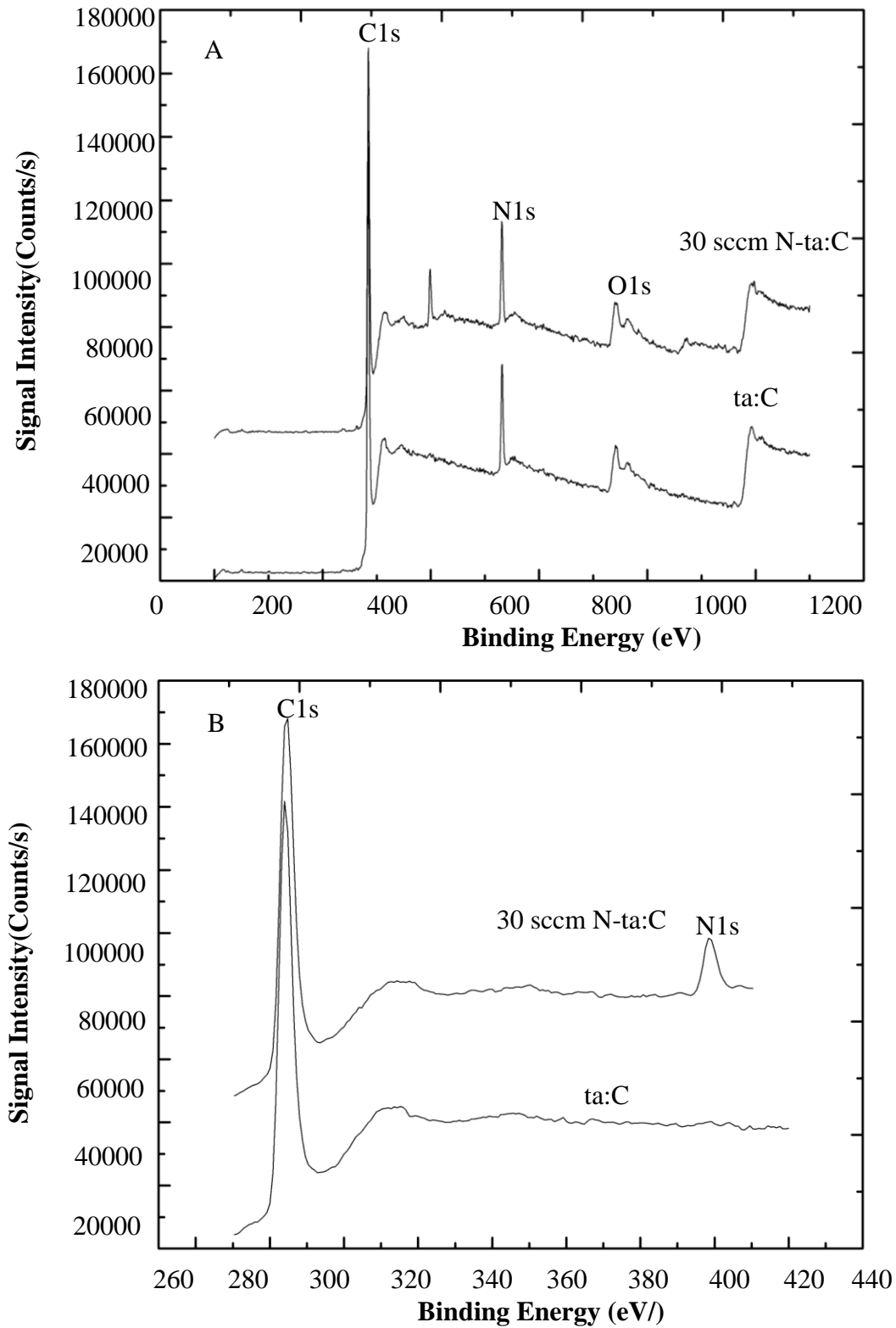
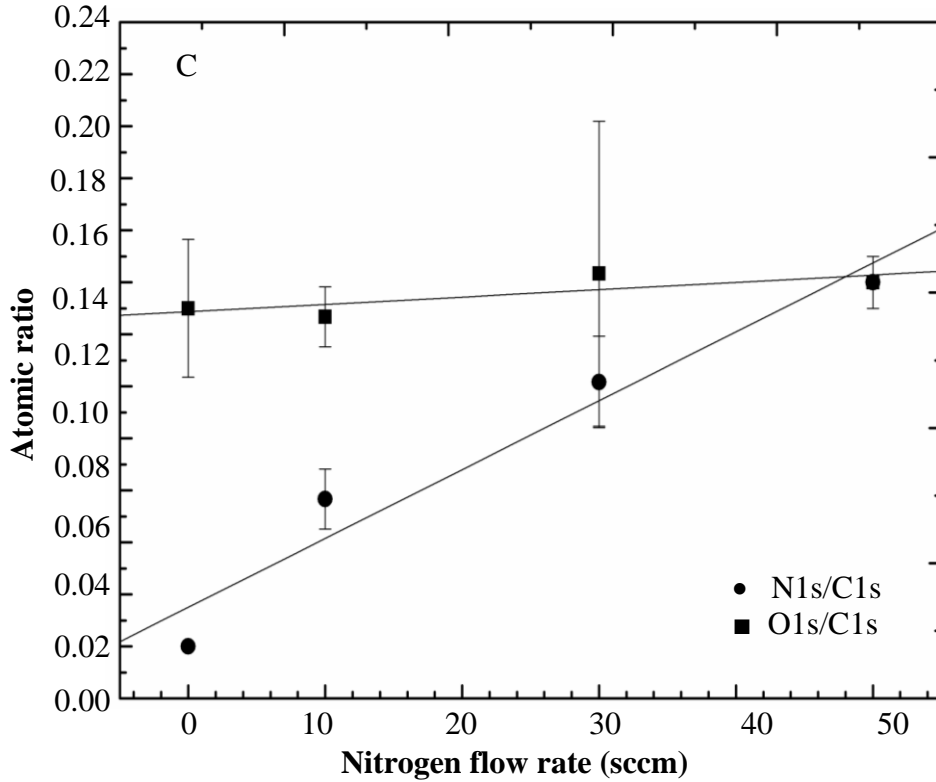


Figure 3.1 (A) XPS survey spectra for a ta:C film and a N-ta:C film deposited with 30 sccm N₂. (B) Expanded XPS survey spectra for C1s and N1s peak from (A). (C) Plot of the O/C and N/C atomic ratio for different ta:C films as a function of the N₂ flow used during the deposition.

Figure 3.1 (cont'd)



3.2.2 Atomic Force Microscopy (AFM)

Figure 3.2 presents height-mode AFM images ($3 \times 3 \mu\text{m}^2$) for the ta:C and N-ta:C films. Based on the image features, all the films are characterized by a nodular morphology. The nodular features increase in size with increasing nitrogen content. This contributes to greater film roughness. Five measurements ($3 \times 3 \mu\text{m}^2$) were made at different locations on each film to determine the roughness. The nominal roughness of each film type was 9 ± 4 (0 sccm N_2), 15 ± 7 (10 sccm N_2), 14 ± 3 (30 sccm N_2) and 23 ± 9 nm (50 sccm N_2). The nodules in our films result from carbon microparticles detached from the solid graphite source during growth. These particles get embedded into the film structure. Their incorporation changes the angle of incidence

of subsequently by altering C ions and this leads to increased sp^2 carbon formation. The sp^2 -bonded carbon has a lower density, which leads to localized volume increases and “bulges” in the film.⁸⁶

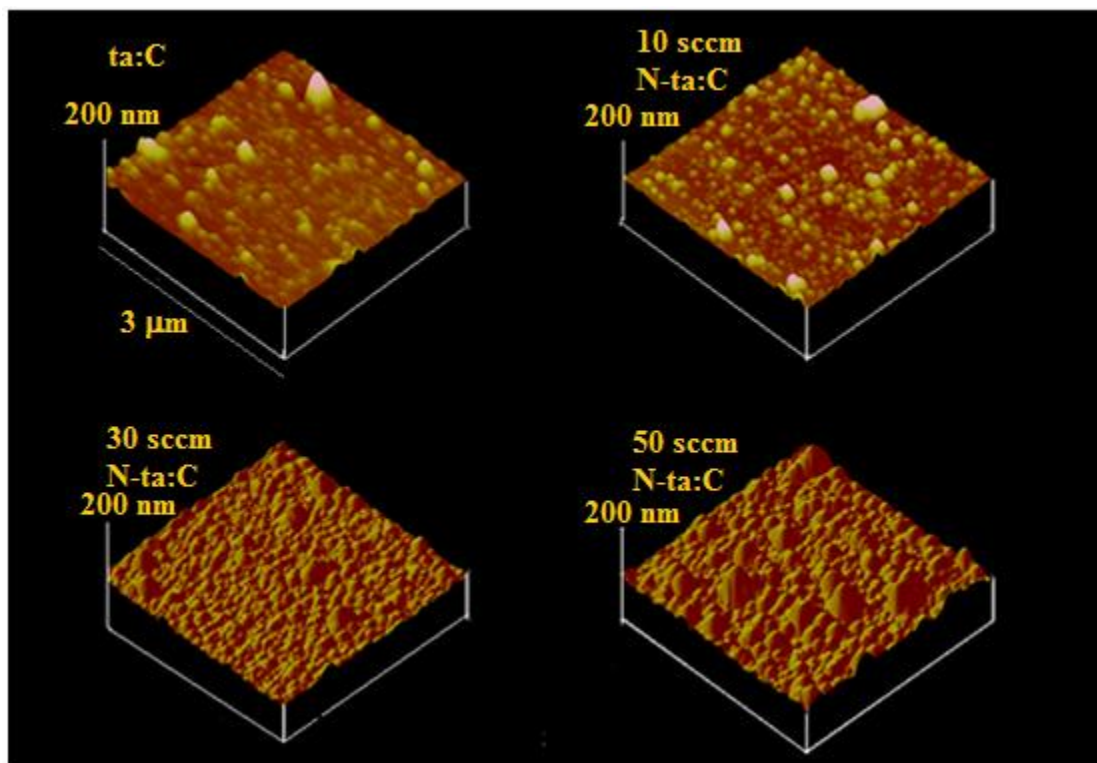


Figure 3.2 Height-mode of AFM images of ta:C and N-ta:C films deposited with 10, 30 and 50 sccm of N₂.

3.2.3 Electron Energy Loss Spectra (EELS)

Small-spot EELS measurements were made to assess the local carbon bonding in ta:C films with different levels of incorporated nitrogen. The carbon K-edge spectra for the ta:C and N-ta:C films are presented in Figure 3.3 A. Figure 3.3 B presents characteristic reference spectra for a pure sp^3 carbon material, diamond, and a pure sp^2 material, multiwall carbon nanotubes (MWCNTs). Unlike the reference spectrum for diamond that consists of a well-defined σ^* absorption edge at 289.5 eV and a second band gap feature at *ca.* 302.0 eV, the spectra for the

ta:C and N-ta:C films all consist of a π^* peak at 285.4 eV that arises from the sp^2 -bonded carbon domains, as well as a broad and more intense sp^3 carbon σ^* absorption edge. The spectrum for each of the ta:C films is characteristic of a mixed-microstructure material (sp^2/sp^3).

The curve area between 280 and 285.4 eV is reflective of the amount of sp^2 -bonded carbon (π) in the probed region while the curve area from 285.4 to 292.4 eV is indicative of the sp^3 -bonded carbon (σ) content.^{20, 42} Therefore, the σ/π area ratio provides an estimate of the sp^3 relative to the sp^2 -bonded carbon content in the films. Spectra were obtained from ten random spots on each film and the area ratios were averaged together to produce the data displayed in Table 3.1. As can be seen, the fraction of sp^2 -bonded carbon increases with increasing nitrogen incorporation. These ta:C and N-ta:C films have an sp^3/sp^3+sp^2 carbon content that ranges from 40-60%, depending on the level of incorporated nitrogen. There is increasing sp^2 carbon bonding with increasing nitrogen incorporation. The nominal σ/π area ratio is 1.3 for the 0 and 10 sccm N_2 films and decreases to 0.97 and 0.72, respectively, for the 30 and 50 sccm N_2 films. This is consistent with the published reports for N-ta:C films.^{42, 87}

% Carbon Bonding	ta:C	10 sccm N_2	30 sccm N_2	50 sccm N_2
sp^2	44 ± 3	44 ± 9	51 ± 8	58 ± 9
sp^3	56 ± 3	56 ± 9	49 ± 8	42 ± 9

Table 3.1. Summary of EELS data for the ta:C and N-ta:C films deposited with 10, 30 and 50 sccm N_2 . Data generated from 10 measurements made randomly on each film.

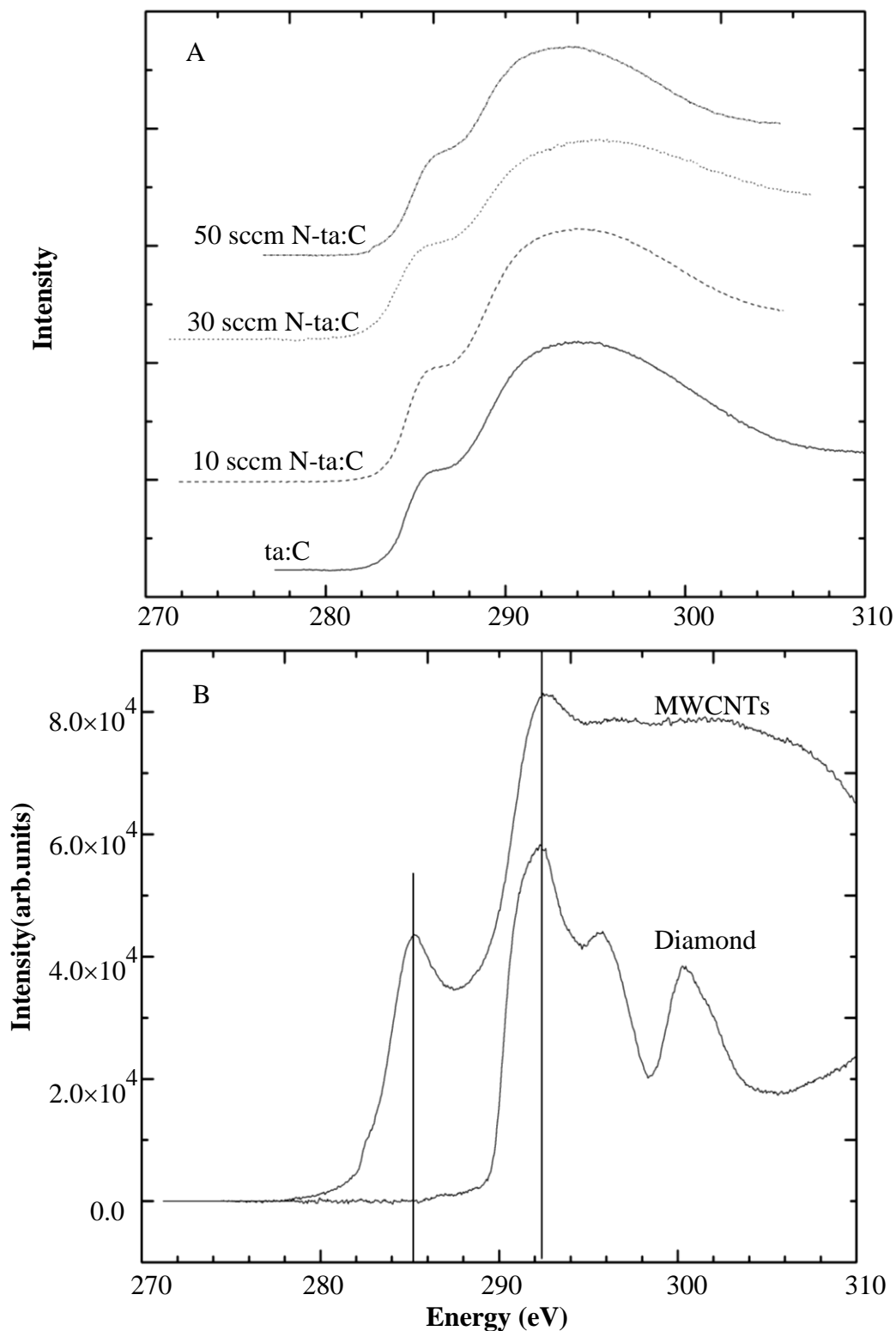


Figure 3.3 (A) Electron energy loss spectra (EELS) at the C K edge for (A) ta:C and N-ta:C films deposited with 10, 30 and 50 sccm N₂. (B) Reference spectra for single crystal diamond (pure sp³) and multiwall carbon nanotubes (pure sp²).

3.2.4 Visible Raman Spectroscopy

Raman spectroscopy was used to assess the microstructure over larger scale (μm) than the EELS measurements. The sp^3 carbon fraction and the configuration of the sp^2 domains in diamond-like carbon films can be deduced from the position of the D ($\sim 1360 \text{ cm}^{-1}$) and G ($\sim 1580 \text{ cm}^{-1}$) bands, the ratio of the peak areas and the peak widths. The ta:C materials typically exhibit a predominant G-band. Figure 3.4 shows the visible (514.5 nm) Raman spectra for ta:C and N-ta:C films between 800 and 2000 cm^{-1} . The spectra are characterized by an asymmetric scattering profile between 1000 and 1700 cm^{-1} , with a maximum at *ca.* 1510 cm^{-1} . Such spectra are typical for ta:C films.³⁵ The peak becomes more asymmetric with increasing nitrogen incorporation as the scattering intensity near 1350 cm^{-1} increases. This trend is indicative of an increasing fraction of sp^2 -bonded carbon. The Raman spectrum for amorphous carbons, like ta:C, is dominated by modes of the graphite-like carbon lattice; the so-called D and G modes.⁵⁵ This domination is because of the sizably larger (230x) scattering cross-section coefficient for the sp^2 -bonded carbon.⁵²⁻⁵³ The G mode for amorphous carbons arises from the bond stretching vibrations of pairs of sp^2 sites, and the D mode is due to the breathing mode of six-fold sp^2 rings.⁸⁸

To estimate the relative sp^2/sp^3 carbon ratio in the films, the spectra were fit with two Gaussian-Lorentzian peaks: the D-mode centered at 1358 cm^{-1} and the G-mode at 1580 cm^{-1} .³⁵

An example of the peak fitting is presented in Figure 3.4 for the 50 sccm N-ta:C film. Table 3.2

presents a summary of the I_D/I_G peak intensity ratio, the G-band position and the peak widths for the different ta:C films. These parameters were determined from the spectral fitting. Robertson et al. reported that the I_D/I_G intensity ratio and the line width of G peak are good indicators of the ta:C film microstructure.³⁴ It can be seen that the I_D/I_G ratio increases with increasing N content. The G-mode width also decreases and the band position shifts to lower wave numbers with increasing N content. Both are the expected trends for increasing sp^2 carbon content and/or domain size. The Raman data, along with the EELS results, confirm that the ta:C films with increasing nitrogen levels have increased levels of sp^2 -bonded carbon.

Sample	I_D/I_G	G-band position (cm^{-1})	FWHM, W_G (cm^{-1})
ta:C	0.64±0.02	1556.6±1.2	172.4±1.6
10 sccm N-ta:C	0.84±0.02	1552.6±0.7	164.4±3.2
30 sccm N-ta:C	0.99±0.09	1548.2±0.9	163.4±2.2
50 sccm N-ta:C	1.12±0.05	1547.0±1.9	158.0±0.6

Table 3.2 Raman spectral parameters for ta:C and N-ta:C films obtained from fitting the spectra with two peaks using Gaussian-Lorentzian functions: D-band at 1358 cm^{-1} and G-band at 1580 cm^{-1} . The N-ta:C films were deposited with 10, 30 and 50 sccm N_2 . (n=4)

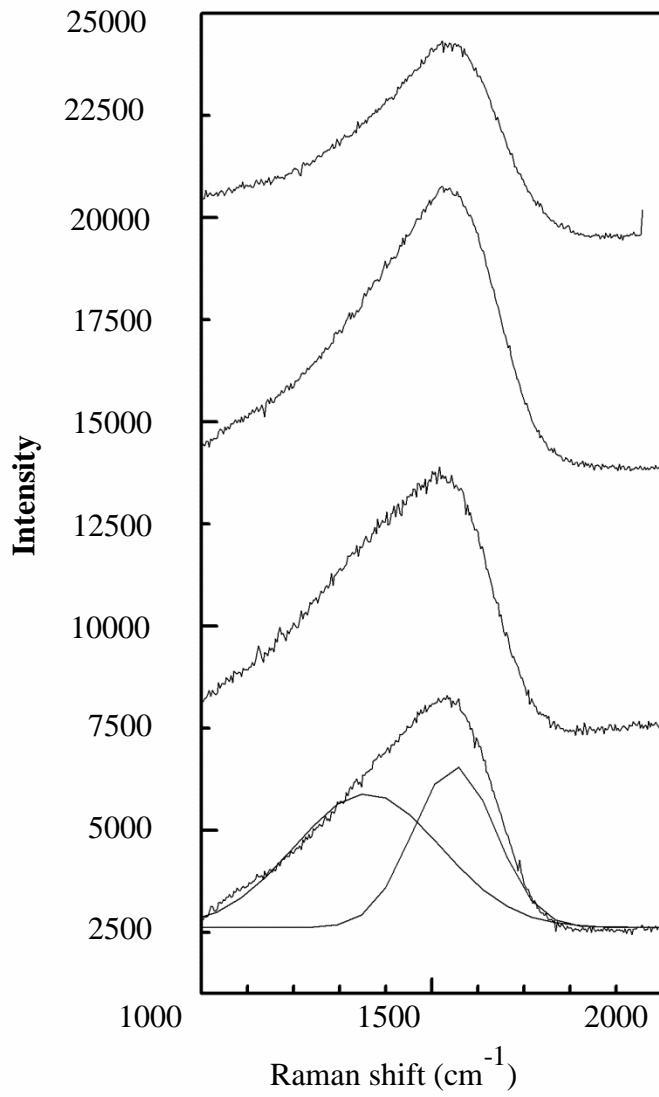


Figure 3.4 Visible Raman Spectra (514.5 nm) for ta:C and N-ta:C films deposited with 10, 30 and 50 sccm N₂.

3.3 Electrochemical Performance

3.3.1 Background Current and Capacitance-Potential Profiles

Figure 3.5 shows background cyclic voltammetric i - E curves for the ta:C and N-ta:C films in 1M KCl. Curves for glassy carbon and boron-doped diamond are also presented for comparison. The geometric area of all the electrodes was 0.2 cm^2 . The curves for all the ta:C films are featureless with current magnitudes slightly higher than the current for the boron-doped diamond film, but lower than the current for glassy carbon. For example, at 0.2 V, the anodic current for diamond is $4.5 \mu\text{A}/\text{cm}^2$. In contrast, the current for glassy carbon is 5x larger at $23.1 \mu\text{A}/\text{cm}^2$. For all the ta:C and N-ta:C films, the background current at this potential is approximately $12 \mu\text{A}/\text{cm}^2$. The lower background current for the ta:C and N-ta:C films is an attractive feature for electroanalytical measurements in terms of enhanced S/B ratios.

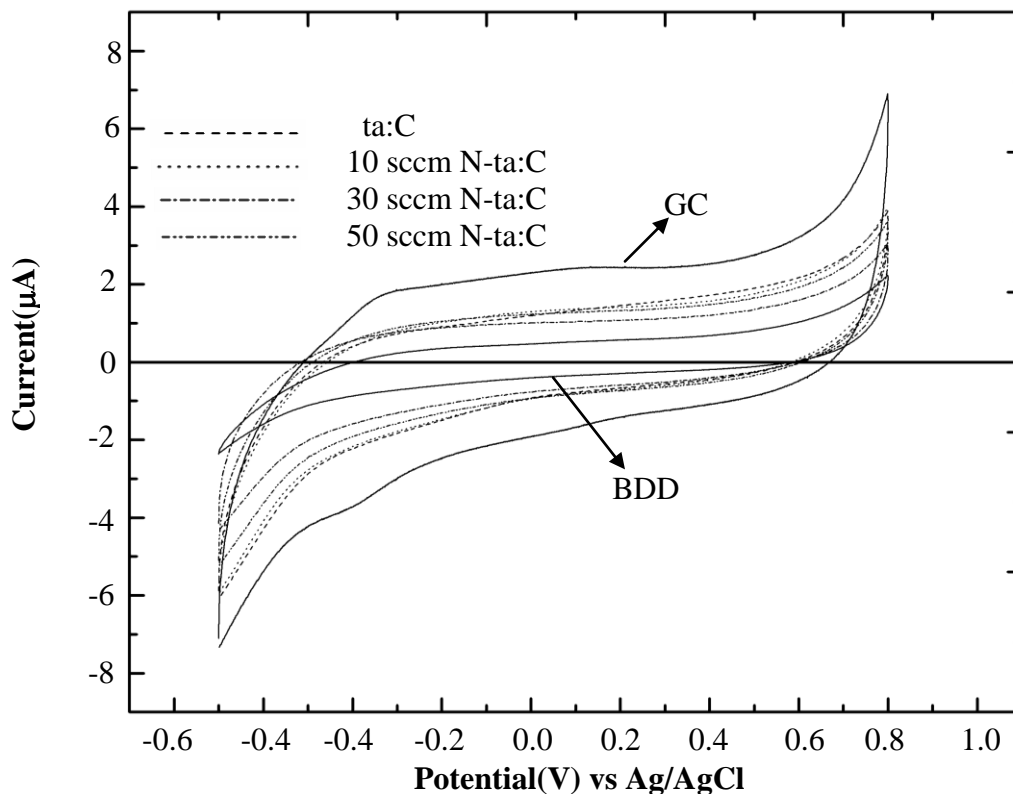


Figure 3.5 Cyclic voltammetric $i-E$ curves for ta:C, N-ta:C films grown with 10, 30 and 50 sccm N_2 , glassy carbon and a boron-doped diamond thin film, all in 1M KCl. Scan rate = 0.1 V/s. Geometric area = 0.2 cm^2 .

Figure 3.6 shows capacitance-potential ($C_{dl}-E$) profiles for each of the ta:C and N-ta:C films recorded in 1M KCl. Comparison data are presented for glassy carbon and boron-doped diamond. The capacitance for glassy carbon ranges from 35-50 $\mu\text{F}/\text{cm}^2$ over the potential range probed. This capacitance is higher than previously reported data by our group for polished glassy carbon.⁸⁹ We attribute the higher capacitance to surface roughness remaining after the polishing step. In other words, these glassy carbon electrodes were no as smooth as the electrode used in the prior work. In contrast, the capacitance for boron-doped diamond ranges from 5-11 $\mu\text{F}/\text{cm}^2$,

consistent with our previously reported results.⁸⁹ The capacitance of the ta:C films falls in between these two electrode materials with values of 20-30 $\mu\text{F}/\text{cm}^2$. This suggests that the electronic properties of these ta:C electrodes lie intermediate between those of a semimetal, like diamond, and a conductor, like glassy carbon.

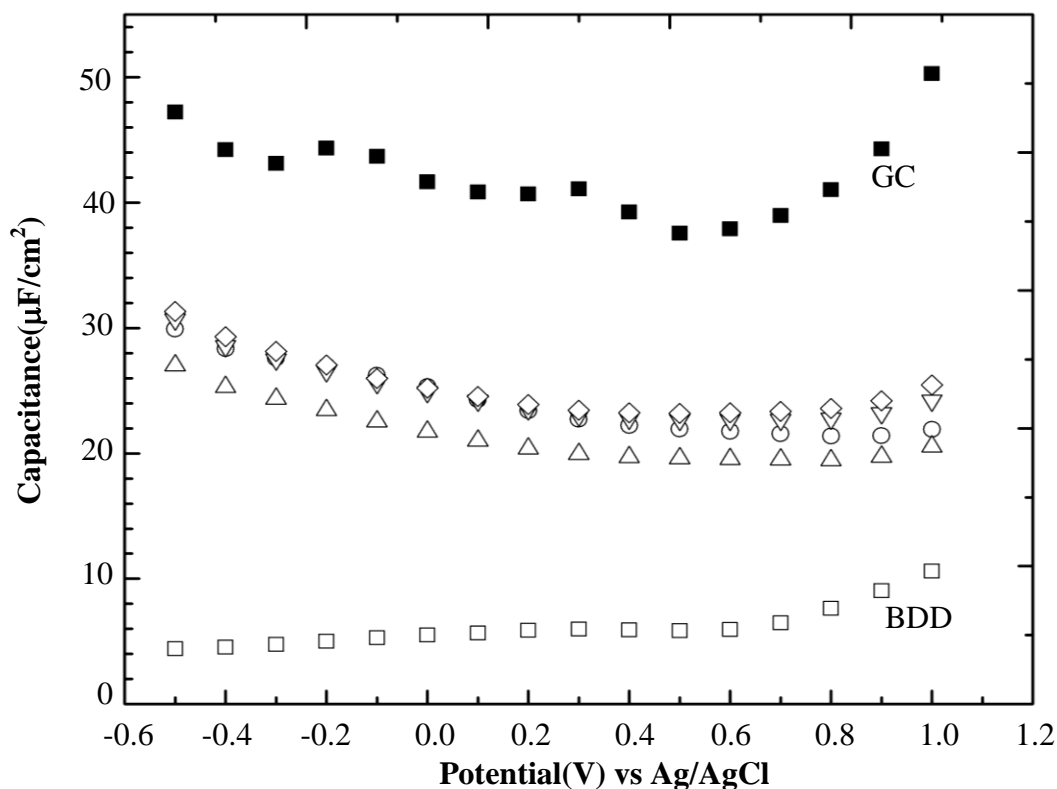


Figure 3.6 Capacitance-potential profiles for ta:C (○), 10 sccmN-ta:C(△), 30 sccmN-ta:C (▽), and 50 sccmN-ta:C (◇) films in 0.1 M HClO₄. Comparison data for glassy carbon and boron-doped diamond are presented. Capacitance values were determined using a 10 mV sine wave at 40 Hz. $Z_{im} = 1/2\pi fC_{dl}$. Data are normalized to the geometric area, 0.2 cm².

3.3.2 Electrochemical Activities in Outer-sphere and Inner-sphere Redox Couples

Figures 3.7 and 3.8 show cyclic voltammetric *i*-*E* curves for the ta:C and N-ta:C films in the presence of 1mM Ru(NH₃)₆^{2+/3+} and 1mM Fe(CN)₆^{3-/4-}, respectively, both in 1 M KCl.

Table 3.3 provides a statistical summary of the cyclic voltammetric data for all four electrodes and presents apparent heterogeneous electron-transfer rate constants, k_{app}^0 . $\text{Ru}(\text{NH}_3)_6^{2+/3+}$ is classified as outer-sphere redox couple and generally involves simple electron transfer at carbon electrodes. k^0 for this redox couple is relatively insensitive to the surface microstructure, surface oxides and the adsorbed monolayers on sp^2 carbon electrodes.^{1, 7, 90} The heterogeneous electron-transfer rate constant is mainly controlled by the electronic properties of the electrode (*i.e.*, carrier mobility and carrier concentration). Well-defined, peak-shaped curves are seen for all the films. Essentially reversible (Nernstian) behavior is seen as the peak separation potential, ΔE_p , is 59 mV for all four films. Plots of i_p^{red} vs. $v^{1/2}$ were linear for all four films between 0.1 and 0.7 V/s ($R^2 > 0.99$), which indicates the current (rate of reaction) is controlled by semi-infinite linear diffusion of the analyte to the electrode surface. The i_p^{ox}/i_p^{red} ratios were near unity for all four electrodes confirming the chemical reversibility of the redox reaction. Near-Nernstian behavior was observed for this redox system at all the ta:C films at the scan rates employed. Therefore, we were unable to extract k_{app}^0 values from the data as the system was behaving reversibly.

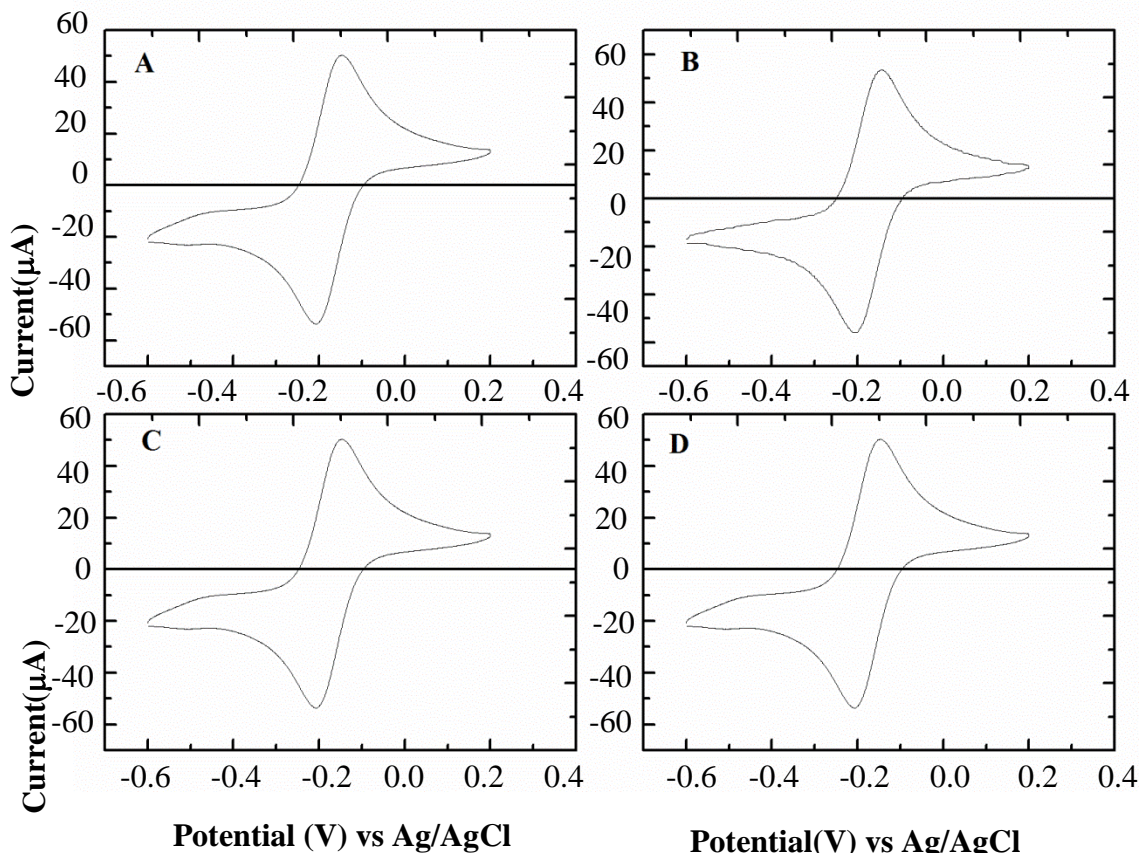


Figure 3.7 Cyclic voltammetric i - E curves with iR correction for ta:C (A), 10 sccm N-ta:C (B), 30 sccm N-ta:C (D), 50 sccm N-ta:C (E) in 1 mM $\text{Ru}(\text{NH}_3)_6^{2+/3+}$ in 1 M KCl. Scan rate = 0.1 V/s. Geometric area = 0.2 cm^2 .

$\text{Fe}(\text{CN})_6^{3-/4-}$, on the other hand, is an inner-sphere redox couple with a k^o value that is strongly influenced by several variables: (1) the electronic properties of the electrode (density of electronic states near E^o) (2) surface cleanness and (3) surface chemistry (*e.g.*, carbon-oxygen functional groups).¹¹⁻¹³ As seen in Table 3.3, the ΔE_p values decrease with increasing N content. Well-defined, peak-shaped curves are seen for all four films. The i_p^{ox} vs. $v^{1/2}$ plots were linear for all four films between 0.1 and 0.7 V/s ($R^2 > 0.99$). The i_p^{ox}/i_p^{red} ratios were unity. The k_{app}^o value increases with nitrogen content ranging from $0.0047 \pm 0.001 \text{ cm/s}$ for the ta:C film to $0.015 \pm 0.009 \text{ cm/s}$ for the 50 sccm N-ta:C film.

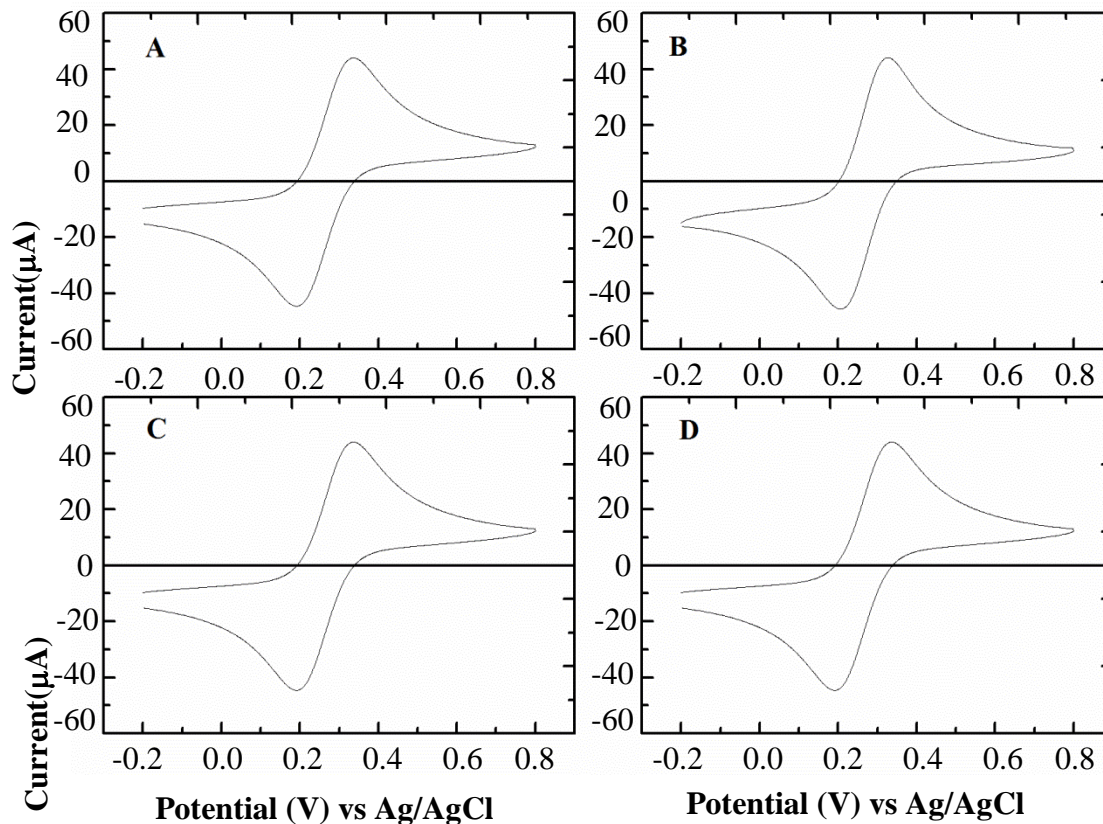


Figure 3.8 Cyclic voltammetric i - E curves with iR correction for ta:C (A), 10 sccm N-ta:C (B), 30 sccm N-ta:C (D), 50 sccm N-ta:C (E) in 1 mM $\text{Fe}(\text{CN})_6^{3-/4-}$ in 1 M KCl. Scan rate = 0.1 V/s. Geometric area = 0.2 cm^2 .

	N-ta:C	N-ta:C	ta:C N-ta:C	10 sccm	30 sccm	50 sccm
$\text{Ru}(\text{NH}_3)_6^{2+/3+}$ ΔE_p (mV)			58 ± 1	59 ± 3	61 ± 3	59 ± 5
i_p^{red} (μA)		55 ± 2	60 ± 3	58 ± 1	58 ± 1	
$\text{Fe}(\text{CN})_6^{3-/4-}$ ΔE_p (mV)			119 ± 18	109 ± 17	97 ± 6	84 ± 15
i_p^{ox} (μA)		49 ± 4	52 ± 4	54 ± 2	53 ± 7	
k^0 (cm/s)	0.0047 ± 0.001	0.0063 ± 0.002	0.0079 ± 0.001	0.015 ± 0.009		
α	0.5	0.5	0.5	0.5	0.5	

Table 3.3 Summary of iR -corrected cyclic voltammetric data for $\text{Ru}(\text{NH}_3)_6^{+3/+2}$ and $\text{Fe}(\text{CN})_6^{-3/-4}$ at ta:C and N-ta:C thin films deposited with 10, 30 and 50 sccm N_2 . Scan rate = 0.1 V/s. Geometric area = 0.2 cm^2 . (n=5)

3.3.3 Electrochemical Behavior of Methylene Blue

Methylene blue is an electroactive molecule that strongly adsorbs on glassy carbon electrode surfaces.⁶⁻⁷ The surface coverage of methylene blue on GC is 190 pmol/cm^2 . We therefore selected this molecule as a probe for molecular adsorption on the ta:C films. The cyclic voltmmetric *i-E* curves in $10 \text{ }\mu\text{M}$ methylene blue are shown in Figure 3.9 for (A) glassy carbon and (B) a 30 sccm N-ta:C film. The solid line represents the background current in $0.1\text{M H}_2\text{SO}_4$. The “in solution” cyclic voltmmetric *i-E* curves were obtained in the presence of $10 \text{ }\mu\text{M}$ methylene blue. The “after soaking” curves were obtained after cycling the electrode in the presence of methylene blue for multiple minutes, removing the solution and rinsing the electrode, and replacing the solution with $0.1 \text{ M H}_2\text{SO}_4$. The inserted figures are the background-corrected cyclic voltammograms for methylene blue dissolved in solution.

The cyclic voltammogram for glassy carbon shows characteristic features of methylene blue adsorption.⁷ A pair of narrow symmetric peaks is seen with a ΔE_p of 16 mV . This is close to the theoretical value of $\Delta E_p=0$ expected for adsorbed molecule undergoing fast electron transfer. The theoretical diffusion-limited peak current for the methylene blue was calculated to be $0.15 \text{ }\mu\text{A}$ for this solution concentration ($n = 2$, $A = 0.2 \text{ cm}^2$, $v = 0.025 \text{ V/s}$, and $D = 3 \times 10^{-6} \text{ cm}^2/\text{s}$). The oxidation peak current, i_p^{ox} , measured from the voltammogram (Fig. 3.9 A) is $7.1 \text{ }\mu\text{A}$ or $\sim 47\text{x}$ larger than the theoretical value. This is also consistent with adsorbed methylene blue. Additionally, the peak currents increased proportionally with the scan rate (0.025 to 0.1 V/s , $R^2 > 0.98$), consistent with adsorbed redox molecule. The surface coverage calculated from the

anodic peak charge was 335 pmol/cm^2 . Solution immersion testing was also performed. After immersing the glassy carbon surface in the $10 \text{ }\mu\text{M}$ methylene blue solution, rinsing the surface and replacing the solution with fresh $0.1 \text{ M H}_2\text{SO}_4$, a cyclic voltammetric curve nearly identical to that in Figure 3.9 A was obtained. Integration of the anodic peak charge lead to a calculated coverage of 399 pmol/cm^2 .

In contrast, for the 30 sccm N-ta:C film, no evidence for molecular adsorption was detected. Immersion tests revealed the absence of adsorption as the cyclic voltammetric i - E curves in $0.1\text{M H}_2\text{SO}_4$ after methylene blue exposure was devoid of any redox peaks. The oxidation peak current, i_p^{ox} , in Figure 3.9 B is $0.14 \text{ }\mu\text{A}$, which is very close to the theoretical value of $0.15 \text{ }\mu\text{A}$ for a diffusion controlled process. The i_p^{ox} values increased linearly with $v^{1/2}$ ($R^2 > 0.99$) consistent with a diffusion controlled redox reaction. Three different 30-sccm N-ta:C films were tested with identical results for all.

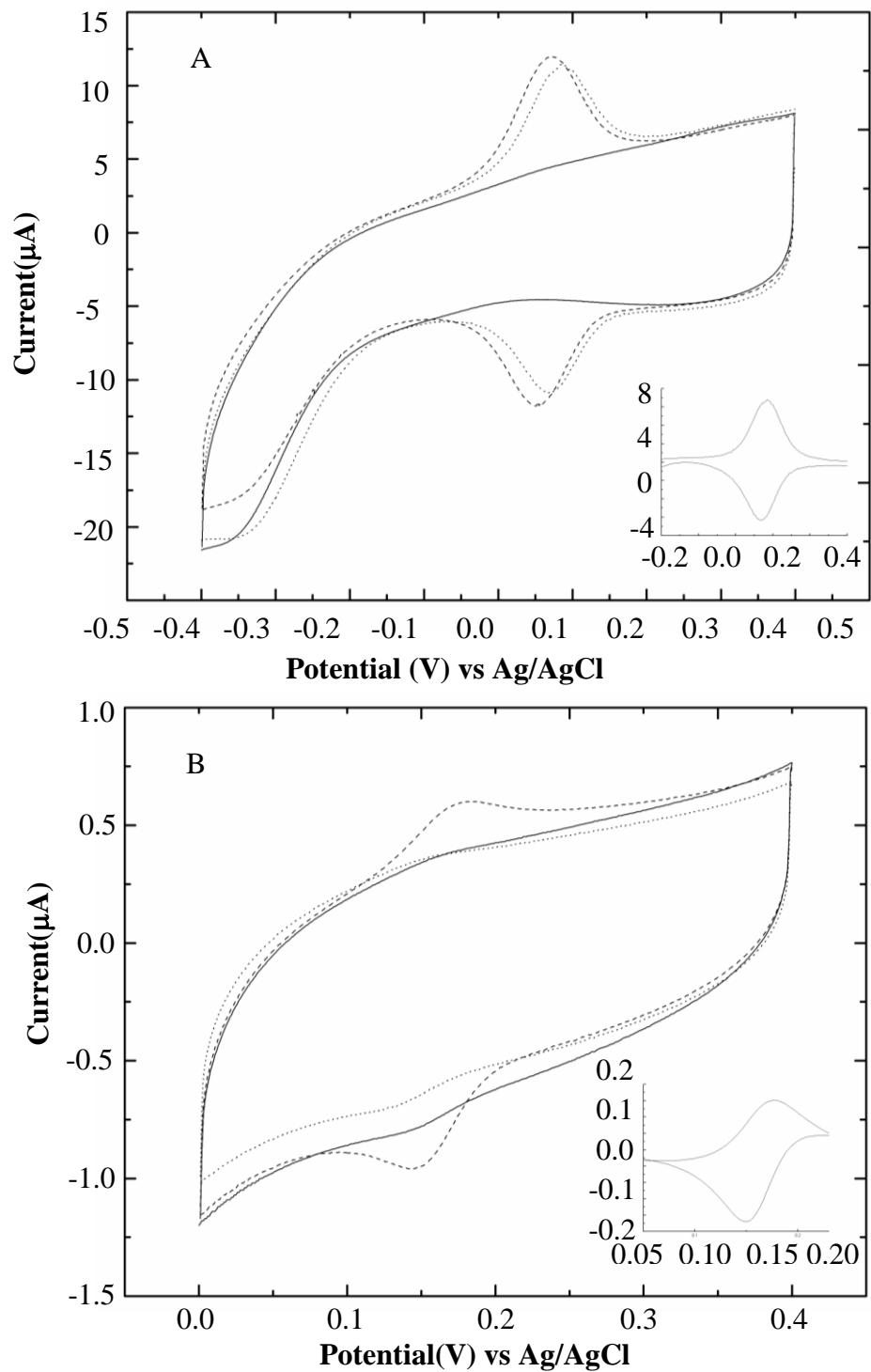


Figure 3.9 Cyclic voltammetric *i-E* curves for (A) GC and (B) a 30-sccm N-ta:C film (B), in 0.1 M H₂SO₄ (—), in 10 μM methylene blue solution (---) and after soaking(...). Scan rate = 0.025 V/s, Geometric area = 0.2 cm². The inserted were cyclic voltammetric *i-E* curves in 10 μM methylene blue after background subtraction.

3.4 Microstructural Stability

3.4.1 Effect of Anodic Polarization

Figure 3.10 A shows cyclic voltammetric i - E curves for a ta:C film in 0.5 M H₂SO₄ before (solid line) and after the film was anodically polarized (dotted line). The purpose for this measurement was to determine how stable the ta:C microstructure is during a typical anodic polarization pretreatment that might be used to activate glassy carbon. One of the characteristics of diamond is its superb micro structural stability during exposure to aggressive electrochemical conditions.¹³ The polarization was carried out potentiostatically at 2 V vs. Ag/AgCl for 15 min in 0.5 M H₂SO₄ (25 °C). Comparison curves for freshly polished glassy carbon, before and after an identical polarization, are presented in Figure 3.10B. The curve for the ta:C film prior to polarization is featureless within the working potential window (~3 V). The background current is low and relatively constant with potential. Similar curve shapes were observed for the other N-ta:C films prior to anodic polarization (data not shown). The working potential window (defined as $\pm 300 \mu\text{A}$) for the ta:C film is 3.1 V, which is lower than the value for boron-doped diamond in this same electrolyte solution (~3.5 V), but larger than the value for glassy carbon (~2.7). The nominal potential windows for the ta:C and N-ta:C films (10, 30 and 50 sccm N₂) were 3.13 ± 0.09 , 3.07 ± 0.05 , 2.89 ± 0.05 and 2.78 ± 0.08 , respectively. Clearly, the potential window decreases with increasing nitrogen content and this correlates with increasing sp² carbon content in the films. The comparison voltammetric behavior of glassy carbon is distinct. The background current (same geometric area) within the working potential window is 3-6x greater than the ta:C films.

The anodic polarization changes the voltammetric behavior of glassy carbon considerably while imparting virtually no change to the response of the ta:C and N-ta:C films. For the ta:C and N-ta:C films, the working potential window and the background current within the window were unaffected by the anodic polarization. In contrast, a significant increase in the background current and a reduction in the working potential window were observed for glassy carbon. These trends are caused by the microstructural damage (exposure of clean edge plane sites) and surface oxidation caused by the polarization. Well defined redox peaks develop at 0.2 V for glassy carbon. These peaks are associated with electroactive surface-carbon oxygen functionalities (*i.e.*, quinone/hydroquinone couple) and these groups represent some fraction of the total oxides produced by the polarization.¹ For glassy carbon, the total anodic charge passed during the polarization was largest at $2.1 \pm 0.4 \text{ C/cm}^2$. In comparison, the charge passed for the ta:C and N-ta:C film deposited with 10 sccm N₂ was identical: $0.13 \pm 0.1 \text{ C/cm}^2$ for the former and for the latter. The 10x lower charge, as compared to glassy carbon, results because of the resistance of ta:C films to microstructural damage and surface oxidation as well as the wider potential window such that there is less contributed charge from water electrolysis. Interestingly though, the charge passed for the N-ta:C film deposited with 30 sccm N₂ was $0.43 \pm 0.08 \text{ C/cm}^2$, about 3-4x greater than the ta:C film. The charge passed during polarization of the N-ta:C film deposited with 50 sccm N₂ was even greater at $2.0 \pm 0.01 \text{ C/cm}^2$; nearly identical to that passed for glassy carbon. Even though the total charge passed for this film was close to that for glass carbon, the working potential window and the background current for the 50-sccm N-ta:C film were still largely unaltered.

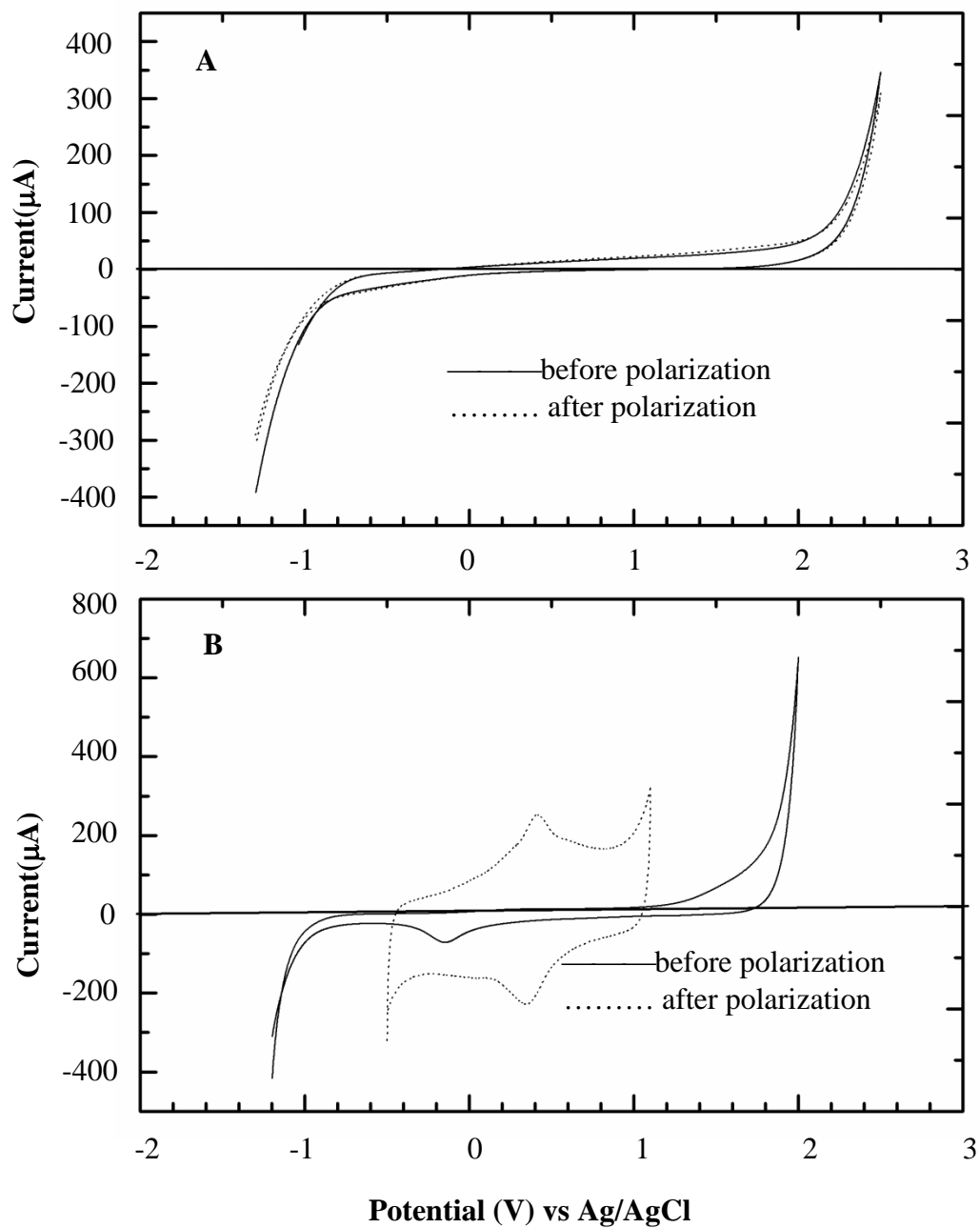


Figure 3.10 Cyclic voltammetric i - E curves for (A) a ta:C film and (B) GC in 0.5 M H_2SO_4 before polarization and after polarization. Scan rate = 50 mV/s. Electrode area = 0.2 cm^2 .

3.4.2 Effect of Chemical Oxidation

The stability and performance of the ta:C and N-ta:C films were also evaluated during strong chemical oxidation. This oxidation treatment is often used to clean diamond surfaces without causing any microstructural alteration. The chemical oxidation involved two steps: (i) 20 min in 3:1 (v/v) HNO₃:HCl at ~55 °C and (ii) 20 min in a 30% H₂O₂ solution at ~55 °C. In the case of the ta:C or the N-ta:C films grown with 10 and 30 sccm of N₂, the oxidation did not alter the microstructure or affect the basic electrochemical properties. However, the 50 sccm ta:C film was completely destroyed by the oxidation as the film cracked and delaminated from the Si substrate.

For the intact films, the voltammetric background current in 1 M KCl increased only by a factor of 1.0-1.5x after the chemical oxidation. The background anodic current at 0.2 V for all the films increased linearly with the scan rate from 0.1 to 0.5 V/s ($R^2 > 0.99$), as expected for capacitive current. From the slope of the i_{bk} vs. v plots, the capacitance, C_{dl} , was determined to be 58, 42 and 56 $\mu\text{F}/\text{cm}^2$, respectively, for the ta:C, 10 sccm N-ta:C and 30 sccm N-ta:C films. The apparent capacitance increase after oxidation (see Fig. 3.6) is likely due to surface oxidation that increases the surface wettability and causes some surface roughening. We did not interrogate these films by AFM or SEM to verify the surface roughening. In summary, with the exception of the 50 sccm N-ta:C film (*i.e.*, the greatest sp^2 carbon content), the morphology and microstructure of the ta:C and N-ta:C films are restable, like boron-doped diamond, during exposure to this aggressive chemical oxidation.

With the exception of the 50 sccm N-ta:C film, the electrochemical response of the films toward $\text{Ru}(\text{NH}_3)_6^{+3/+2}$ was largely unchanged after the chemical oxidation. After oxidation, ΔE_p for $\text{Ru}(\text{NH}_3)_6^{+3/+2}$ increased only from 59 to 65 mV (near Nernstian) up to 0.5 V/s. The i_p^{red} vs. $\nu^{1/2}$ plots remained linear. The effect of oxidation on the $\text{Fe}(\text{CN})_6^{-3/-4}$ response was distinctly different. ΔE_p values increased for all three films after oxidation, compared to those values presented in Table 3.3, consistent with more sluggish electron-transfer kinetics. For the ta:C film, ΔE_p increased from 167 to 314 mV between 0.1 to 0.5 V/s, from 91 to 145 mV for the 10 sccm N-ta:C film, and from 91-120 mV for the 30 sccm N-ta:C film. For all three, i_p^{ox} vs. $\nu^{1/2}$ plots remained linear.

3.5 Discussion and Conclusions

The results confirmed that the ta:C and the low nitrogen (10 and 30 sccm N_2) N-ta:C films exhibit electrochemical properties more closely aligned with those of boron-doped diamond than with those of glassy carbon. In contrast, the film with the highest nitrogen content (50 sccm N_2) exhibited behavior more like that of glassy carbon.

Structurally, it was found that the ta:C and N-ta:C films possess a mixed sp^3 and sp^2 -bonded carbon microstructure. The $\text{sp}^3/\text{sp}^3+\text{sp}^2$ content varied from 40-60%, with the ratio decreasing with increasing incorporated nitrogen. It is unclear if the sp^2 -bonded carbon exists as 6-membered rings, linear or branched chains of unsaturated hydrocarbons, or some combination of the two. Both the EELS and Raman spectroscopic data confirmed the existence of sp^2 carbon

domains in the films. The near-surface N/C atomic ratio, as determined by XPS, increased in a near linear fashion with the process gas N₂ flow from 0 (undetectable nitrogen) for the ta:C film to 14% for the 50 sccm N-ta:C film. Oxygen was present on all the film surfaces at a constant level of *ca.* 14% (O/C). Given how thin these films are (~200 nm), we suppose that the near-surface elemental composition is reflective of the bulk composition. With increasing nitrogen content, the fraction of sp² carbon in the film increased. The incorporated nitrogen forms sp² hybridized bonds with carbon (C=N), and this leads to an overall increase in the sp² carbon content. The film roughness also increased with the nitrogen content. We do not know from our data exactly how the nitrogen is bonded within the films. Future FTIR studies will hopefully provide greater insight as to the C-N bonding in the films.

The electrochemical data indicated the ta:C and low nitrogen N-ta:C thin-film electrodes have properties more similar to those of boron-doped diamond than to those of glassy carbon. Background cyclic voltammetric currents were lower than those for glassy carbon by a factor of 2-5x but slightly higher than those for diamond. The background currents increased slightly with increasing nitrogen content, consistent with increasing sp² carbon content. The capacitance values for the ta:C and N-ta:C films were intermediate between those of diamond and glassy carbon. Capacitance values for all the ta:C films ranged from 20-30 μF/cm² in 0.1 M HClO₄ between -0.5 and 1.0 V vs. Ag/AgCl. There was not a major difference in the values for the different films, regardless of the nitrogen (*i.e.*, sp² carbon) content. This suggests that the electronic properties are not significantly altered by the change in sp² bonding within the films. The lower capacitance and background voltammetric current of the ta:C films make this electrode material attractive for electroanalytical measurements in terms of increased signal-to-background ratios. We are presently investigating the use of these materials in flow injection

analysis coupled with electrochemical detection in order to determine what analytical detection figures of merit are possible.

The working potential window for the ta:C films in 0.5 M H₂SO₄ ranged from 3.1 V for the film deposited with no added N₂ to 2.8 V for the N-ta:C film deposited with 50 sccm N₂. By way of comparison, the potential window for glassy carbon in the same medium is 2.7 V. As is the case for microcrystalline and ultrananocrystalline diamond, the background current increases and the working potential window decreases with increasing sp² carbon content.⁹¹⁻⁹² The 2.8 V limit for the 50 sccm N-ta:C film is similar to the 2.7 V limit for glassy carbon. The sp²-bonded graphitic carbons, with a high fraction of exposed edge plane, are more kinetically active for solvent breakdown (oxygen evolution and hydrogen evolution from water) than is diamond. Therefore, increasing the sp² carbon content in these a ta:C films causes a proportional decrease in the working potential window and an increase in the voltammetric background current.

The ta:C and N-ta:C films exhibit very active voltammetric responses for the outer sphere, Ru(NH₃)₆^{+3/+2}, and the inner sphere, Fe(CN)₆^{-3/-4}. The reproducibility of the voltammetric responses from film to film was also very good. The cyclic voltammetric response for Ru(NH₃)₆^{+3/+2} was near Nernstian for all the films with ΔE_p values of ca. 59 mV at scan rates from 0.1 to 0.5 V/s. There was no increase in ΔE_p with increasing analyte concentration in solution (same scan rate) indicating that ohmic resistance within the films was not influencing the *i*-*E* curve shapes. The apparent heterogeneous electron-transfer rate constant for this redox system at all the films was greater than 0.1 cm/s, which is comparable to what has been reported for boron-doped microcrystalline and ultrananocrystalline diamond thin films.⁹²⁻⁹³ In other

words, the activity of the ta:C and N-ta:C films for this redox system is independent of the sp^2 carbon content, similar to what has been observed for boron-doped diamond.⁹¹

In contrast, quasireversible electron-transfer kinetics were seen for $Fe(CN)_6^{-3/-4}$ at all the films. ΔE_p values decreased with increasing nitrogen content (*i.e.*, increasing sp^2 carbon content) ranging from a nominal value of 119 mV for the ta:C film to 84 mV for the 50 sccm N-ta:C film. Clearly, the sp^2 -bonded carbon introduces more active sites for this redox system, and the trend is not a reduction in the ohmic resistance of the film based on the $Ru(NH_3)_6^{+3/+2}$ data. The trend seen for the ta:C films is similar to that seen for boron-doped diamond electrodes with increasing levels of sp^2 carbon impurity. These two distinct redox analyte behaviors is why the electrochemical activity of these new carbon electrodes must be evaluated using a variety of redox systems. The reason for the $Fe(CN)_6^{-3/-4}$ activity increase with increasing sp^2 carbon content is unclear at this time but maybe related to differences in the double layer structure (potential at the plane of closest approach) at the sp^3 versus the sp^2 carbon sites, which have a greater impact on the inner-sphere $Fe(CN)_6^{-3/-4}$ redox couple. The apparent heterogeneous electron-transfer rate constants ranged from 0.0046 to 0.024 cm/s, which are comparable to those found for diamond.⁹³

The undetectable methylene blue adsorption on the ta:C and N-ta:C films is certainly a distinguishing feature and very much resembles the characteristics of boron-doped diamond. The strong molecular adsorption on glassy carbon is likely driven by a combination of H-bonding, dipole-dipole and π - π interactions at the electrode surface. While the 30-sccm N-ta:C film has

surface carbon-oxygen functional groups, the types of functional groups and the functional group density are likely different from glassy carbon. For example, there is no evidence for any redox-active quinone functional groups on the ta:C films like there are on oxidized glassy carbon (see peaks in Fig. 3.10B). Also, the N-ta:C films possess no extended π -electron system. Taken together, these differences are likely the reason for the weak molecular adsorption of methylene blue on the ta:C electrodes.

With the exception of the glassy carbon-like 50 sccm N-ta:C film, the other ta:C and N-ta:C films exhibited excellent microstructural stability during anodic polarization and harsh chemical oxidation, much like boron-doped diamond. These are trademark characteristics of diamond that are mimicked for the most part by these ta:C films. The surface also does not undergo extensive surface oxide formation, at least ionizable and or electrochemically active oxides, during either of these two treatments as evidenced by the fact that the background voltammetric current and working potential window are both relatively unchanged after treatment. The N-ta:C film deposited with 50 sccm N_2 behaved more like a graphitic carbon being completely destroyed during exposure to two-step oxidation treatment. The greater sp^2 carbon content of this film rendered it more susceptible to microstructural degradation, likely due to the corrosion (gasification) of this carbon preferentially over the sp^3 carbon.

The ta:C and N-ta:C films show some similarity with nano-carbon films from Niwa's group, which have sp^3/sp^2+sp^3 about 0.70.⁹⁴⁻⁹⁶ The electron cyclotron resonance (ECR)-sputtered carbon films have wide working potential (3.7 V in 0.05 M H_2SO_4), fast electron-transfer rates in $Ru(NH_3)_6^{+3/+2}$ and $Fe(CN)_6^{-3/-4}$ which are close to those of GC. Due to their

ultraflat surface (0.7 Å roughness) and low surface O/C (3.3%), these nano-carbon films have weak interactions with electroactive species (e.g. Fe^{+2/+3}, O₂ reduction). The resistance to fouling and high stability of these nano-carbon films to detect biomolecules (e.g. bisphenol A) is great advantage to be applied in eletroanalytical area. They successfully developed a simple electrochemical DNA methylation analysis technique with this nano-carbon film.⁹⁷ The ta:C and N-ta:C films reported on herein are predicted to have similar behavior as nano-carbon films in terms of biomolecule detection.

Chapter 4. Factors Affecting the Microscopic Electrical and Electrochemical Properties of Nitrogen-Containing Tetrahedral Amorphous Carbon Thin-Film Electrodes

4.1 Heterogeneous Electrical Conductivity of N-ta:C films

4.1.1 Introduction

In field emission, people have been interested in carbon materials, such as diamond, diamond-like carbon (DLC) and nanostructured carbon, for a long time due to their low applied field for the electron emission.⁹⁸⁻⁹⁹ On the film surface, electron emission sites are generally distributed randomly. The electron emission sites are associated with the highly conducting clusters of sp^2 -carbon, which are isolated from one another by sp^3 -carbon domains in DLC materials. The distribution of these sp^2 -carbon domains is an important factor for the application of these films in electronic devices, such as field emission displays.

Pure ta:C films are a weak p-type semiconductor that can be converted into an n-type material by nitrogen incorporation.^{22, 74-76} Robertson et al. proposed a schematic density of states for nitrogen in ta:C to explain the doping mechanism.⁴¹ At lower nitrogen levels (< 1%), nitrogen does act as n-type dopant. The conductivity increases due to the Fermi level shift into the conduction band. At moderate levels (1%~10%), nitrogen helps the existing sp^2 -bonded carbon to cluster. The conductivity increases as the band gap decreases because of the clustering. When the nitrogen level is less than 10%, the sp^3 -bonded carbon and optical gap remain constant. At higher nitrogen levels (> 10%), the content of sp^3 -bonded carbon decreases and new sp^2 -

bonded carbon is formed as C=N. Therefore, the nitrogen incorporation during the deposition of ta:C films alters the electronic properties.

In this work, ta:C and N-ta:C films were synthesized by pulsed laser-arc deposition (PLD). The N-ta:C films were deposited in the presence of nitrogen gas at flow rates of 10, 30 and 50 sccm. We report on the morphology and heterogeneous electronic properties of ta:C and N-ta:C films as assessed by conducting-probe AFM. Atomic force microscopy (AFM) was used to probe the film morphology in the contact mode. The bulk electrical properties were assessed by four-point probe resistivity measurements. Conductive-probe atomic force microscopy (CP-AFM) was used to map the morphology and electrical conductivity of these films.

4.1.2 CP-AFM Images and Topography of the ta:C and N-ta:C Films

While four-point probe resistivity measurements provide information about a film's bulk electrical properties, CP-AFM provides spatially-resolved information on the electrical properties (i.e., local electrical conductivity). Figure 4.1 shows (A) height mode and (B) deflection mode images, and (C) electrical conductivity maps ($1 \times 1 \mu\text{m}^2$) for a ta:C and N-ta:C films. The electrical conductivity map was obtained for bias voltage of +0.2 V (tip relative to the ta:C film). The height and deflection-mode images reveal the characteristic nodular film morphology. For example, there is a cluster of nodules (50-100 nm high) running across the center of the image.

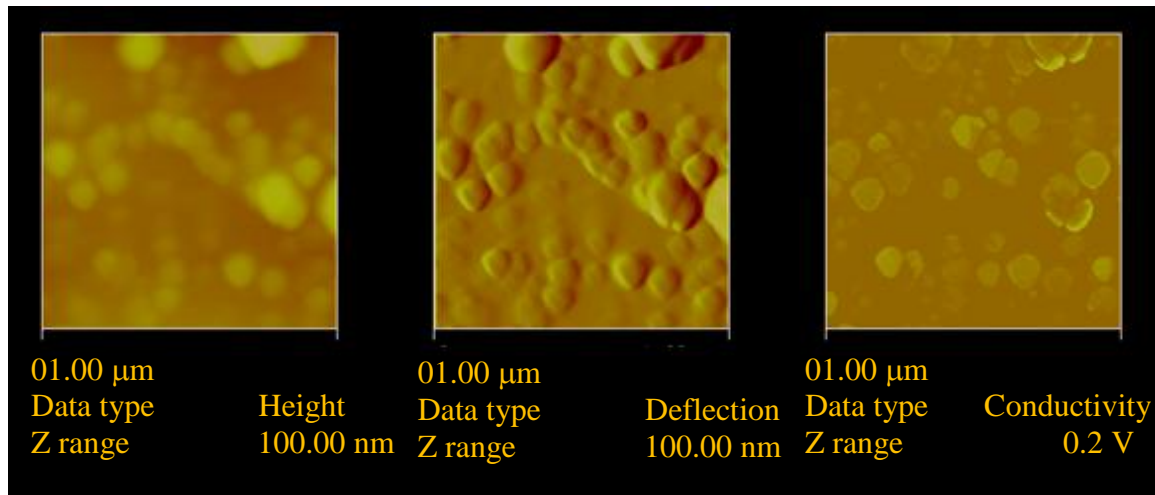


Figure 4.1 AFM images ($1 \times 1 \mu\text{m}^2$) for 10 sccm N-ta:C film: (A) height mode; (B) deflection mode and (C) conductivity mode.

The conductivity map reveals that most of the nodular features exhibit higher electrical conductivity than the surrounding film. The brighter spots (higher current) in the conductive mode (C) image correspond to the nodules in the deflection mode image (B). Similar results were found for the other films. One interesting phenomenon is the brighter color on the edge of some particles in image C. The trend was found for all of the films. This may be explained by a decreased contact resistance, R .

$$R = 4\rho l / 3\pi a^2 \quad [3]$$

where ρ is the resistivity, l is the electron mean free path in the electrode and a is the tip radius.¹⁰⁰ The tip curvature radius is approximately 50 nm, which is comparable to the nodular structure (ca. 100 nm) of all ta:C and N-ta:C films. For the 30 sccm and 50 sccm N-ta:C films, the density of the nodules was highest. Previously reported, EELS data showed that the 30 sccm and 50 sccm N-ta:C films possess ca. 51% and 58% sp^2 -bonded carbon, respectively. On the other hand, theta:C and 10 sccm N-ta:C films possess similar sp^2 -bonded carbon contents (ca.

44%). Therefore, we suppose the larger contact area and increased sp^2 -bonded carbon content are the reasons for the higher currents with the 30 sccm and 50 sccm N-ta:C films. One interesting observation is that larger currents were measured near some nodule edges. At the nodules, the pyramidally shaped tip will have a larger contact area with the film leading to a higher current (i.e. reduced resistance).

4.1.3 Effect of Bias Voltage Polarity and Magnitude

Figure 4.2 shows conductivity maps ($1 \mu\text{m} \times 1 \mu\text{m}$) for the same area of a 10 sccm N-ta:C film using tip voltages of (A) + 0.2 V and (B) – 0.2 V relative to the substrate. The current along a line profile is also shown. From the line profiles, one can see the highest currents are recorded at the edge of the nodules where the tip is expected to have the greatest contact area with the surface. With the exception of one location (ca. 0.25 μm mark) under the +0.2 V bias, the line profiles for the two bias voltages are mirror images of one another with nearly identical current magnitudes at each location. Similar results were observed for the ta:C, 30 sccm and 50 sccm N-ta:C films. At most locations on this ta:C film, current flow between the tip and film is characteristic of an ohmic or non-rectifying junction. In other words, current flows easily from the tip into the film or from the film and into the tip. Interestingly, there are regions in between the conducting zones that are insulating.

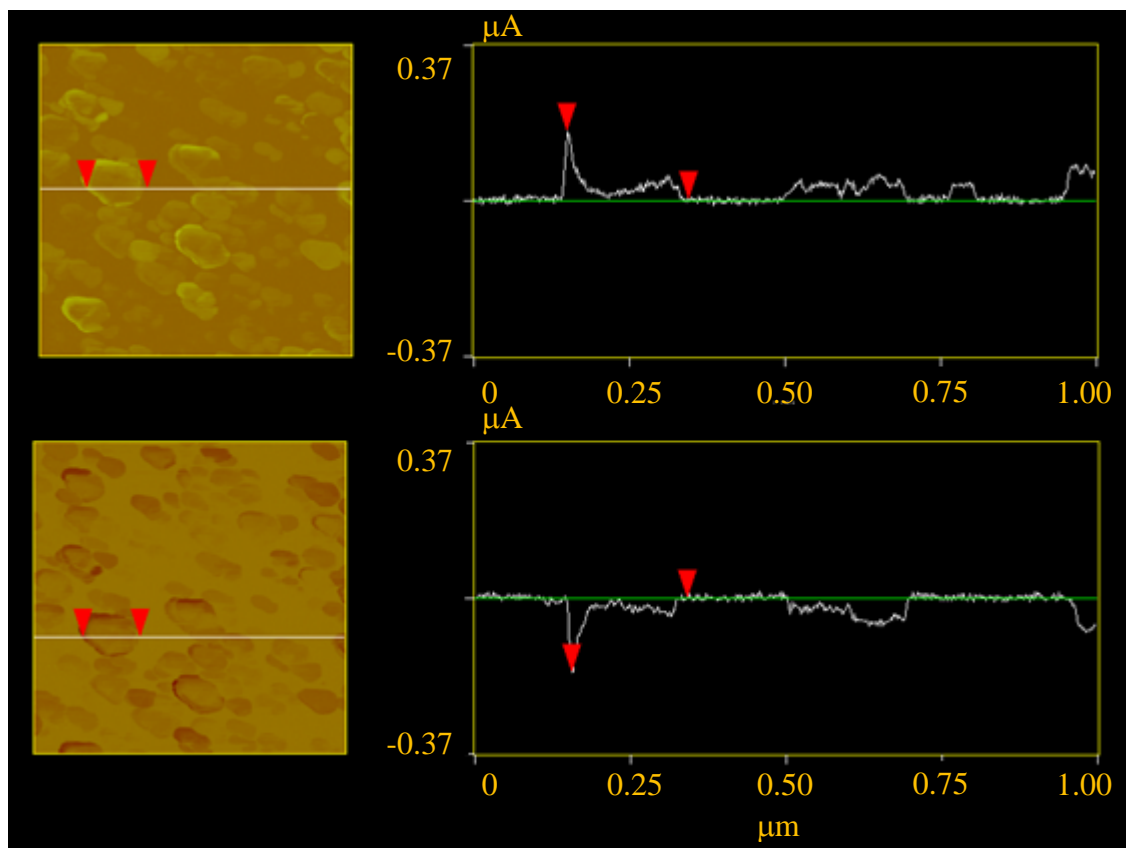


Figure 4.2 CP-AFM images with line profiles ($1 \times 1 \mu\text{m}^2$) for 10 sccm N-ta:C film at bias voltages of (A) +0.2 V or (B) -0.2 V.

To test the relationship between the bias voltage magnitude and the current, we recorded conductivity maps as a function of the tip voltage. Figure 4.3 shows the conductivity maps at a tip voltages of (A) + 0.2, (B) +0.4, (C) + 0.6 and (D) + 0.8 V relative to the substrate for a 10 sccm N-ta:C film. The same nodular morphology is seen for this film along with the more conducting nodular features. With increasing tip voltage, the conducting features do not change shape or increase in number. The current simply increases proportionally. The linear increase in the current with tip voltage characteristic of most sites on the different films studies is shown in Figure 4.2. This behavior is characteristic of ohmic and not Schottky behavior.

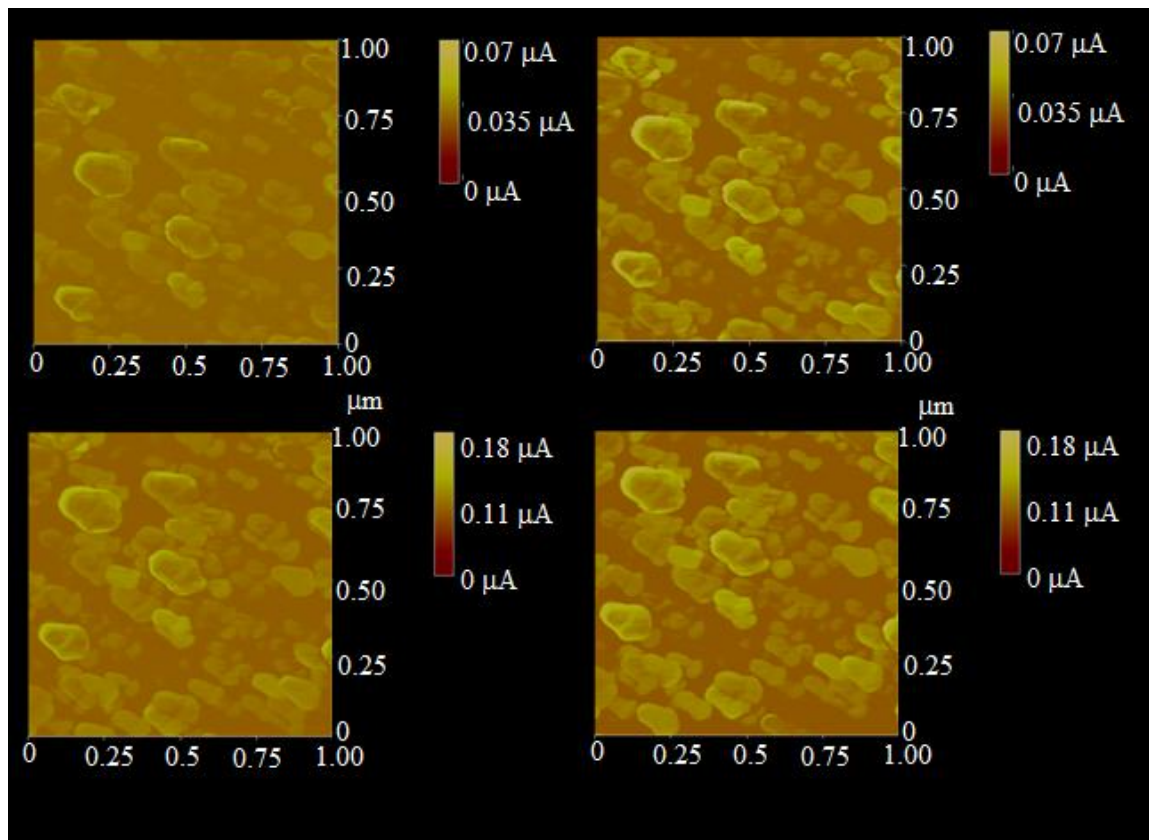


Figure 4.3 CP-AFM images ($1 \times 1 \mu\text{m}^2$) for 10 sccm N-ta:C film with bias voltage of (A) +0.2 V, (B) +0.4 V, (C) +0.6 V and (D) +0.8 V.

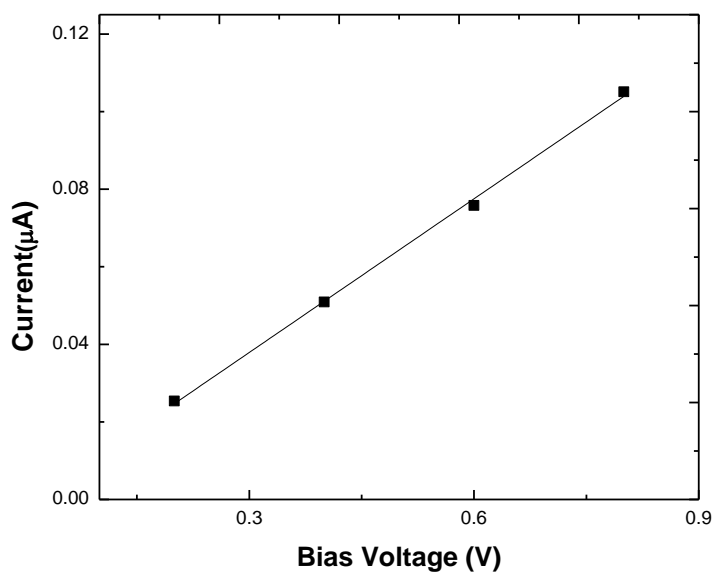


Figure 4.4. Current vs bias voltage curve for 10 sccm N-ta:C film.

The contact resistance at this film location was obtained from the slope of the I-V curve. Four different spots on a sample were processed with the same procedure. The results are summarized in Table 4.1. The 10 sccm N-ta:C film has the highest nominal resistance (ca. 7.12 MΩ). The 30 sccm and 50 sccm N-ta:C films have similarly lower values a (ca. 0.19 MΩ). A value of ca. 1 MΩ was recorded for boron-doped diamond using the same set up.⁸² As found in the four-point probe measurements, incorporating nitrogen into these films reduces the sheet resistance. But we also need to consider the resistance in the film, the ta:C or N-ta:C film, the interface between the Si and ta:C, Si and the conducting Si substrate. The total resistance is the sum of the resistance between the tip and the film, the resistance of the film and the resistance between the film and Si substrate. In order to make sure this was not the artifact of sample preparation, another 10 sccm N-ta:C film was prepared under the same method and the CP-AFM data were similar. For the 10 sccm N-ta:C film, the fraction of conductive area was also the least among these films since density of the nodular structure was lowest.

Sample(n=4)	Resistance (MΩ)
ta:C	2.15± 0.31
10 sccm N-ta:C	7.12±2.30
30 sccm N-ta:C	0.19±0.006
50 sccm N-ta:C	0.19±0.007

Table 4.1 Contact resistance from I-V curves for ta:C and N-ta:C films

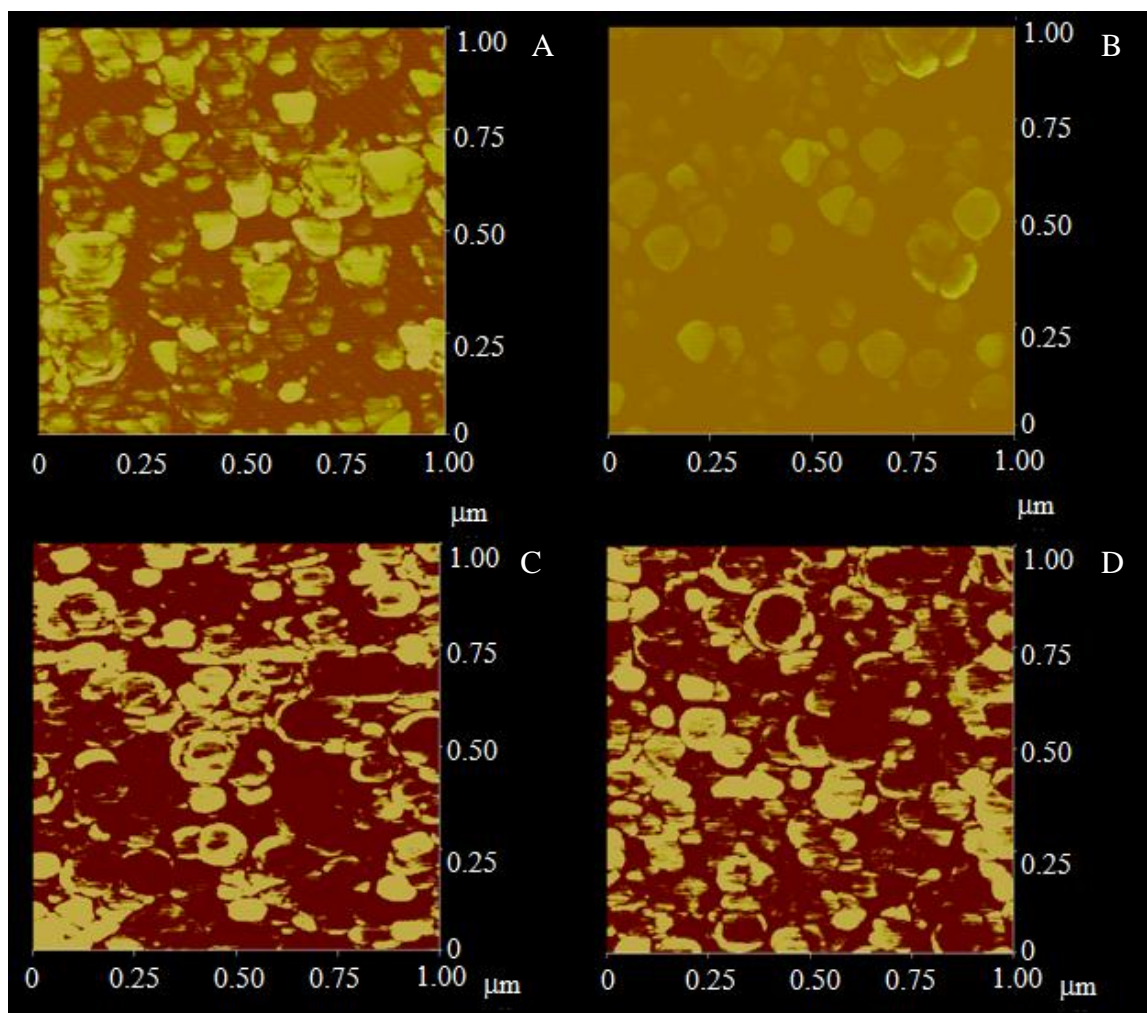


Figure 4.5 CP-AFM images ($1 \times 1 \mu\text{m}^2$) for (A) ta:C, (B) 10 sccm, (C) 30 sccm and (D) 50 sccm N-ta:C films at a bias voltage of + 0.2 V. The current ranged from 0 to 0.07 μA .

Figure 4.5 shows the conductivity maps for all films. The 10 sccm N-ta:C film had the lowest current value and the lowest fraction of conductive sites. In contrast, the 30 sccm and 50 sccm N-ta:C films had the largest current. The largest fraction of conductive sites was seen for the 50 sccm N-ta:C film. The conductive sites coincide with the nodular structure on the films. The higher current value for the 30 and 50 sccm N-ta:C films could be due to the lower contact resistance between the tip and film and/or the lower resistance through the film. The increased

level of sp^2 -bonded carbon in 30 and 50 sccm N-ta:C films correlates with a decreased film resistance, based on the four-point probe measurements.

4.1.5 Conclusions

The ta:C and N-ta:C films were grown by pulsed-laser arc deposition. A film with a nodular structure, which was composed of sp^2 -bonded carbon, was formed on the substrate surface. The nodular feature consists of sp^2 -bonded carbon. Contact-mode AFM images showed the nodular structures for all films. The density of the nodules increased with increasing nitrogen content. Resistance measurements were carried out by four-point probe measurement. The resistance was significantly decreased by introducing nitrogen in the film due to the increase of content of sp^2 -bonded carbon.

CP-AFM revealed the high conductivity of the nodules. The heterogeneous distribution of the nodules results in nonuniformity of the conductivity across the film. The conductive sites are ohmic and exhibit metal-like electronic properties. The high roughness for ta:C and N-ta:C films (10-20 nm) could offer high surface area. The real surface area of these films was larger than the geometrical area. This could explain why the capacitance of ta:C and N-ta:C films had higher value than that of boron-doped diamond(BDD).¹⁰¹ For BDD, the conductive area (0.5-2 μm) is randomly and nonuniformly distributed over the surface. The electron transfer happens through a partially blocked electrode which is consisted by highly conductive sites isolated by less conductive sites.¹⁰²⁻¹⁰³ Similar with BDD, the ta:C and N-ta:C films pose the conductive

sites separated by the non or less conductive sites. The difference is the density of conductive sites is higher than that of BDD and also the size of the nodular structure (ca.100 nm) is much smaller than BDD. By adding nitrogen in the film, the 30 sccm and 50 sccm N-ta:C films'conductive sites increased due to the increased content of the sp^2 -bonded carbon. Robertson et al, has been discussing the role of nitrogen incorporation.^{22, 76} At low nitrogen level, nitrogen behaved as substitution atom and the sp^3 fraction stayed constant. At intermediate nitrogen level, nitrogen helps the clustering of the sp^2 -bonded carbon. At high nitrogen level, new sp^2 -bonded carbon was formed with nitrogen. The nitrogen content was measured by XPS in our previous paper.¹⁰¹ Even though the nitrogen signal raised from the atomic content in the near surface region (ca.10 nm), we presumed that bulk of the film was same as the near surface level since the film was relatively thin (ca. 200 nm). The XPS data showed that N/C ratio for 10 sccm N-ta:C film was ca. 6% and the nitrogen encouraged the clustering of the sp^2 -bonded carbon. The EELS data showed that 10 sccm N-ta:C film had similar sp^2 -bonded carbon as ta:C film (ca. 44%). For the 30 sccm and 50 sccm N-ta:C films, N/C ratio was ca.10% and 13%. At this nitrogen level, the content of sp^2 -bonded carbon was increased due to the new sp^2 -bonded carbon. EELS data showed that the content of sp^2 -bonded carbon did increased (ca.51% for 30 sccm and 58% for 50 sccm N-ta:C films). This could explain why the 10 sccm N-ta:C film had less conductive sites and 30 sccm and 50 sccm N-ta:C films' conductive sites increased with nitrogen content. The increased sp^2 -bonded carbon in 30 sccm and 50 sccm N-ta:C films is part of the reason for the highest current on the CP-AFM images.

4.2 Heterogeneous Electrochemical Properties of N-ta:C Films

4.2.1 Introduction

SECM is a measurement of the current on an ultramicroelectrode (UME) when a UME approaches to a substrate in a few micrometers and probes the electrochemical activity across the surface.¹⁰⁴ The UME has radius around 10 μm .

During the movement to the substrate surface, there is perturbation between UME and substrate and this can offer information about the nature and properties of the substrate. Typically,

the tip potential is chosen to fully oxidize or reduce a mediator species in solution.

The measured current is controlled by the flux of mediator, which depends on the properties of the substrates and the distance between the UME and substrate. By keeping the distance constant, the current is only controlled by the properties of substrate. There are two common imaging modes: tip-generation/substrate-collection (TG/SC) and tip-collection/substrate-generation (TC/SG). For TG/SC, the tip is held at a potential where an electrode reaction occurs. If the substrate is conductive, the substrate could be held at a different potential where a product of the tip reaction will react. The product of the substrate reaction will diffuse to the tip and flux at the tip increases, which leads to an increase of the tip current. This is called positive feedback TG/SC mode. Figure 4.6 shows the general principle of this mode. If the substrate is non conductive, the substrate will hinder diffusion of redox species to the tip and the tip current

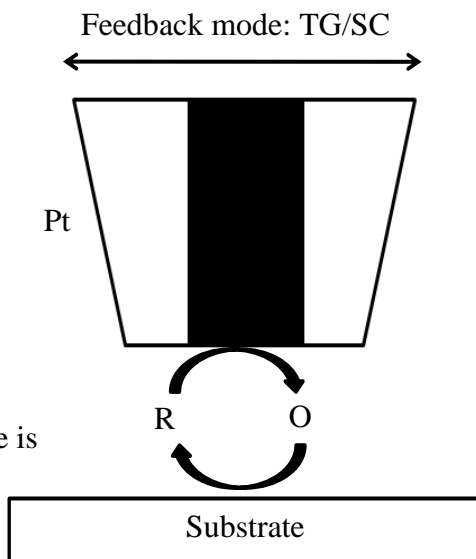


Figure 4.6 General principle of the positive feedback mode for an SECM measurement.

decreases. This is the negative feedback TG/SC. By scanning across the surface of a substrate and recording the tip current, the electrochemical activity of the substrate could be revealed.

4.2.2 Tip Conditioning

The resolution in an SECM measurement strongly depends on the tip diameter. The smallest diameter of commercially available Pt microelectrodes is 10 μm . All microelectrodes were cleaned by the method as described in Section 2.4.2. Cyclic voltammetry in 0.1 M HClO_4 was carried out to assess electrode surface cleanliness. Figure 4.7 shows a cyclic voltammetric i - E curve at 0.1 V/s for the last cycle. The characteristic features of clean Pt are seen: Pt oxide formation and oxide reduction, hydrogen adsorption and desorption.

Cyclic voltammetric i - E curves for 1 mM $\text{Fe}(\text{CN})_6^{4-}$ in 0.1M KCl was recorded to determine the tip diameter. An example is shown in Figure 4.8. Clearly, a sigmoidal, steady-state current response is seen, as expected for a small diameter microelectrode. According to¹⁰⁴

$$i_{T,\infty} = 4nFD Cr_0(1)$$

$i_{T,\infty}$ is the steady-state current for a disk-shaped microelectrode, n is the number of electrons transferred in the reaction, F is the Faraday, D is the diffusion coefficient, C is bulk concentration and r_0 is the tip radius. The calculated radius/diameter was very close to the actual radius/diameter determined by electron microscopy.

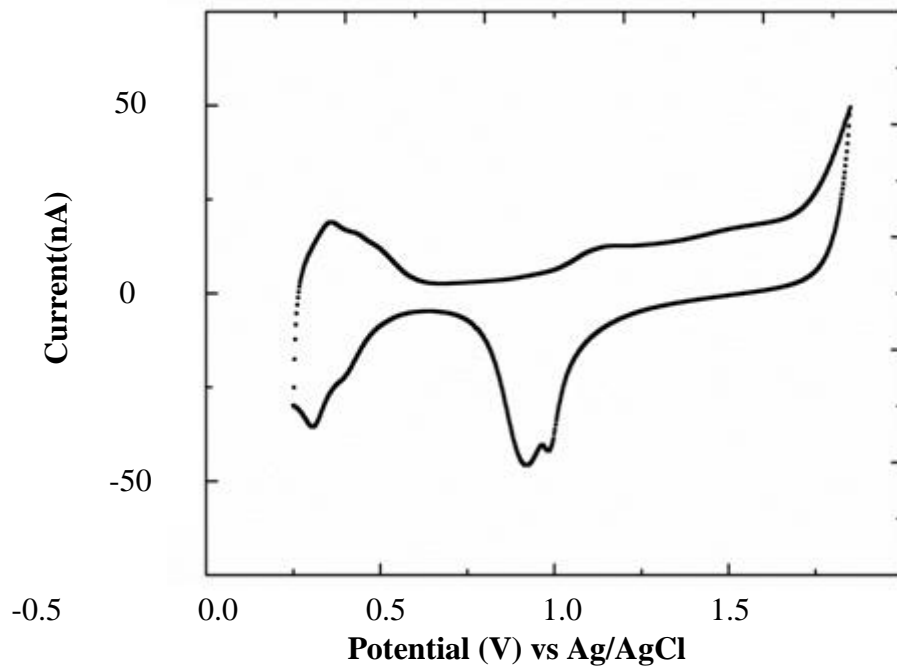


Figure 4.7 Cyclic voltammetric *i-E* curve for the Pt microelectrode in 0.1 mol/L HClO₄ at 0.05 V/s.

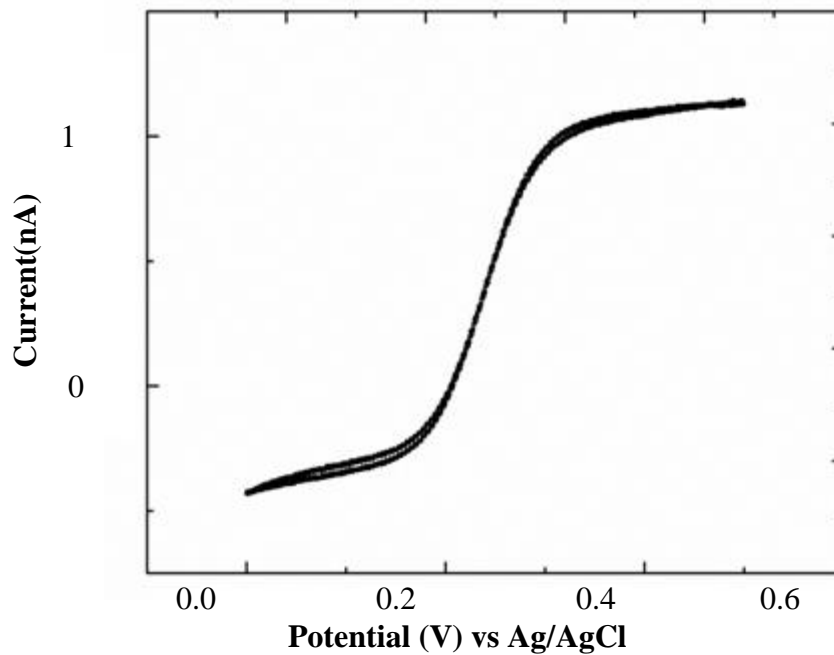


Figure 4.8 Cyclic voltammetric *i-E* curve for Pt microelectrode in 1 mmol/L Fe(CN)₆⁴⁻ 1M KCl. Scan rate = 0.05 V/s.

4.2.3 Tip Approach Curves

Prior to imaging, recording tip approach curves can be used to ascertain if the local region is electrically conductive and active for the redox probe or more insulating and less active. A tip approach curve is simply a plot of tip current vs. tip-substrate distance. There are two pieces of information that tip approach curve can offer. One is the distance between tip and the substrate. Another is the electrochemical properties of the substrate.

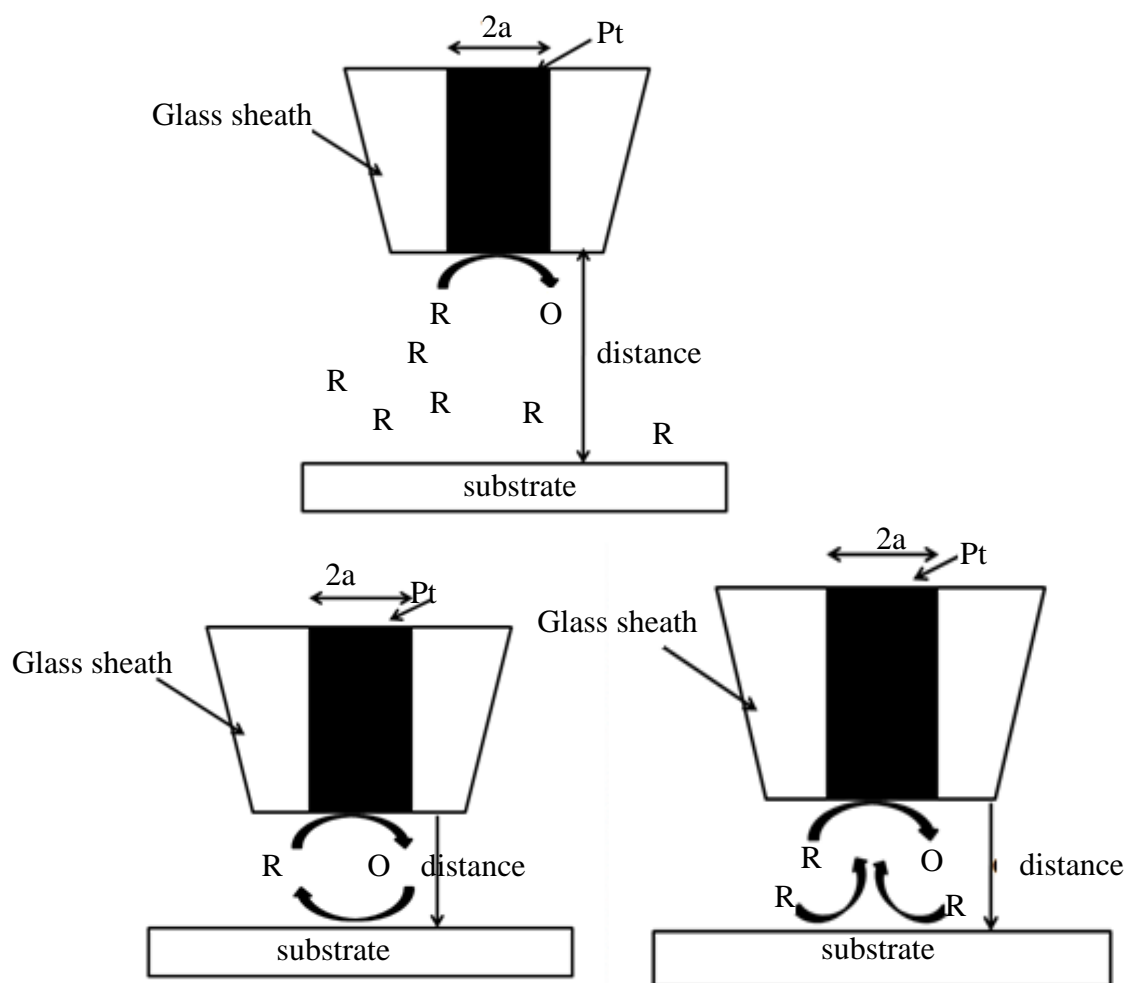


Figure 4.9 Fundamental principles of an SECM measurement. (A) Tip is far away from substrate (hemispherical diffusion). (B) Tip is close to the substrate (regeneration reaction or positive feedback). (C) Tip is close to the substrate (hindered diffusion or negative feedback).

Figure 4.9 shows the fundamental principles of SECM. When the tip is far away from the substrate (Figure 4.9A), the microelectrode measures the mass transfer limited steady state current. As the tip approaches the substrate electrode, the processes occurring at the substrate electrode become important. If the substrate electrode is a conductor, where the $O + ne \rightarrow R$ reaction can occur, an increase current with distance relative to the steady state current will take place. This is called positive feedback as shown in Figure 4.9B. If on the other hand, the substrate electrode is insulating, where the $O + ne \rightarrow R$ reaction cannot occur, the electrode blocks diffusion of R and the concentration of R around the microelectrode decreases (Figure 4.9C). As a result, the tip will collect smaller current with distance relative to the steady state current and this is called negative feedback. The tip will stop automatically according to a pre set-point. The pre set-point is the ratio of i_T vs $i_{T,\infty}$. $i_{T,\infty}$ is the steady state current when the tip is far away from the substrate. i_T is the current recording during the approach process. In $\text{Ru}(\text{NH}_3)_6^{3+/2+}$, the $i_T/i_{T,\infty}$ was set to 1.3. In $\text{Fe}(\text{CN})_6^{3-/4-}$, the $i_T/i_{T,\infty}$ was set to 1.5. When the tip stopped once the $i_T/i_{T,\infty}$ reached the set point, the distance between the tip and substrate could be calculated by the following equation:¹⁰⁴

$$\frac{i_T}{i_{T,\infty}} = \left(\frac{\pi}{4}\right)\left(\frac{a}{d}\right) + 0.901 + 0.099\exp\left[-0.16\frac{a}{d}\right] - 0.29\exp\left[-0.39\frac{d}{a}\right] \quad (2)$$

Where i_T is the tip current at any position, $i_{T,\infty}$ is the limiting current measured when the tip is far away from the substrate, a is the tip radius and d is the distance between the tip and the substrate.

Figure 4.10 showed the tip approach curves for ta:C and N-ta:C films in 1 mM $\text{Ru}(\text{NH}_3)_6^{3+/2+}$ /1M KCl. $\text{Ru}(\text{NH}_3)_6^{3+/2+}$ is outer-sphere redox couple and involves simple

electron transfer. The electrode kinetics for this redox couples is relatively insensitive to the surface microstructure, surface oxides and the adsorbed monolayers on sp^2 carbon electrodes.^{6-7,}
⁹⁰ Their electron transfer rate are mainly controlled by the electronic properties of the electrodes (i.e., carrier mobility and carrier concentration). On all of the ta:C and N-ta:C films, all of tip approach curves were almost identical to each other and

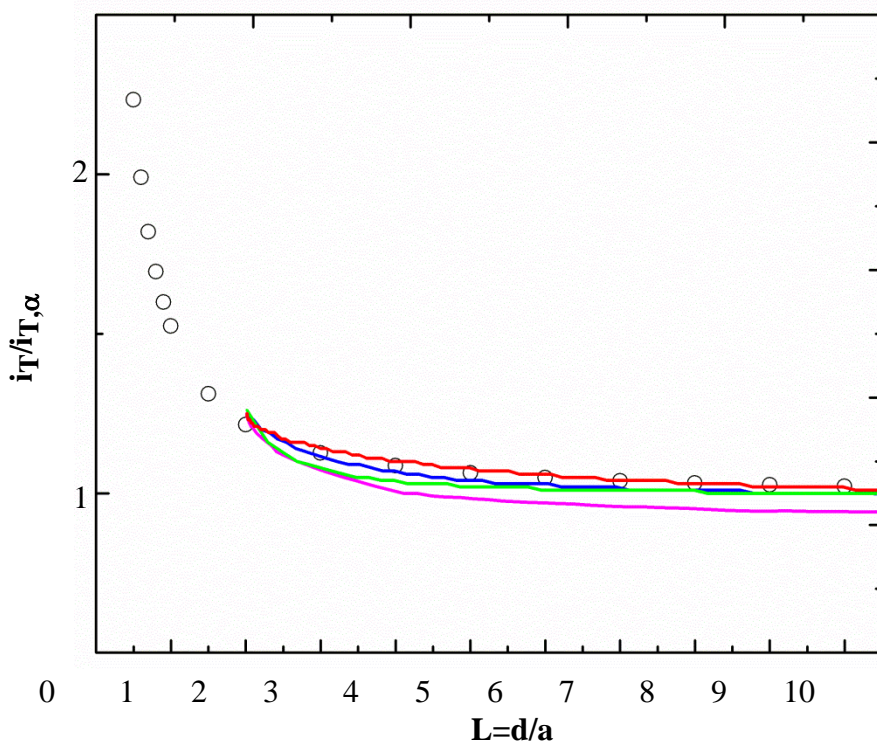


Figure 4.10 Approach curves for ta:C and N-ta:C films in 1 mM $\text{Ru}(\text{NH}_3)_6^{3+/2+}$ /1M KCl. The microelectrode was held at -0.3 V and the substrate was held at 0 V vs Ag/AgCl. $L=d/a$, where d is the distance between the tip and the substrate, a is the tip radius. i_T is the tip current and $i_{T,\infty}$ is the limiting current.

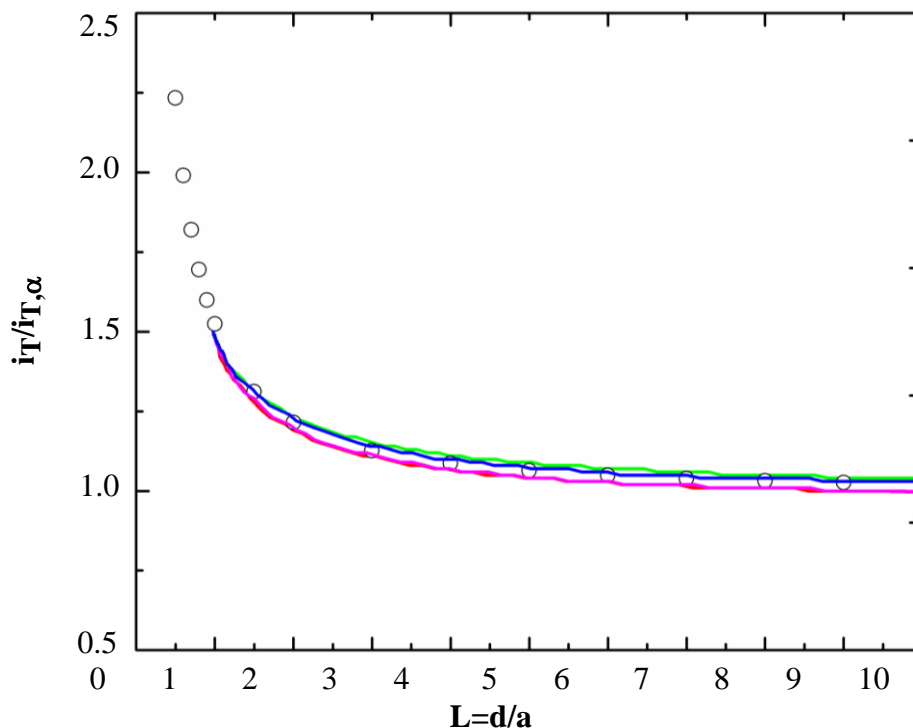


Figure 4.11 Approach curves for ta-C and N-ta:C films in 1 mM $\text{Fe}(\text{CN})_6^{3-/4-}$ /1M KCl. The microelectrode was held at 0 V and the substrate was held at +0.4 V vs Ag/AgCl. $L=d/a$, where d is the distance between the tip and the substrate, a is the tip radius. i_T is the tip current and $i_{T,\infty}$ is the limiting current.

were positive feedback. The pre set-point for $i_T/i_{T,\infty}$ was 1.25, according to equation 1, the calculated d was 10.7 μm . The theoretical approach curve under the same condition was also shown for comparison. The tip potential was held at -0.3 V vs Ag/AgCl to make sure the full reduction of $\text{Ru}(\text{NH}_3)_6^{3+}$. The substrate potential was held at 0 V vs Ag/AgCl to make sure the full oxidation of $\text{Ru}(\text{NH}_3)_6^{2+}$. The tip current was decided by the solution composition, the distance from the tip to the substrate and electrochemical properties of electrode substrate.¹⁰⁵

During the approach process, $\text{Ru}(\text{NH}_3)_6^{2+}$, from the reduction reaction from the tip, was oxidized back to $\text{Ru}(\text{NH}_3)_6^{3+}$. The oxidation product diffused to the tip and caused an increase

in the flux of $\text{Ru}(\text{NH}_3)_6^{3+}$ compared with $i_{T,\infty}$. The positive feedback for ta:C and N-ta:C films meant all of these films' surface were conducting.

Figure 4.11 showed the tip approach curves for ta:C and N-ta:C films in 1 mM $\text{Fe}(\text{CN})_6^{3-}$ /1M KCl. $\text{Fe}(\text{CN})_6^{3-/4-}$ is an inner-sphere redox couple and the rate of the electron transfer is influenced by several variables⁷: (1) the electronic properties of the electrodes (local carrier concentration and mobility); (2) surface cleanliness (3) surface chemistry. The electrochemical kinetics of $\text{Fe}(\text{CN})_6^{3-/4-}$ has been widely studied. For metal and sp^2 carbon electrodes, there are several factors that can influence the electrode kinetics.^{6-7, 90} First, the heterogeneous rate constant is strongly influenced by the fraction of edge plane of exposed on sp^2 carbon electrodes. Second, surface cleanliness is important, as are the electrolyte type and concentration. The rate of reaction increases with electrolyte composition in the order of $\text{LiCl} < \text{NaCl} < \text{KCl}$.¹⁰⁶⁻¹⁰⁷ The electron transfer rate constant in 1M KCl is ~10 higher than that of 1M LiCl for both gold and glassy carbon electrodes. Third, the rate of reaction could be decreased by the adsorbed monolayer on sp^2 carbon electrodes.

The pre set-point was 1.5 and the calculated d was 4.9 μm . The tip potential was held at 0 V vs Ag/AgCl to fully reduce $\text{Fe}(\text{CN})_6^{3-}$. The substrate potential was held at 0.4 V vs Ag/AgCl to fully oxidize $\text{Fe}(\text{CN})_6^{4-}$. The positive feedback told us that the ta:C and N-ta:C films were conductive. Same was in $\text{Ru}(\text{NH}_3)_6^{3+/2+}$, all of the approach curves in $\text{Fe}(\text{CN})_6^{3-/4-}$ were positive feedback.

After finishing the tip approach curves, the protocol was switched to imaging the electrochemical activity across the substrate surface using the constant mode in 1 mM $\text{Ru}(\text{NH}_3)_6^{3+/2+}$ /1M KCl or 1 mM $\text{Fe}(\text{CN})_6^{3-/4-}$ /1M KCl.

4.2.4 SECM Images for N-ta:C Films in $\text{Ru}(\text{NH}_3)_6^{3+/2+}$ /1M KCl

SECM images were also obtained in 1mM $\text{Ru}(\text{NH}_3)_6^{+3/+2}$ +1M KCl. $\text{Ru}(\text{NH}_3)_6^{3+/2+}$ is an outer-sphere redox couple as the electrochemical kinetics primarily depend on the electronic properties of the electrode. Figure 4.12 shows image maps for a series of ta:C film in 1mM $\text{Ru}(\text{NH}_3)_6^{+3/+2}$ +1M KCl. The current at infinite distance, $i_{T,\infty}$, is 2.3 nA. In Figure 4.12A a large fraction of the imaged area shows high activity for the redox reaction. The 10 sccm N:ta-C film was all conductive (Figure 4.12.b). Similar results showed in 30 sccm N:ta-C and 50 sccm N:ta-C films. The highest current in each film is increased by increasing the nitrogen flow rate. This might prove the conductivity of ta-C films was increased by incorporation of nitrogen. On all of these films, in the scanning range ($500 \times 500 \mu\text{m}^2$) there were some areas that were less conductive. The transition between the more conductive and less conductive zones was very clear. The distribution of the conductive sites was not uniform on the ta:C and N-ta:C films. CP-AFM data showed the conductive nodules (100-200 nm) on the surface. In SECM, the microelectrode's radius was around 5 μm . The resolution of SECM was much lower than the CP-AFM. The ta:C and N-ta:C films behaved like micro-electron arrays. Since the distribution of nodules was not uniform, when the tip scanned at zones which had a certain amount of nodules, the SECM images showed high conductivity. When the tip scanned at zone where had less or none nodules, the SECM images showed low conductivity. The highest current increased by

increasing nitrogen content in these films. $\text{Ru}(\text{NH}_3)_6^{3+/2+}$ was out-sphere redox couple. Higher current meant higher kinetics and the kinetics depended on the electronic properties of the electrodes. So the nitrogen incorporation in the ta:C film improved the conductivity.

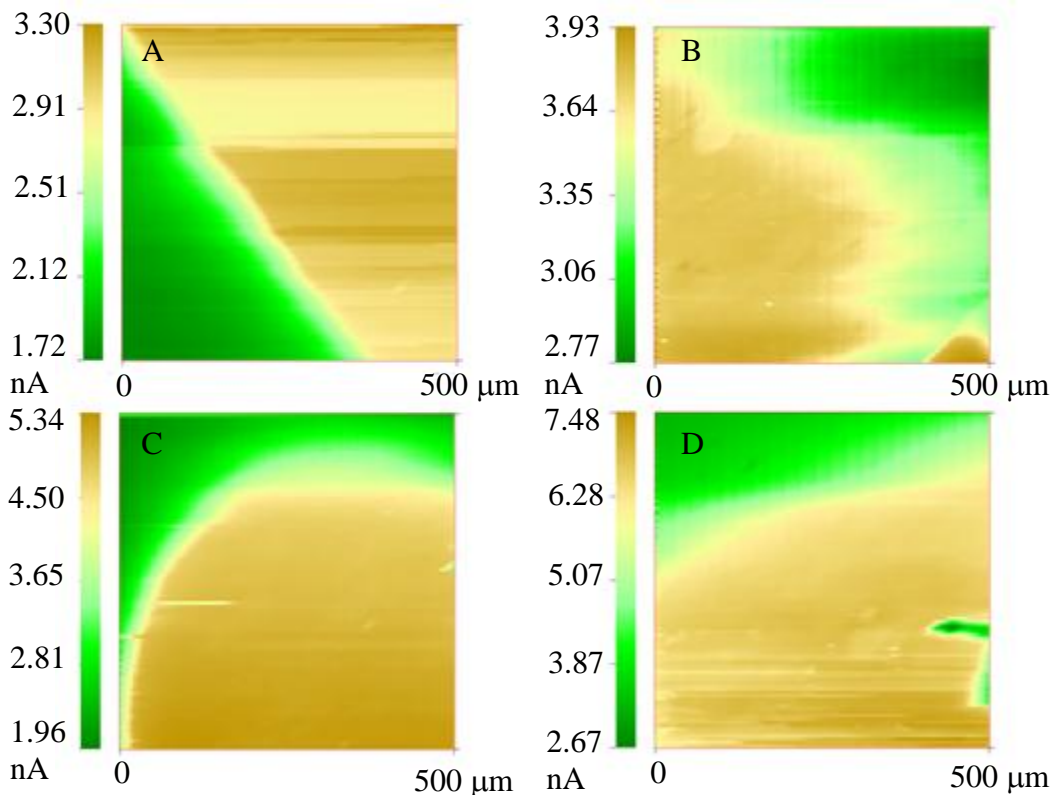


Figure 4.12 Feedback mode SECM images ($500 \times 500 \mu\text{m}^2$) in $1 \text{ mM Ru}(\text{NH}_3)_6^{2+/3+} + 1 \text{ M KCl}$ (A) ta:C, (B) 10 sccm N-ta:C, (C) 30 sccm N-ta:C, and (D) 50 sccm N-ta:C films. In all cases, the Pt probe tip diameter was $5 \mu\text{m}$. The tip potential was -0.3 V and the substrate potential was 0 V vs Ag/AgCl.

4.2.5 SECM Images for N-ta:C Films in $\text{Fe}(\text{CN})_6^{3-/4-}/1 \text{ M KCl}$

Figure 4.13 showed the SECM images acquired for ta:C films in $1 \text{ mM Fe}(\text{CN})_6^{3-/4-}$ in 1 M KCl . The steady-state current $i_{T,\infty}$ for $1 \text{ mM Fe}(\text{CN})_6^{3-/4-}$ was 1.4 nA . For ta:C film (Figure 4.13. a), image showed the whole areas was conductive as the current is greater than 1.4 nA . There was a large region which the current was higher than the rest, which indicated higher level

of electrochemical activity. As increasing nitrogen flow rate (i.e., nitrogen content), SECM images (Figure 4.13.b, c, d) revealed that these films exhibit electrochemical activity, except there is a tiny spot in 30 sccm N:ta-C film showing negative feedback. Another issue that should be addressed was that the highest current was increasing by increasing the nitrogen flow rate. For ta:C film and 10 sccm N-ta:C, the highest currents were ~ 2.3 nA and ~ 3.1 nA respectively. For 30 sccm N-ta:C and 50 sccm N-ta:C films, the highest currents were ~ 6.6 nA and ~ 5.2 nA. Since $\text{Fe}(\text{CN})_6^{3-/4-}$ was an inner-sphere redox couple, the increasing current might be due to the improvement of conductivity or the surface chemistry changed by the incorporation of nitrogen. Active regions were randomly distributed over the surface with some of them being close enough to create a zone (multiple micrometers in dimension).

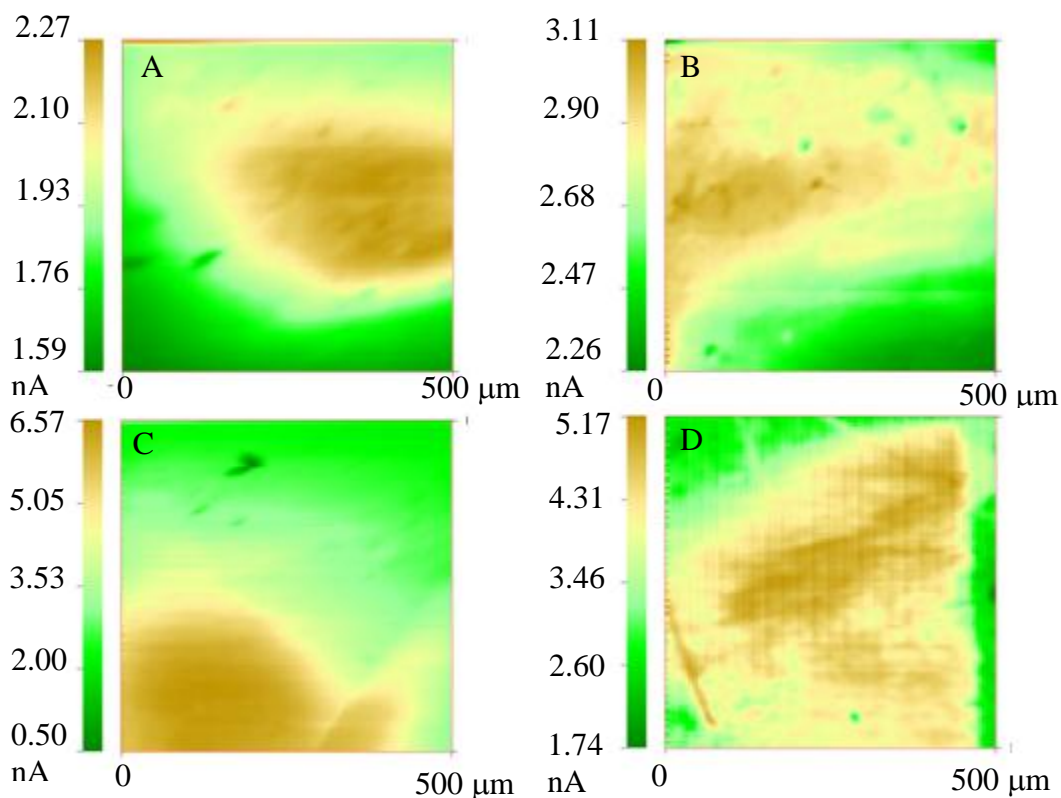


Figure 4.13 Feedback mode SECM images ($500 \times 500 \mu\text{m}^2$) in $1 \text{ mM Fe}(\text{CN})_6^{3-/4-} + 1 \text{ M KCl}$ at (A) ta:C, (B) 10 sccm N-ta:C, (C) 30 sccm N-ta:C and (D) 50 sccm N-ta:C films. In all cases, the Pt

probe tip diameter was 5 μm . The tip potential was 0 V and the substrate potential was 0.4 V vs Ag/AgCl.

4.2.4 Conclusions

SECM was used to investigate the spatial heterogeneity of the electrochemical activity across ta:C and N-ta:C films. For both the outer and inner-sphere redox system probes, all of these films showed the electrochemically active sites were isolated by less or non-conductive sites. The conductivity of these films increased by increasing nitrogen in these films. The heterogeneous electrochemical activity could help to understand the reaction mechanism of different redox couples on these films' surface. One interesting point is the area of the conductive area. These SECM images were scanning in $500 \times 500 \mu\text{m}^2$. If the conductive area could be calculated, the influence of the nitrogen could be figured out. One expectation is to scan SECM image in larger scale to see if the conductive sites were totally isolated from less or non-conductive sites and the scale of the individual conductive site.

Chapter 5. Application of Nitrogen-Containing Tetrahedral Amorphous Carbon (ta-C)

Thin-film Electrodes in Flow Injection Analysis

5.1. Introduction

Results in prior chapters indicate that the ta:C and N-ta:C films are excellent candidates for use in the electroanalytical measurements. These electrodes have properties similar to those of boron-doped diamond and, compared to conventional glassy carbon, the ta:C electrodes exhibit lower background currents, a wider working potential, better microstructure stability during the imposition of harsh chemical and or electrochemical conditions, and resistance to the adsorption of organic molecules. The latter property is important for electrode response stability in electroanalytical measurements; a critical figure of merit. Polar molecules tend to weakly adsorb onto hydrogen-terminated diamond thin-film electrodes. This bodes well for fouling resistance. We sought to determine if molecules that show strong adsorption onto sp^2 glassy carbon and weak adsorption on sp^3 diamond adsorb onto the mixed microstructure ta:C and N-ta:C thin-film electrodes. Methylene blue was the molecule selected for these studies. This molecule is an electroactive heterocyclic aromatic that strongly adsorbs onto glassy carbon surfaces.¹⁰⁸ It was hypothesized that ta:C electrodes are resistant to fouling making it possible to stably detect organic molecules without the fouling; an often encountered issue with glassy carbon.¹⁰¹

The catecholamines, dopamine (DA) and norepinephrine (NE), are important neurotransmitters in the central nervous system and play a significant role in psychiatric disorders, such as depression and gastrointestinal disorder.¹⁰⁹ Abnormal catecholamine

signaling is associated with certain diseases. For example, hypertension has been linked to the abnormal catecholamine levels in plasma.¹¹⁰ The traditional methods used for measuring catecholamines, such as absorption spectroscopy or mass spectroscopy, have their limitations.¹¹¹ Most of catecholamines are electrochemically active making electrochemical detection is good choice for detection.¹¹² Electrochemical detection requires relatively inexpensive instrumentation, and affords low detection limits and excellent sensitivity. Flow injection analysis (FIA) coupled with electrochemical detection is an analytical method useful for chemical analysis. In this method, a plug of sample is injected into carrier solution that flows through an electrochemical detector. Analyte molecules arriving at the working electrode are oxidized or reduced. FIA offers several advantages including: low sample and reagent consumption, rapid analysis time, incorporation of online matrix separation and pre-concentration phases.¹¹³⁻¹¹⁴ A traditional electrode for electrochemical measurements is glassy carbon(GC). This electrode is a microstructurally disordered sp^2 carbon and exhibits good electrochemical activity for a wide range of analytes. A limitation of glassy carbon is that it is prone to deactivation during exposure to complex media. Undesirable molecular adsorption (i.e., fouling) leads to attenuated current and sluggish reaction kinetics.¹¹⁵⁻¹¹⁶ Boron-doped diamond is an alternate to glassy carbon due to its superior performance characteristics including lower background current, excellent response precision, good stability and sensitivity.¹¹⁷ Our group has been published papers about the detection of catecholamines by flow injection analysis with amperometric detection.¹⁴ Other work in this dissertation showed that ta:C and N-ta:C films are excellent candidates for electroanalytical measurements with properties similar to those of

boron-doped diamond.¹⁰¹ Considering their milder growth conditions with BDD's, it will be a big contribution to the electrochemical detection of catecholamines if their figures of merit could be comparable with BDD.

In this study, we used the 30 sccm N-ta:C film as the detection electrode. This film has exhibits good electrochemical behavior (low background current, relatively rapid electron-transfer kinetics and microstructural stability during exposure to harsh conditions). Studies of the electrochemical detection of norepinephrine and dopamine are reported herein.

5.2 Cyclic Voltammetry of Dopamine and Norepinephrine

The redox reactions for these three analytes are presented below for dopamine (1) and norepinephrine (2).

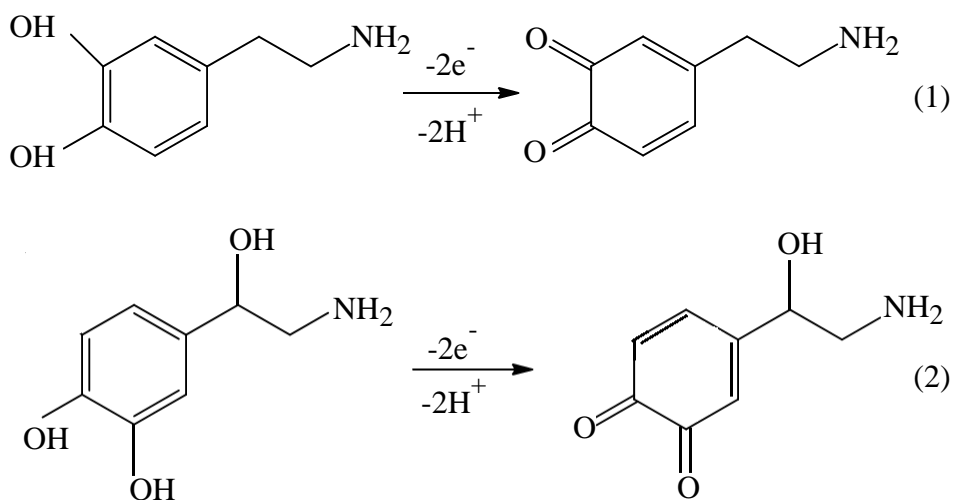


Figure 5.1A shows the first-scan cyclic voltammetric *i-E* curve for 10 μM dopamine (DA) at scan rate of 0.025 V/s. The solid line represented the background current in 0.1M PBS buffer solution. The dash line was cyclic voltammtric *i-E* curve in the presence of 10 μM DA. The dot line was cyclic voltammetric *i-E* curve obtained after applying the electrode in the presence of 10

μM DA, removing the solution and rinsing the electrode and replacing the solution with 0.1 M PBS buffer solution. The dot line almost matched the solid line, which meant that the 30 sccm N-ta:C film did not adsorption of oxidation product of DA, which was a serious issue for GC. Figure 5.1B showed the cyclic voltammetric i - E curves at different scan rate after background subtraction. All of these peaks were well-defined and i_p^{ox} increased by increasing scan rate from 0.025 V/s to 0.3 V/s. The insert graph in Figure 5.1B was the plot for current vs square root of scan rate, $v^{1/2}$. The R^2 for this plot was 0.992, which indicated the diffusion-controlled reaction of DA on the electrode surface. Oxidation peak potential (E_p^{ox}) offered the information about the energy that needed for the electron transfer between the electrode and the analyte. The higher value of E_p^{ox} , the more sluggish reaction kinetics on the electrode surface. From Figure 5.2B, at scan rate of 0.1V/s, the E_p^{ox} was 0.27 V vs Ag/AgCl. Under the same condition, E_p^{ox} was about 0.18 V vs Ag/AgCl for glassy carbon and 0.30 V vs Ag/AgCl for BDD.¹¹⁷ The peak separation value(ΔE_p) was reflected the heterogeneous electron transfer rate. At 100 mV/s, ΔE_p was 0.14 V for 30 sccm N-ta:C. For glassy carbon, ΔE_p was 0.081 V vs Ag/AgCl. For BDD, ΔE_p was 0.23~0.35 V vs Ag/AgCl. It is well-known that the adsorption of catechols on the electrode surface facilitates fast electron transfer kinetics.¹¹⁸ Since there was a certain amount of sp^2 -bonded carbon on the 30 sccm N-ta:C film, it could have adsorption sites for dopamine to enhance the sensitivity without fouling. Both the E_p^{ox} and ΔE_p reflected that the electron-transfer rate for N-ta:C film was between GC and BDD.

Figure 5.2 showed cyclic voltammetric *i-E* curves of 10 μM norepinephrine(NE) under same conditions as detecting serotonin. In Figure 5.2A, the cyclic voltammetric *i-E* curves before and after cycling with dopamine almost matched with each other. In Figure 5.2B, the currents after background subtraction were well-defined. The insert graph showed the linearity between the oxidation current and the square root of scan rate, $v^{1/2}$ ($R^2=0.995$). All of these confirmed the diffusion-controlled process of NE on the electrode surface. Figure 5.3 showed the cyclic voltammetric *i-E* curves in 10 μM norepinephrine. No adsorption of norepinephrine was observed on the film surface and the oxidation reaction of norepinephrine was diffusion-controlled reaction since the oxidation current was very linear with the square root of scan rate ($R^2=0.996$).

The cyclic voltammetry data for 10 μM of dopamine and norepinephrine showed that there was no observable adsorption of these catecholamines on 30 sccm N-ta:C film surface. The oxidation reaction of these catecholamines were diffusion-controlled reaction on the surface of 30 sccm N-ta:C film. The 30 sccm N-ta:C film could be applied in electrochemical-flow injection analysis (EC-FIA) for the detection of these catecholamines.

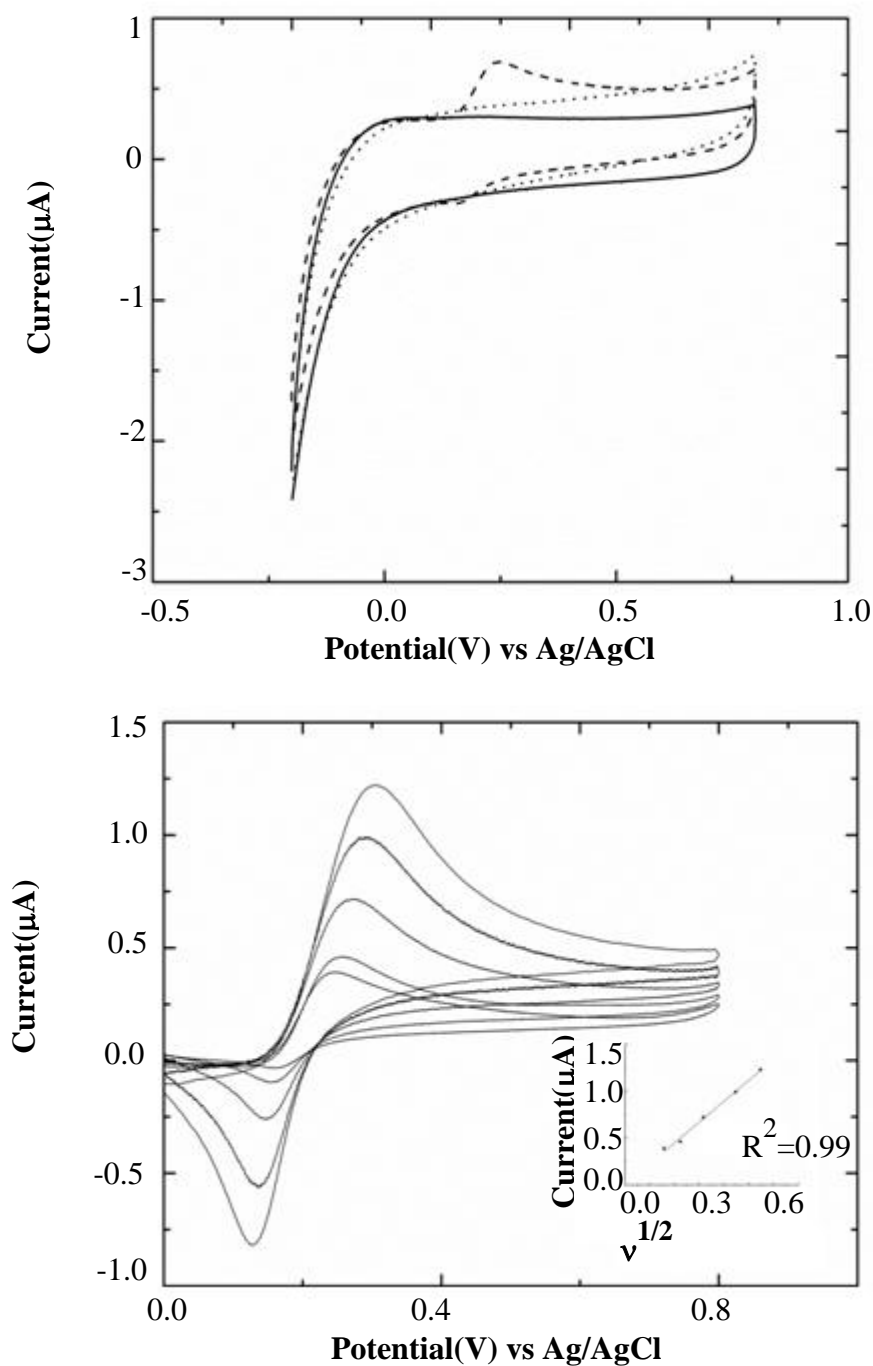


Figure 5.1(A) Cyclic voltammetric i - E curves at scan rate of 0.025 V/s for 30 sccm N-ta:C film in: 0.1M PBS(—), in 10 μ M dopamine(---) and in 0.1M PBS buffer after soaking(...); (B) Cyclic voltammetric i - E curves of first scan after background subtraction in 10 μ M dopamine at scan rate(v) of 0.025, 0.050, 0.100, 0.200 and 0.300 V/s, the insert graph was the i_p^{ox} vs $v^{1/2}$. Geometric area = 0.2 cm²

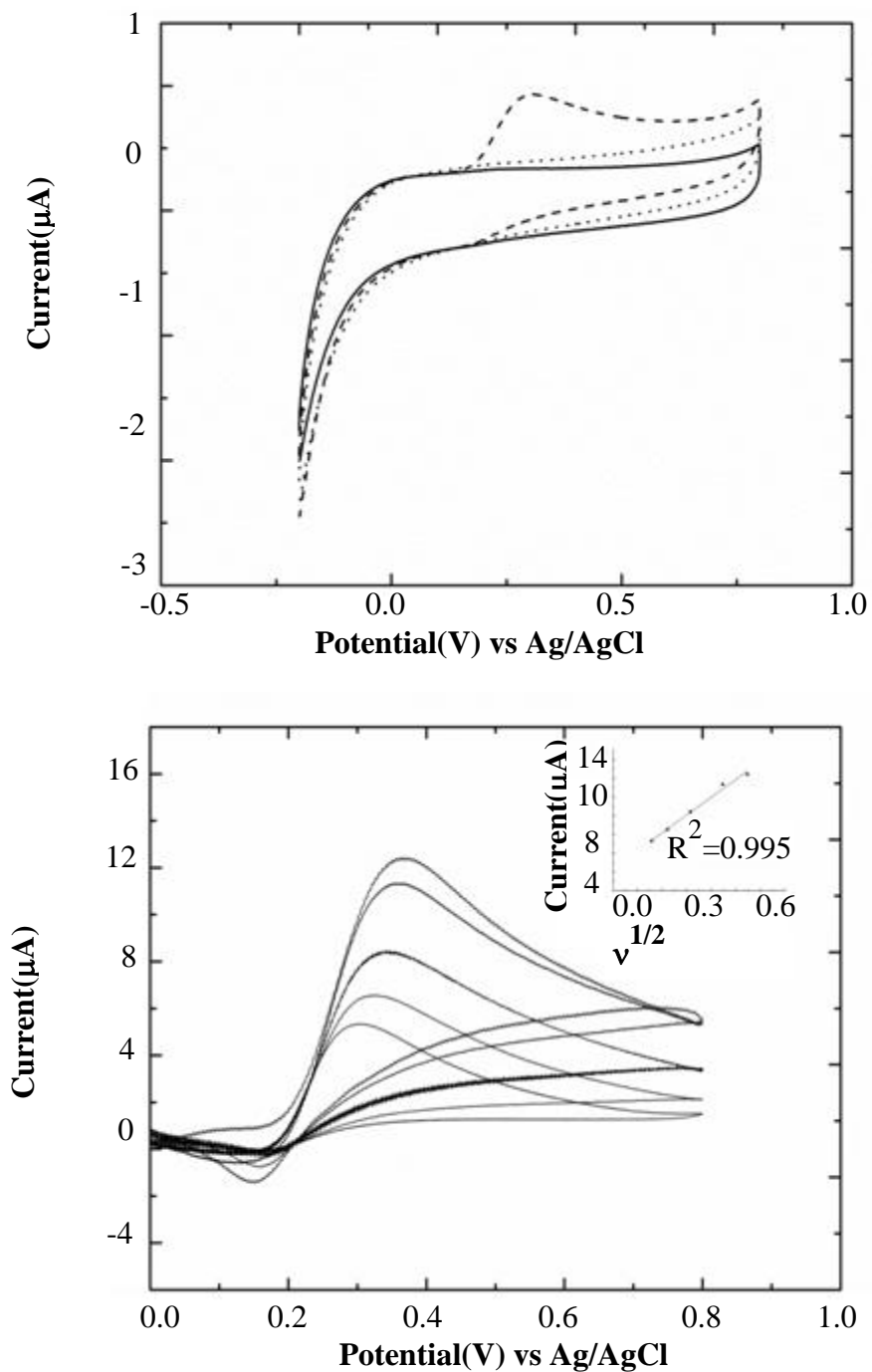


Figure 5.2 (A) Cyclic voltammetric $i-E$ curves at scan rate of 0.025 V/s for 30 sccm N-ta:C film in: 0.1M PBS buffer(—), in 10 μM norepinephrine (NE)(---) and in 0.1M PBS buffer after soaking(...); (B) Cyclic voltammetric $i-E$ curves of first scan after background subtraction in 10 μM norepinephrine(NE) at scan rate(ν) of 0.025, 0.050, 0.100, 0.200 and 0.300 V/s, the insert graph was the i_p^{ox} vs $\nu^{1/2}$. Geometric area = 0.2 cm^2 .

5.3 FIA-EC studies of Norepinephrine

5.3.1 Hydrodynamic Voltammetric *i-E* Curves

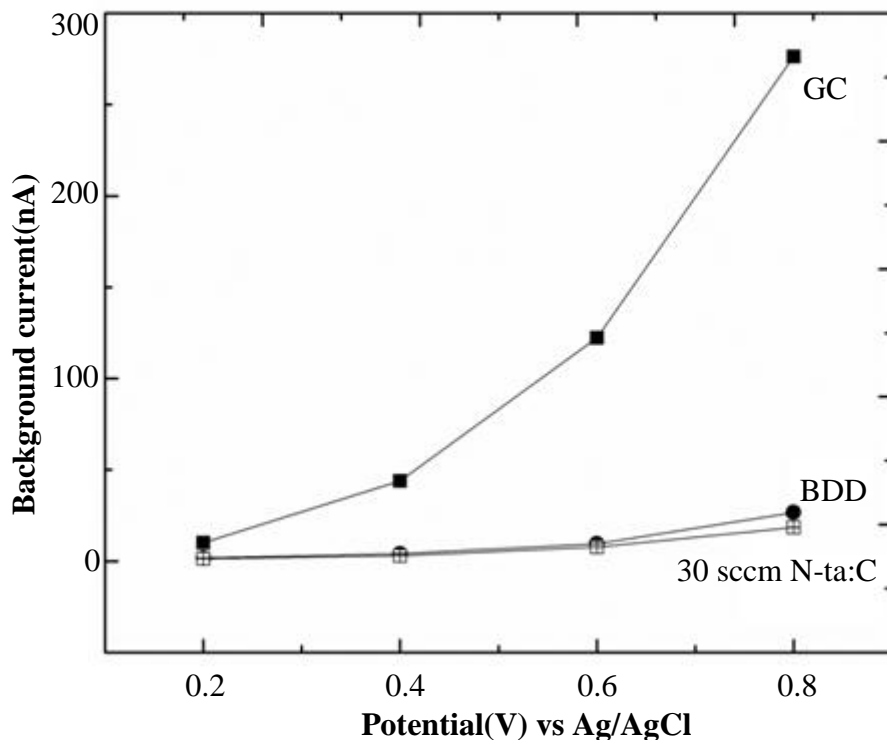


Figure 5.3 Background Hydrodynamic voltammetric *i-E* curves in 0.1M PBS(pH=7.2) for (■) glassy carbon(GC), (●) boron-doped diamond(BDD) and (□) a 30 sccm N-ta:C films. Flow rate = 1.0 mL/min. Electrode geometric area = 0.12 cm².

Figure 5.3 shows the background hydrodynamic voltammetric *i-E* curves for a 30 sccm N-ta:C film in 0.1M phosphate buffer (pH=7.2). Data for glassy carbon and boron-doped diamond are also presented for comparison. The carrier solution flow rate was 1.0 mL/min. The curves were obtained by changing the applied potential in 0.2 V increments starting at 0.2 V. During each potential step, the background current for doped diamond and the 30 sccm N-ta:C film stabilized much rapidly than did the current for glassy carbon. For example, at the beginning of measurements, it took over one hour for the glassy carbon background current to stabilize while the current for diamond and the N-ta:C film stabilized within 30 minutes. This

short stabilization time for the diamond and ta:C films results because of the microstructural stability of these surfaces as compared to glassy carbon. At all potentials, the background current for the diamond and ta:C were similar and lower than the values for glassy carbon by a factor of 3-10 depending on the potential. For example at 0.4 V, the background current was 2.87, 4.05 and 43.9 nA, respectively, for 30 sccm N-ta:C, doped diamond and glassy carbon. At the higher potentials, the glassy carbon current progressively increases due to microstructural alterations and surface oxidation processes. The lower background current for the 30 sccm N-ta:C film is a great advantage in amperometric detection schemes.

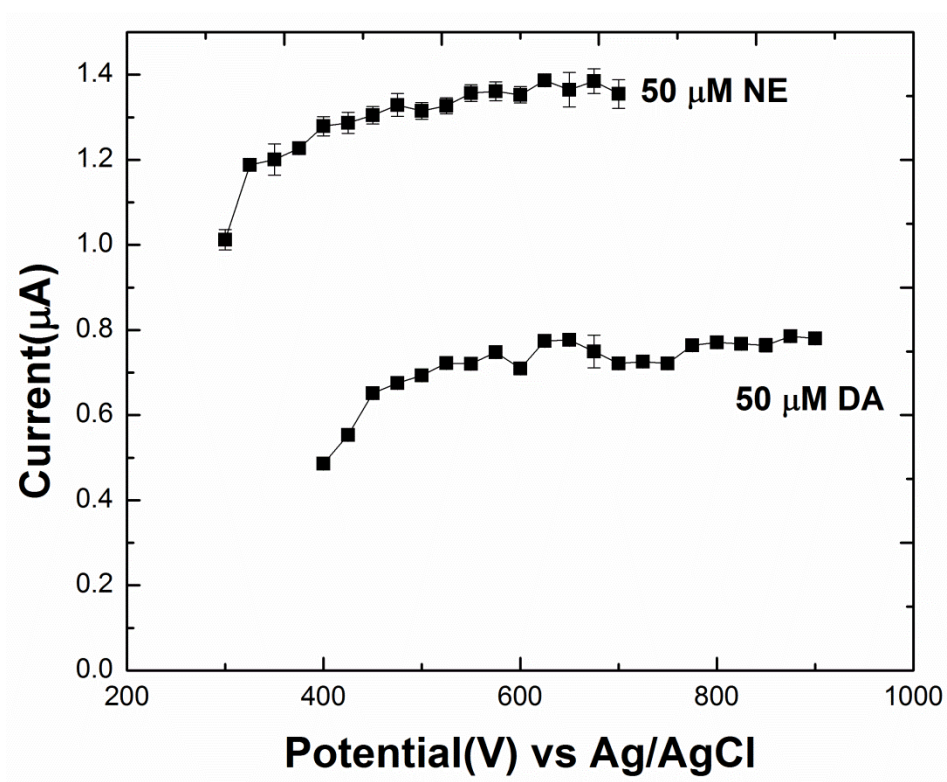


Figure 5.4 Hydrodynamic *i-E* curves for 50 μM norepinephrine (NE) in 0.1 PBS (pH=7.2) at a 30 sccm N-ta:C film., Flow rate = 1.0 mL/min. Electrode geometric area = 0.12 cm^2 .

Figure 5.4 showed the hydrodynamic *i-E* curves for 30 sccm N-ta:C film exposed to a 20 μL injection of 50 μM dopamine (DA) and 50 μM norepinephrine (NE) in 0.1M PBS buffer respectively. Well-defined sigmoidal curves were presented for all three analytes. The detection

potential was decided in the limiting current region. In the limiting current region, the current was most intense and the sensitivity of the electrode was stable. The detection potential was 0.65 V for 50 μM NE and 0.55 V for 50 μM DA. In the thin-layer cell, there was always some uncertainty in the actual channel height. The actual channel height was decided by how tightly the electrode was pressed against the gasket. Since 30 sccm N-ta:C was grown on fragile Si substrates, it was easy to crack it. The variation in actual channel height resulted in different limiting current for same concentration of NE and DA.

5.3.2. Detection figures of merit for DA and NE

After obtaining the detection potential for each analyte, the analytical detection figures of merit, including the linear dynamic range, sensitivity, response precision and response stability, were obtained and compared with BDD. The response precision was evaluated from running consecutive 30 injections of 1 μM and 100 μM DA and NE (Figure 5.5) in 0.1M PBS buffer (pH=7.2). The detection potential was 0.65 V and the mobile phase flow rate was 1.0 mL/min. The peaks were sharp and narrow. In Figure 5.5-1 μM DA, the relative standard deviation (RSD) for current was 1.62%. The current ratio between the 30s' injection and the 1st injection (i_p^{30}/i_p^1) was 97%. In Figure 5.5-100 μM DA, the RSD value was 0.34%, i_p^{30}/i_p^1 was 99%. For 30 sccm N-ta:C film, excellent reproducibility and stability were presented in 1 μM and 100 μM DA. The similar results were also obtained for NE. RSD was 1.6% for 1 μM NE and 1.8% for 100 μM with 30 consecutive injections in 15 minutes. The i_p^{30}/i_p^1 was 95.1% in 1 μM NE and 104.0% for 100 μM NE.

The long term stability was also tested to evaluate the response stability and resistance to fouling of 30 sccm N-ta:C film. Figure 5.6 showed the response of 30 sccm N-ta:C film for 1 μM DA and 1 μM NE in 0.1 M PBS buffer (pH=7.2) over a 6-h period. Five consecutive injections were made each hour. The mobile phase was 0.1M PBS (pH=7.2) buffer with flow rate of 1.0 mL/min. For 1 μM DA in 0.1M PBS buffer (pH=7.2), the current response over 6-h period was quite stable with RSD value of 1.9%. The RSD value was 7.3% for 1 μM NE, which was slightly higher.

30 sccm N-ta:C film showed good stability in the detection of DA and NE in both short and long term. This was due to the morphological and microstructural stability of this film. The lack of adsorption of DA and NE on this film was also an important reason. To evaluate the application of 30 sccm N-ta:C film in the analysis of dopamine and norepinephrine in EC-FIA, the analytical detection figures of merit were determined and compared with GC and BDD from literature, including linear dynamic range, sensitivity and response precision. The calibration curves were obtained in 0.1M PBS buffer (pH=7.2) as a function of analyte concentration. Figure 5.7 showed plots of log peak current vs log concentration for (A) dopamine and (B) norepinephrine. The calibration curves were obtained on 8 concentrations between 1 nM and 100 μM . The injection volume was 20 μL and consecutive 30 injections were made with 30 seconds' interval. In Figure 5.7 (A), the linear dynamic range for dopamine was four orders of magnitude from 0.1 μM to 100 μM ($R^2 = 0.99$). In Figure 5.7 (B), the linear dynamic range for norepinephrine was four orders of magnitude from 0.2 μM to 100 μM ($R^2 = 0.996$). After obtaining the LDRs, plots of current vs concentration were obtained in order to determine the response sensitivity. RSD for consecutive 30 injections of 1 μM of dopamine/norepinephrine in

0.1M PBS buffer (pH=7.2) were calculated. The figures of merit for dopamine and norepinephrine are summarized in Table 5.1 and Table 5.2 respectively. Comparison data is also presented from literature for GC and BDD. The linear dynamic ranges for dopamine and norepinephrine are smaller than GC and BDD's. But the sensitivity and peak variability are comparable to these of GC and BDD.

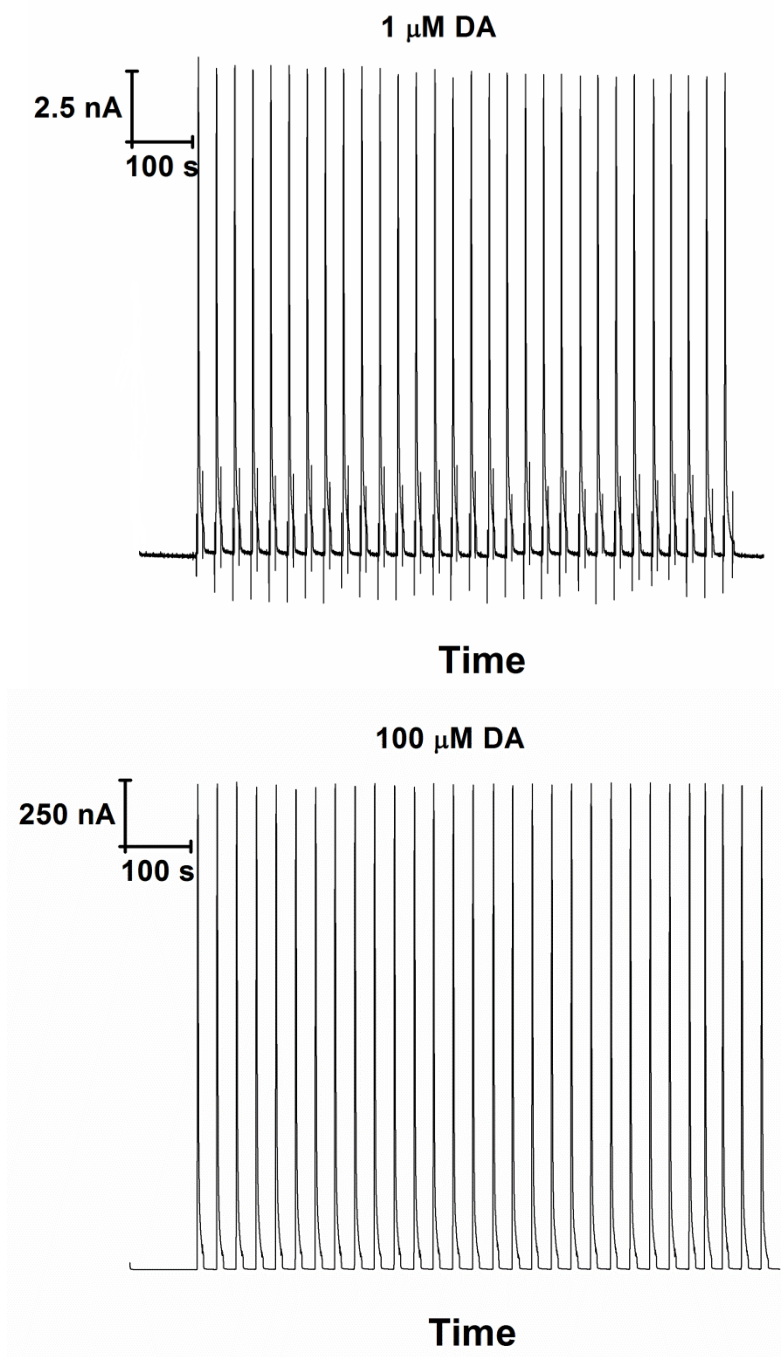


Figure 5.5 The amperometric response of a 30 sccm N-ta:C film to 30 consecutive injections of dopamine over a 15 minute period (1 and 100 μM) in 0.1M PBS buffer (pH=7.2) with detection potential of 0.65 V, flow rate of 1.0 mL/min.

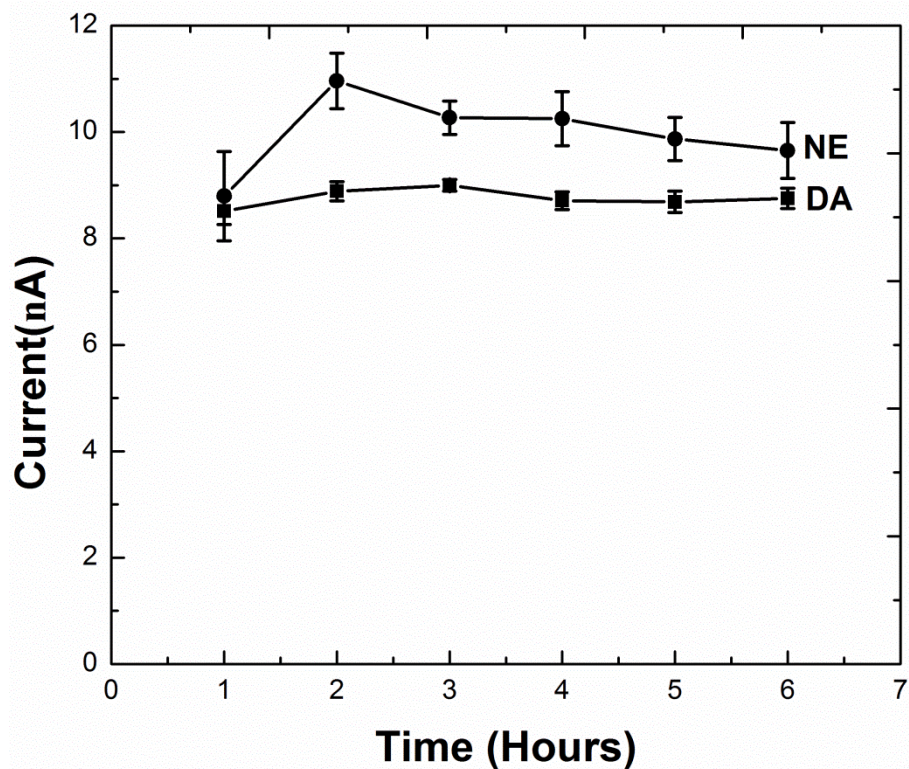


Figure 5.6 FIA-EC response of a 30 sccm N-ta:C film for 1 μ M DA (■) and 1 μ M NE(●) in 0.1M PBS (pH=7.2) buffer recorded over a 6-h period. Mobile phase was PBS buffer (pH=7.2), flow rate = 1.0 mL/min, electrode area = 0.12 cm². Each data point was calculated from 5 injections with interval of 30 second. The error bars were within the size of the marker.

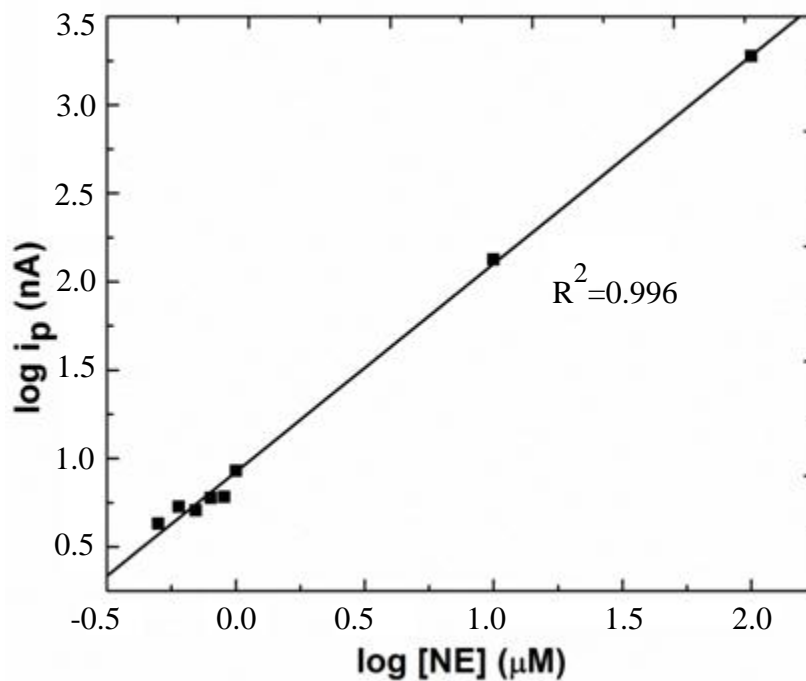
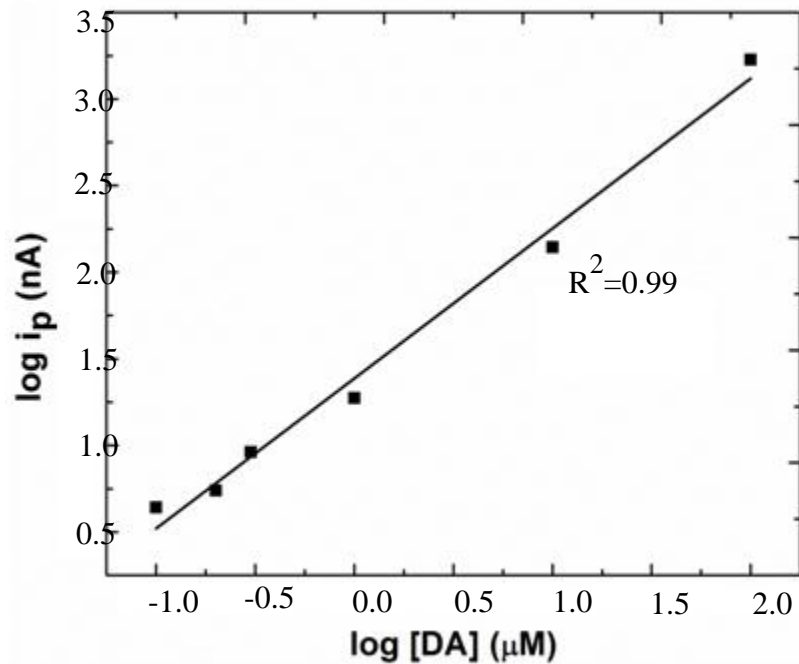


Figure 5.7 Calibration curves obtained for (A) dopamine and (B) norepinephrine for 30 sccm N-ta:C film . Mobile phase was 0.1 M PBS buffer (pH=7.2), flow rate = 1.0 mL/min, applied potential was 0.65 V for dopamine and 0.55 V for norepinephrine.

Electrode	Linear Dynamic Range, μM ($R^2 > 0.99$)	Sensitivity $\text{nA}/\mu\text{M}$	Peak Variability ($1 \mu\text{M}$, RSD %), $n=30$
30 sccm N-ta:C	0.01~100	16.0 ± 1.1	1.9 ± 0.3
GC ¹¹⁷	0.01~1000	17 ± 4	2.5
NCD ¹¹⁷	0.01~3000	16 ± 9	1.5
MCD ¹¹⁷	0.01~5000	16 ± 9	1.9

Table 5.1 FIA-EC data of 30 sccm N-ta:C film for dopamine.

Electrode	Linear Dynamic Range, μM ($R^2 > 0.99$)	Sensitivity $\text{nA}/\mu\text{M}$	Peak Variability ($1 \mu\text{M}$, RSD%), $n=30$
30 sccm N-ta:C	0.02~100	17.7 ± 2.4	2.4 ± 1.0
GC ¹¹⁷	0.01~4000	17 ± 1	2.9
NCD ¹¹⁷	0.01~3000	15 ± 6	2.4
MCD ¹¹⁷	0.01~7000	17 ± 7	1.4

Table 5.2 FIA-EC data of 30 sccm N-ta:C film for norepinephrine.

5.3.3 Conclusions

The cyclic voltammetric data showed the reactions of dopamine and norepinephrine were diffusion-controlled. The lack of adsorption on the 30 sccm N-ta:C film makes it potential candidate in the electrochemical detection of these catecholamines. By comparison with GC and BDD, the advantages of 30 sccm N-ta:C film in the detection of dopamine and norepinephrine in the electrochemical method are : (1) The stabilization time is comparable with BDD, smaller

than GC's. It usually takes 15 minutes to obtain stable background for BDD and 30 sccm N-ta:C film. While for GC, it usually takes over 40 minutes. (2) Background current is close to BDD's and much smaller than GC's, which could offer higher S/B and S/N ratios. (3) No fouling on the film's surface. (4) No pretreatment is required for 30 sccm N-ta:C film. For GC, polishing is a tedious procedure and the quality of polished GC is hard to control. The behavior of 30 sccm N-ta:C film in the detection of these catecholamines is more prone to BDD. But the growth condition for 30 sccm N-ta:C film is much milder than BDD's, including the growth temperature and growth rate. The 30 sccm N-ta:C film shows great promise in the detection of catecholamines in the future.

Chapter 6. Conclusions and Future Work

Tetrahedral amorphous carbon (ta:C) thin film electrodes are starting to be investigated and used in electroanalytic measurements. The sp^2 -bonded carbon content in the film strongly influences the electrical and electrochemical properties. The sp^3 -bonded carbon is responsible for the mechanical property and microstructure stability. By varying the sp^2/sp^3 ratio, ta:C films can be prepared to possess electrochemical properties more like those of glassy carbon or more like those of diamond. In this project, ta:C and N-ta:C films with sp^2 carbon contents in the 40-60% range offered excellent electrical and electrochemical properties. In fact, the properties of the ta:C and N-ta:C films resembled those expected for boron-doped diamond: low background current, microstructural stability, good electron-transfer kinetics for some aqueous redox systems without conventional pretreatment and weak molecular adsorption of polar analytes. The incorporation of nitrogen increases the sp^2 bonding in the film.

These ta:C and N-ta:C films are excellent candidates for electroanalytical measurements due to the following properties: low background current, wide working potential, fast electron-transfer rate for some aqueous redox couples, microstructural stability in harsh conditions and weak adsorption of the molecule, methylene blue. For the microstructure analysis, we used XPS, AFM, visible-Raman and EELS. XPS data revealed the nitrogen content in the near-surface region of these thin films (200 nm) increases from 0.05 to 0.15 atomic percent with increasing the nitrogen flow rate from 10 to 50 sccm in the source gas. Some oxygen is incorporated on the surface. The oxygen level was independent of the nitrogen incorporation. The carbon-oxygen surface functional groups could influence electrode response for some analytes but this was not

specifically investigated.. If oxygen were removed from the surface by, for example, hydrogen plasma treatment, then one could investigate the effects of the surface groups. From the visible-Raman spectral data, we know that the sp^2 -bonded carbon and/or sp^2 domain size increased with increasing nitrogen incorporation. EELS data proves the hypothesis that the sp^2 carbon content increased proportionally with the nitrogen incorporation. AFM images revealed a nodular morphology for all of films studied. The nodular feature size and the surface roughness increased with increasing nitrogen incorporation. The nodules result from the growth mechanism in the pulsed-laser deposition.

CP-AFM images revealed that the nodules on all of these films are electrically conducting and likely are domains of sp^2 -bonded carbon.. The random distribution of these nodules leads to the heterogeneous electrical properties of the ta:C and N-ta:C films. The nodule density and size increased with increasing the nitrogen content in the film. SECM electrochemical activity maps of $Ru(NH_3)_6^{+3/+2}$ and $Fe(CN)_6^{-3/-4}$ revealed spatially heterogeneous responses for both across the surface of ta:C and N-ta:C films. Similar heterogeneity was seen conductivity is also increased by increasing nitrogen content.

The lack of methylene blue adsorption, is consistent with the ta:C and n-ta:C films possessing surface properties much like those of boron-doped diamond. This molecule tenaciously adsorbs onto glassy carbon but weak adsorption is detected on diamond. The cyclic voltammetric behavior of the catecholamines, dopamine and norepinephrine, revealed no significant adsorption on the 30 sccm N-ta:C film surface. EC-FIA is applied to determine the detection figures of merit (linear dynamic range, sensitivity, response precision and stability) for

these two bioanalytes at the 30 sccm N-ta:C film. The performance of the 30 sccm N-ta:C film was found to be comparable with that of BDD.

In order to fully understand the microstructure, electrical and electrochemical properties of these films, there are still some issues needing study:

- (1) What is the nature of the chemical bond formed between the film's C and the incorporated N? It is hypothesized that the nitrogen exists as C=N, which served to increase the sp^2 carbon content in the film. Reflectance IR measurements may prove useful to answering this question.
- (2) What is the role of the surface carbon-oxygen functionalities that exist on the ta:C films after growth? Do they significantly affect the electrochemical properties of these films? This could be studied using a suite of redox systems, some of which are known to be kinetically sensitive to surface carbon-oxygen functionalities and some that are known to be insensitive. Furthermore, these redox systems could be studied at films before (with surface oxygen) and after hydrogen plasma treatment (without surface oxygen).
- (3) Why are the electrochemical reactivity maps in SECM data and the electrical properties in CP-AFM data heterogeneous across the ta:C and N-ta:C film surface? Is the electrical conductivity influenced by the π -states in the bandgap of the material or does the incorporated nitrogen function in a manner similar to a dopant atom by increasing the carrier concentration. To some extent, these questions can be answered by Hall Effect measurements as a function of the temperature.

REFERENCES

REFERENCES

1. R. L. McCreery, Carbon Electrodes: Structural Effects on Electron Transfer Kinetics. In *Electroanalytical Chemistry. A Series of Advances*, A. J. Bard, Ed. Dekker: 1991; Vol. 17, pp 221.
2. R. L. McCreery, *Chemical Reviews*. 108 (2008) 2646.
3. R. J. Rice; N. M. Pontikos; R. L. McCreery, *J. Am. Chem. Soc.* 112 (1990) 4617.
4. C. A. McDermott; K. R. Kneten; R. L. McCreery, *J. Electrochem. Soc.* 140 (1993) 2593.
5. K. K. Cline; M. T. McDermott; R. L. McCreery, *J. Phys. Chem.* 98 (1994) 5314.
6. P. Chen; M. A. Fryling; R. L. McCreery, *Anal. Chem.* 67 (1995) 3115.
7. P. Chen; R. L. McCreery, *Anal. Chem.* 68 (1996) 3958.
8. J. E. Field; Editor, *The Properties of Diamond*. Academic Press: 1979; p 674 pp.
9. N. Tokuda; T. Saito; H. Umezawa; H. Okushi; S. Yamasaki, *Diam Relat Mater.* 16 (2007) 409.
10. G. Swain, *Electroically Conducting Diamond Thin Films; Advanced Electrode Materials For Electrochemical Technologies*. Marcel Dekker, Inc.: 2004.
11. M. C. Granger; M. Witek; J. S. Xu; J. Wang; M. Hupert; A. Hanks; M. D. Koppang; J. E. Butler; G. Lucazeau; M. Mermoux; J. W. Strojek; G. M. Swain, *Anal Chem.* 72 (2000) 3793.
12. M. Wei; Y. Zhou; J. Zhi; D. Fu; Y. Einaga; A. Fujishima; X. Wang; Z. Gu, *Electroanalysis.* 20 (2008) 137.
13. G. M. Swain, *J. Electrochem. Soc.* 141 (1994) 3382.
14. M. C. Granger; J. S. Xu; J. W. Strojek; G. M. Swain, *Anal Chim Acta.* 397 (1999) 145.
15. D. Shin; A. Fujishima; A. Merkoci; J. Wang, *Chem. Sens.* 19 (2003) 130.
16. A. Suzuki; T. A. Ivandini; K. Yoshimi; A. Fujishima; G. Oyama; T. Nakazato; N. Hattori; S. Kitazawa; Y. Einaga, *Anal. Chem. (Washington, DC, U. S.)*. 79 (2007) 8608.
17. G. W. Muna; N. Tasheva; G. M. Swain, *Environ. Sci. Technol.* 38 (2004) 3674.
18. A. E. Fischer; G. M. Swain, *J. Electrochem. Soc.* 152 (2005) B369.
19. A. E. Fischer; G. M. Swain, *J Electrochem Soc.* 152 (2005) B369.

20. S. Waidmann; M. Knupfer; J. Fink; B. Kleinsorge; J. Robertson, *J Appl Phys.* 89 (2001) 3783.
21. J. Robertson, *Materials Science & Engineering R-Reports.* 37 (2002) 129.
22. C. Arena; B. Kleinsorge; J. Robertson; W. I. Milne; M. E. Welland, *J Appl Phys.* 85 (1999) 1609.
23. Aisenber.S; R. Chabot, *J Vac Sci Technol.* 8 (1971) 112.
24. M. Weiler; S. Sattel; K. Jung; H. Ehrhardt; V. S. Veerasamy; J. Robertson, *Appl Phys Lett.* 64 (1994) 2797.
25. Y. Lifshitz, *Diam Relat Mater.* 5 (1996) 388.
26. Y. Lifshitz, *Diam Relat Mater.* 8 (1999) 1659.
27. M. P. Siegal; J. C. Barbour; P. N. Provencio; D. R. Tallant; T. A. Friedmann, *Appl Phys Lett.* 73 (1998) 759.
28. N. M. J. Conway; A. C. Ferrari; A. J. Flewitt; J. Robertson; W. I. Milne; A. Tagliaferro; W. Beyer, *Diam Relat Mater.* 9 (2000) 765.
29. M. Weiler; S. Sattel; T. Giessen; K. Jung; H. Ehrhardt; V. S. Veerasamy; J. Robertson, *Phys Rev B.* 53 (1996) 1594.
30. J. Robertson, *Adv Phys.* 35 (1986) 317.
31. J. Robertson, *Mater. Sci. Forum.* 52-53 (1990) 125.
32. C. Arena; B. Kleinsorge; J. Robertson; W. I. Milne; M. E. Welland, *J. Appl. Phys.* 85 (1999) 1609.
33. M. G. Beghi; A. C. Ferrari; K. B. K. Teo; J. Robertson; C. E. Bottani; A. Libassi; B. K. Tanner, *Appl Phys Lett.* 81 (2002) 3804.
34. A. C. Ferrari; J. Robertson, *Philos. Trans. R. Soc. London, Ser. A.* 362 (2004) 2477.
35. A. C. Ferrari; S. E. Rodil; J. Robertson, *Phys Rev B.* 67 (2003).
36. B. Kleinsorge; A. C. Ferrari; J. Robertson; W. I. Milne; S. Waidmann; S. Hearne, *Diam Relat Mater.* 9 (2000) 643.
37. J. Robertson, *Curr. Opin. Solid State Mater. Sci.* 1 (1996) 557.
38. J. Robertson, *Diamond Relat. Mater.* 3 (1994) 361.

39. J. Robertson, *Diamond Relat. Mater.* 14 (2005) 942.
40. J. Robertson, *Semicond. Sci. Technol.* 18 (2003) S12.
41. J. Robertson; C. A. Davis, *Diam Relat Mater.* 4 (1995) 441.
42. S. Waidmann; M. Knupfer; J. Fink; B. Kleinsorge; J. Robertson, *Diam Relat Mater.* 9 (2000) 722.
43. Aisenber.S; R. Chabot, *J Appl Phys.* 42 (1971) 2953.
44. J. Schwan; S. Ulrich; H. Roth; H. Ehrhardt; S. R. P. Silva; J. Robertson; R. Samlenski; R. Brenn, *J Appl Phys.* 79 (1996) 1416.
45. S. Logothetidis, *Appl Phys Lett.* 69 (1996) 158.
46. V. I. Merkulov; D. H. Lowndes; G. E. Jellison; A. A. Puretzky; D. B. Geohegan, *Appl Phys Lett.* 73 (1998) 2591.
47. A. A. Voevodin; M. S. Donley, *Surf Coat Tech.* 82 (1996) 199.
48. Y. Huai; M. Chaker; J. N. Broughton; E. Gat; H. Pepin; T. Gu; X. Bian; M. Sutton, *Appl Phys Lett.* 65 (1994) 830.
49. M. Chhowalla; J. Robertson; C. W. Chen; S. R. P. Silva; C. A. Davis; G. A. J. Amaratunga; W. I. Milne, *J Appl Phys.* 81 (1997) 139.
50. C. A. Davis; G. A. J. Amaratunga; K. M. Knowles, *Phys Rev Lett.* 80 (1998) 3280.
51. S. D. Berger; D. R. Mckenzie; P. J. Martin, *Phil Mag Lett.* 57 (1988) 285.
52. N. Wada; P. J. Gaczi; S. A. Solin, *J. Non-Cryst. Solids.* 35-36 (1980) 543.
53. S. R. Sails; D. J. Gardiner; M. Bowden; J. Savage; D. Rodway, *Diamond Relat. Mater.* 5 (1996) 589.
54. K. W. R. Gilkes; H. S. Sands; D. N. Batchelder; W. I. Milne; J. Robertson, *J Non-Cryst Solids.* 227 (1998) 612.
55. A. C. Ferrari; J. Robertson, *Phys Rev B.* 64 (2001).
56. K. W. R. Gilkes; S. Praver; K. W. Nugent; J. Robertson; H. S. Sands; Y. Lifshitz; X. Shi, *J Appl Phys.* 87 (2000) 7283.
57. M. Profeta; F. Mauri, *Phys Rev B.* 63 (2001).

58. W. G. Cui; Q. B. Lai; L. Zhang; F. M. Wang, *Surf Coat Tech.* 205 (2010) 1995.
59. P. Stumm; D. A. Drabold; P. A. Fedders, *J. Appl. Phys.* 81 (1997) 1289.
60. C. Arena; B. Kleinsorge; J. Robertson; W. I. Milne; M. E. Welland, *Diam Relat Mater.* 8 (1999) 435.
61. P. Stumm; D. A. Drabold; P. A. Fedders, *J Appl Phys.* 81 (1997) 1289.
62. Y. Tanaka; M. Furuta; K. Kuriyama; R. Kuwabara; Y. Katsuki; T. Kondo; A. Fujishima; K. Honda, *Electrochim Acta.* 56 (2011) 1172.
63. K. Yoo; B. Miller; R. Kalish; X. Shi, *Electrochemical and Solid-State Letters.* 2 (1999) 233.
64. D. Sopchak; B. Miller; R. Kalish; Y. Avyigal; X. Shi, *Electroanalysis.* 14 (2002) 473.
65. A. Zeng; E. Liu; S. N. Tan; S. Zhang; J. Gao, *Electroanalysis.* 14 (2002) 1110.
66. S. Liu; G. Wang; Z. Wang, *J. Non-Cryst. Solids.* 353 (2007) 2796.
67. N. W. Khun; E. Liu; H. W. Guo, *Electroanalysis.* 20 (2008) 1851.
68. L. Han; X. Chen; L. Yang; Y. Wang; X. Wang; Y. Zhao, *Appl. Surf. Sci.* 257 (2011) 6945.
69. Y. E. Evstefeeva; Y. V. Pleskov; A. M. Kutsay; I. Bello, *Russian Journal of Electrochemistry.* 41 (2005) 772.
70. Y. V. Pleskov; A. Y. Sakharova; M. D. Krotova; L. L. Builov; B. V. Spitsyn, *J. Electroanal. Chem. Interfacial Electrochem.* 228 (1987) 19.
71. A. Zeng; M. M. M. Bilek; D. R. McKenzie; P. A. Lay, *Diamond Relat. Mater.* 18 (2009) 1102.
72. A. Zeng; M. M. M. Bilek; D. R. McKenzie; P. A. Lay, *Diamond Relat. Mater.* 18 (2009) 1211.
73. N. A. Marks; D. R. McKenzie; B. A. Pailthorpe; M. Bernasconi; M. Parrinello, *Phys. Rev. Lett.* 76 (1996) 768.
74. V. S. Veerasamy; J. Yuan; G. A. J. Amaratunga; W. I. Milne; K. W. R. Gilkes; M. Weiler; L. M. Brown, *Phys Rev B.* 48 (1993) 17954.
75. V. S. Veerasamy; G. A. J. Amaratunga; C. A. Davis; A. E. Timbs; W. I. Milne; D. R. Mckenzie, *J Phys-Condens Mat.* 5 (1993) L169.

76. B. Kleinsorge; A. C. Ferrari; J. Robertson; W. I. Milne, *J Appl Phys.* 88 (2000) 1149.
77. F. Weich; J. Widany; T. Frauenheim, *Phys Rev Lett.* 78 (1997) 3326.
78. L. B. Valdes, *P Ire.* 42 (1954) 420.
79. S. Ranganathan; T.-C. Kuo; R. L. McCreery, *Anal. Chem.* 71 (1999) 3574.
80. Y. Show; V. M. Swope; G. M. Swain, *Diamond Relat. Mater.* 18 (2009) 1426.
81. S. Jolley; M. Koppang; T. Jackson; G. M. Swain, *Anal Chem.* 69 (1997) 4099.
82. S. Wang; G. M. Swain, *J. Phys. Chem. C.* 111 (2007) 3986.
83. J. Kwak; A. J. Bard, *Anal Chem.* 61 (1989) 1794.
84. J. Kwak; A. J. Bard, *Anal Chem.* 61 (1989) 1221.
85. J. C. Lascovich; R. Giorgi; S. Scaglione, *Applied Surface Science.* 47 (1991) 17.
86. D. Drescher; J. Koskinen; H. J. Scheibe; A. Mensch, *Diamond Relat. Mater.* 7 (1998) 1375.
87. S. Bhattacharyya; M. Hietschold; F. Richter, *Diam Relat Mater.* 9 (2000) 544.
88. A. C. Ferrari; J. Robertson, *Physical Review B.* 61 (2000) 14095.
89. J. S. Xu; Q. Y. Chen; G. M. Swain, *Anal Chem.* 70 (1998) 3146.
90. K. R. Kneten; R. L. McCreery, *Anal. Chem.* 64 (1992) 2518.
91. J. A. Bennett; J. Wang; Y. Show; G. M. Swain, *J. Electrochem. Soc.* 151 (2004) E306.
92. S. Wang; V. M. Swope; J. E. Butler; T. Feygelson; G. M. Swain, *Diamond Relat. Mater.* 18 (2009) 669.
93. A. E. Fischer; Y. Show; G. M. Swain, *Anal. Chem.* 76 (2004) 2553.
94. J. Jia; D. Kato; R. Kurita; Y. Sato; K. Maruyama; K. Suzuki; S. Hirono; T. Ando; O. Niwa, *Anal. Chem.* 79 (2007) 98.
95. O. Niwa; J. Jia; Y. Sato; D. Kato; R. Kurita; K. Maruyama; K. Suzuki; S. Hirono, *J. Am. Chem. Soc.* 128 (2006) 7144.
96. N. Sekioka; D. Kato; A. Ueda; T. Kamata; R. Kurita; S. Umemura; S. Hirono; O. Niwa, *Carbon.* 46 (2008) 1918.

97. D. Kato; N. Sekioka; A. Ueda; R. Kurita; S. Hirono; K. Suzuki; O. Niwa, *J. Am. Chem. Soc.* *130* (2008) 3716.
98. A. Ilie; A. Hart; A. J. Flewitt; J. Robertson; W. I. Milne, *J Appl Phys.* *88* (2000) 6002.
99. A. Ilie; A. C. Ferrari; T. Yagi; J. Robertson, *Appl Phys Lett.* *76* (2000) 2627.
100. F. Houze; R. Meyer; O. Schneegans; L. Boyer, *Appl Phys Lett.* *69* (1996) 1975.
101. X. Y. Yang; L. Haubold; G. DeVivo; G. M. Swain, *Analytical Chemistry.* *84* (2012) 6240.
102. K. B. Holt; A. J. Bard; Y. Show; G. M. Swain, *Journal of Physical Chemistry B.* *108* (2004) 15117.
103. S. H. Wang; G. M. Swain, *J Phys Chem C.* *111* (2007) 3986.
104. A. J. Bard; M. V. Mirkin; Editors, *Scanning Electrochemical Microscopy.* Marcel Dekker, Inc.: 2001; p 650 pp.
105. A. J. Bard; G. Denuault; C. Lee; D. Mandler; D. O. Wipf, *Acc. Chem. Res.* *23* (1990) 357.
106. F. Peter; M. Gross, *J Electroanal Chem.* *61* (1975) 245.
107. M. Noel; P. N. Anantharaman, *Analyst.* *110* (1985) 1095.
108. S. Ranganathan; R. L. McCreery, *Anal. Chem.* *73* (2001) 893.
109. J. Bergquist; A. Sciubisz; A. Kaczor; J. Silberring, *J Neurosci Meth.* *113* (2002) 1.
110. A. M. Krstulovic; Editor, *Quantitative Analysis of Catecholamines and Related Compounds.* Ellis Horwood Ltd.: 1986; p 384 pp.
111. G. A. Scratchley; A. N. Masoud; S. J. Stohs; D. W. Wingard, *J Chromatogr.* *169* (1979) 313.
112. C. Refshauge; P. T. Kissinger; R. Dreiling; L. Blank; R. Freeman; R. N. Adams, *Life Sci.* *14* (1974) 311.
113. G. Hanrahan; F. Dahdouh; K. Clarke; F. A. Gomez, *Curr. Anal. Chem.* *1* (2005) 321.
114. W. Xu; R. Sandford; P. Worsfold; A. Carlton; G. Hanrahan, *Crit. Rev. Anal. Chem.* *35* (2005) 237.
115. R. L. McCreery, *Neuromethods.* *27* (1995) 1.

116. J. Mattusch; K. H. Hallmeier; K. Stulik; V. Pacakova, *Electroanalysis (N. Y.). 1* (1989) 405.
117. G. F. M. Pimienta. The electrochemical oxidation and amperometric detection of catechols and catecholamines at boron-doped diamond thin-film electrodes. 1424723, Michigan State University, United States -- Michigan, 2004.
118. S. H. DuVall; R. L. McCreery, *Anal. Chem.* 71 (1999) 4594.